Eur. Phys. J. C (2026) 86:802
https://doi.org/10.1140/epjc/s10052-026-15960-1

THE EUROPEAN PHYSICAL JOURNAL C

Regular Article - Theoretical Physics

Toward a comprehensive exploration of flavored dark matter models

Benedetta Belfatto[1,a], **Monika Blanke**[1,2,b], **Jan Heisig**[3,c], **Michael Krämer**[3,d], **Lena Rathmann**[2,3,e], **Felix Wilsch**[3,f]

[1] Institut für Theoretische Teilchenphysik, Karlsruhe Institute of Technology, Engesserstraße 7, 76128 Karlsruhe, Germany
[2] Institut für Astroteilchenphysik, Karlsruhe Institute of Technology, Hermann-von-Helmholtz-Platz 1, 76344 Eggenstein-Leopoldshafen, Germany

[3] Institute for Theoretical Particle Physics and Cosmology, RWTH Aachen University, Sommerfeldstr. 16, 52056 Aachen, Germany

Received: 7 January 2026 / Accepted: 8 June 2026

Abstract We present a comprehensive framework for the study of flavored dark matter models, combining relic density calculations with direct and indirect detection limits, collider constraints, and a global analysis of flavor observables based on SMEFT matching and renormalization-group evolution. The framework applies to scalar or fermionic dark matter, including both self-conjugate and non-self-conjugate cases. As a proof of principle, we analyze two scenarios with Majorana dark matter coupling to right-handed charged leptons and to right-handed down-type quarks, assuming a thermal freeze-out. In the leptophilic case, flavor-violating decays such as $\mu \to e\gamma$ dominate the constraints, while LHC searches still leave sizable parameter space. For quark couplings, direct detection bounds and meson mixing severely restrict the allowed couplings, favoring hierarchical flavor structures. The toolchain presented in this paper is publicly available on GitHub.

Contents

[a] e-mail: benedetta.belfatto@kit.edu
[b] e-mail: monika.blanke@kit.edu (corresponding author)
[c] e-mail: heisig@physik.rwth-aachen.de
[d] e-mail: mkraemer@physik.rwth-aachen.de
[e] e-mail: lena.rathmann@kit.edu
[f] e-mail: felix.wilsch@physik.rwth-aachen.de

1 Introduction

The Standard Model (SM) of particle physics has proven to be extremely successful in describing laboratory-based experi-

Published online: 13 July 2026

ments. However, it fails to address some fundamental theoretical questions like the origin of its gauge symmetry structure, the dynamics behind electroweak symmetry breaking (EWSB), and the origin of flavor and its hierarchies. Notably, the majority of free SM parameters appear in the latter sector, calling for an extended theory of flavor. Additionally, and perhaps even more pressingly, the SM also falls short of explaining several fundamental astrophysical and cosmological observations such as the origin of the matter-antimatter asymmetry and the existence of Dark Matter (DM) in our Universe. It is hence expected that a more complete theory addressing some or ideally all of these issues will ultimately replace the SM.

A common approach toward achieving this goal is the study of minimal renormalizable extensions of the SM – so-called simplified models – that address one or more of the aforementioned issues. Analyzing their phenomenology provides insight into the necessary ingredients of a more complete theory.

A popular class of simplified models of DM introduces a t-channel mediator that couples the DM particle to the SM fermion sector. A recent review of this class of models can be found in [1]. While the simplest t-channel models introduce only a single DM and mediator field each, a non-trivial flavor structure can also be present in the dark sector. For example, in simplified models of the Minimal Supersymmetric Standard Model, the lightest neutralino – a Majorana fermion – is the non-flavored DM candidate while the squarks or sleptons are flavored scalars that serve as the t-channel mediators. Models with multiple mediator flavors have also been considered in [2–4]. Flavored DM models, on the other hand, introduce the DM candidate as the lightest state of a flavor multiplet, while the mediator field remains a singlet under the flavor group [5–7]. Lastly, in skew-flavored DM models both mediator and DM are flavored [8].

Flavored DM, in particular, comes along with significant phenomenological advantages. On the one hand, the tension between the observed relic abundance and the non-observation of DM in direct detection experiments can be relieved by weakening the coupling of the DM candidate to the detector nuclei [7,9]. On the other hand, the models' phenomenology becomes much richer, including signatures of more complicated decay chains at the LHC, and the effects of flavor-violating new interactions in both flavor and collider physics experiments [9–11]. Additionally, flavored DM offers exciting opportunities for nonstandard freeze-out dynamics, such as conversion-driven freeze-out [12,13], whose realization in this framework [14] opens up further viable regions of parameter space and can simultaneously account for baryogenesis [15].

While a number of previous papers have analyzed the phenomenology of flavored DM models – see Table 1 for an overview – significant parts of the flavored DM model space remain completely untouched. To improve our understanding of flavored DM, in this paper we therefore provide a toolchain that facilitates future phenomenological studies. The toolchain connects various publicly available tools for constraining models of DM and other new physics (NP) models, namely FeynRules [16], micrOMEGAs [17–20], SModelS [21–23], Matchete [24] and smelli [25] (based upon flavio [26] and Wilson [27]).

In Sect. 2, we begin with a classification of flavored DM models. Section 3 describes the setup of our toolchain, discussing in turn the handling of constraints from the DM relic abundance, direct and indirect detection, LHC and flavor physics. Then in Sect. 4, we apply the toolchain to two different flavored DM models that have not been studied in detail in the literature before, namely flavored Majorana DM coupled to either the right-handed charged leptons or to the right-handed down-type quarks, and discuss the results. Appendix A summarizes the naming conventions used in the model files of the provided toolchain, while Appendix B provides a detailed discussion of the flavor structure and flavor constraints for the down-type quark scenario.

2 Classification of flavored dark matter models

The flavored DM framework, broadly defined, comprises models in which the DM field is introduced as part of a flavor multiplet. In addition, it is commonly assumed that DM transforms as a singlet under the SM gauge symmetry and couples to the SM fermion sector via a t-channel mediator. In what follows, we adopt these assumptions. We further restrict our attention to simplified models in which only a single mediator is introduced in addition to the DM flavor multiplet. Models with multiple mediator flavors have been considered e. g. in [2–4]. A scenario in which both DM and the mediator carry flavor has been investigated in [8]. Finally, a model with two mediators of different gauge representations coupling DM to both left- and right-handed leptons has been considered in [28].

Massive spin-1 fields in a simplified model introduce additional complications and should therefore be considered with caution. In a possible UV completion such a spin-1 state arises either as a massive vector after spontaneous symmetry breaking of a bigger gauge group down to the SM gauge group $\mathcal{G}_{\text{SM}}$, or as a composite vector resonance of a strongly coupled sector. In both cases we generally expect further states of similar mass present in the theory that can alter conclusions. Therefore, while phenomenologically viable models with new vector states can be constructed, we do not include this case in our classification and restrict ourselves to dark sectors with only new spin-0 and spin-1/2 fields, i. e. scalars and fermions.

Under these assumptions, the field content of flavored DM models generally contains the following particles:

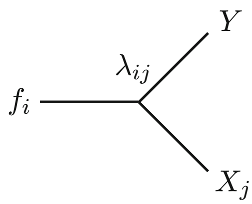

Fig. 1 Schematic visualization of the interaction of a DM field X with a SM fermion f and a mediator field Y. Here i, j are (SM and dark) flavor indices

- $f = (f_1, f_2, f_3)^\mathsf{T}$: 3-generation SM fermion field
- $X = (X_1, X_2, \dots X_n)^\mathsf{T}$: n generations of DM field
- Y: t-channel mediator field

where we adopt the notation of [1]. These states feature interactions of the form

$$\mathcal{L}_{\text{int}} = -\lambda_{ij} \bar{f}_i X_j Y + \text{h.c.}, \tag{2.1}$$

schematically depicted in Fig. 1.

Since X is assumed to be a gauge singlet, the mediator Y has to carry the same gauge quantum numbers as the fermion f in the interaction (2.1). This leads us to five different classes of flavored DM models depending on the fermion f coupled to the dark sector. In each case Y can be chosen to be either a scalar or a fermion field,[1] which in turn fixes X to be fermionic or scalar, respectively. Finally, X can be either real or complex, resulting in four possible combinations for each choice of SM fermion f. In total, this yields 20 distinct scenarios involving a single flavored DM multiplet field and a single mediator field, which we summarize in Table 1 along with references to previous studies where applicable.

To ensure DM stability, we assume a $\mathbb{Z}_2$ symmetry under which both the mediator Y and the DM field X are charged. The lightest flavor X_1 is thus stable and serves as DM candidate as long as $M_{X_1} < M_Y$. Note that in some of the simplified models introduced below this $\mathbb{Z}_2$ symmetry is accidental. In order to ensure DM stability in UV-complete models of flavored DM, flavor symmetries can be used to stabilize the DM candidate [6,9,29].

The form of the Lagrangian depends on the choice of spin representation for X and Y. Below we collect the four possible cases, in which we adopt the more common notation $\tilde{S}$ and S for real and complex scalar DM, $\tilde{\chi}$ and χ for Majorana and Dirac DM, and ψ and φ for a fermionic and scalar mediator, respectively. Furthermore, notice that in our notation, scalar mass parameters before EWSB are denoted by lower-case letters (m), whereas physical scalar masses after EWSB are labeled by capital letters (M). Fermion masses do not receive corrections from EWSB in our setup, and we label them by capital letters (M). Accordingly, for the Dirac and Majorana DM case, fermion masses are denoted by M_χ and $M_{\tilde{\chi}}$, respectively, while for the mediator one has $m_\varphi \neq M_\varphi$. For the real and complex scalar DM case, this distinction similarly leads to $m_S \neq M_S$ and $m_{\tilde{S}} \neq M_{\tilde{S}}$, whereas the mediator mass is denoted by M_ψ.

- *Real scalar DM*
  In this case, we introduce a real scalar DM field $X \equiv \tilde{S}$ which is flavored and a mediator $Y \equiv \psi$ which is a Dirac fermion and carries the gauge quantum numbers of the SM fermion f. The Lagrangian before EWSB describing all possible NP interactions is given by

$$\begin{aligned}\mathcal{L} \supset\, & \frac{1}{2}(\partial_\mu \tilde{S})(\partial^\mu \tilde{S}) - \frac{1}{2} m_{\tilde{S}}^2 \tilde{S}\tilde{S} + \bar{\psi}(i\not{D} - M_\psi)\psi \\ & + (\lambda_{ij} \bar{f}_i \psi \tilde{S}_j + \text{h.c.}) + \lambda_{\tilde{S}H,ij}(\tilde{S}_i \tilde{S}_j)(H^\dagger H) \\ & + \lambda_{\tilde{S}\tilde{S},ijkl} \tilde{S}_i \tilde{S}_j \tilde{S}_k \tilde{S}_l\,,\end{aligned} \tag{2.2}$$

  where $m_{\tilde{S}}$ is the flavored DM mass matrix before EWSB. The complex matrix λ_{ij} describes the coupling of the mediator to the SM fermions f_i and the DM flavor multiplet. The hermitian coupling matrix $\lambda_{\tilde{S}H}$ describes the interactions of $\tilde{S}$ with the Higgs doublet H, given by $H = (-i\, G^+, 1/\sqrt{2}\,(v + h + i\, G^0))^\mathsf{T}$ after EWSB. This Higgs portal interaction induces an additional contribution to the DM mass term after

$$M_{\tilde{S}}^2 = m_{\tilde{S}}^2 - v^2 \lambda_{\tilde{S}H}, \tag{2.3}$$

  where $v = 246\,\text{GeV}$ is the vacuum expectation value of the Higgs. Finally, the coupling $\lambda_{\tilde{S}\tilde{S},ijkl}$ describes the flavored DM self-interactions.
- *Complex scalar DM*
  The Lagrangian for complex scalar flavored DM, S, is very similar to the real DM case in Eq. (2.2). It reads

$$\begin{aligned}\mathcal{L} \supset\, & (\partial_\mu S)^\dagger(\partial^\mu S) - m_S^2 S^\dagger S + \bar{\psi}(i\not{D} - M_\psi)\psi \\ & + (\lambda_{ij} \bar{f}_i \psi S_j + \text{h.c.}) + \lambda_{SH,ij}(S_i^\dagger S_j)(H^\dagger H) \\ & + \lambda_{SS,ijkl}(S_i^\dagger S_j)(S_k^\dagger S_l).\end{aligned} \tag{2.4}$$

  Again, the Higgs portal interaction induces a contribution from EWSB to the DM mass matrix

$$M_S^2 = m_S^2 - \frac{v^2}{2}\lambda_{SH}. \tag{2.5}$$

- *Majorana DM*
  We write the Majorana DM field $X \equiv \tilde{\chi}$ as a four-component Majorana spinor $\tilde{\chi} = (\tilde{\chi}_L, i\sigma_2 \tilde{\chi}_L^*)^\mathsf{T}$ where $\tilde{\chi}_L$ is a two-component Weyl spinor. The mediator $Y \equiv \varphi$ is a complex scalar field that carries the same gauge

[1] Recall that we avoid the case of vector mediators for the reasons mentioned above.

Table 1 Overview of all possible combination of DM candidates and mediators that can couple to the various SM fermions. The second column shows the gauge quantum numbers of the mediator and its spin s, the third column shows the nature of the DM fields, and the fourth and fifth column list the literature where such a combination was considered within the context of Minimal Flavor Violation (MFV) or beyond, respectively (if available). Note that in Refs. [5,31,32,41,43] considered flavored DM in the EFT limit without explicitly introducing the t-channel mediator

f	Y: $\mathcal{G}_{\rm SM} \times s$	$X \sim (\mathbf{1},\mathbf{1})_0$	MFV	Beyond MFV
q	$(\mathbf{3},\mathbf{2})_{1/6} \times 0$	Dirac fermion	–	[11,30]
		Majorana fermion	–	–
	$(\mathbf{3},\mathbf{2})_{1/6} \times \frac{1}{2}$	Complex scalar	[31,32]	–
		Real scalar	–	–
u	$(\mathbf{3},\mathbf{1})_{2/3} \times 0$	Dirac fermion	[7,29,33,34]	[10,11,35]
		Majorana fermion	–	[14,36]
	$(\mathbf{3},\mathbf{1})_{2/3} \times \frac{1}{2}$	Complex scalar	[31,32]	–
		Real scalar	–	–
d	$(\mathbf{3},\mathbf{1})_{-1/3} \times 0$	Dirac fermion	[7,37]	[5,9,38]
		Majorana fermion	–	–
	$(\mathbf{3},\mathbf{1})_{-1/3} \times \frac{1}{2}$	Complex scalar	[31,32]	–
		Real scalar	–	–
ℓ	$(\mathbf{1},\mathbf{2})_{-1/2} \times 0$	Dirac fermion	[7]	–
		Majorana fermion	–	[39,40]
	$(\mathbf{1},\mathbf{2})_{-1/2} \times \frac{1}{2}$	Complex scalar	[41]	[28]
		Real scalar	–	–
e	$(\mathbf{1},\mathbf{1})_{-1} \times 0$	Dirac fermion	[7,42,43]	[44,45]
		Majorana fermion	–	[15,46]
	$(\mathbf{1},\mathbf{1})_{-1} \times \frac{1}{2}$	Complex scalar	[41,43]	[28,47,48]
		Real scalar	–	–

quantum numbers as the SM fermion f. The general Lagrangian before EWSB is given by

$$\begin{aligned}\mathcal{L} \supset\; & \frac{1}{2}\bar{\tilde{\chi}}(i\partial\!\!\!/ - M_{\tilde{\chi}})\tilde{\chi} + (D_\mu\varphi)^\dagger(D^\mu\varphi) - m_\varphi^2\varphi^\dagger\varphi \\ & + (\lambda_{ij}\bar{f}_i\tilde{\chi}_j\varphi + \text{h.c.}) \\ & + \lambda_{\varphi H,1}(\varphi^\dagger\varphi)(H^\dagger H) + \lambda_{\varphi H,2}(H^\dagger\varphi)(\varphi^\dagger H) \\ & + \frac{1}{2}\lambda_{\varphi H,3}[(H_i\varepsilon^{ij}\varphi_j)^2 + \text{h.c.}] + \lambda_{\varphi\varphi}(\varphi^\dagger\varphi)^2.\end{aligned} \tag{2.6}$$

In contrast to the scalar DM models introduced above, the Majorana fermion DM field does not couple to the Higgs doublet at tree level. Instead, the $\lambda_{\varphi H}$ coupling terms couple the mediator φ to the SM Higgs field. Therefore, the mass term m_φ^2 receives a correction from EWSB. Note that not all $\lambda_{\varphi H}$ terms in the Lagrangian are present in all Majorana DM models. The charge of the mediator therefore determines the correction to the mass term after EWSB. For an SU$(2)_L$-singlet mediator only the term $\lambda_{\varphi H,1}(\varphi^\dagger\varphi)(H^\dagger H)$ is present, resulting in the physical squared mass of the mediator after EWSB

$$M_\varphi^2 = m_\varphi^2 - \frac{v^2}{2}\lambda_{\varphi H,1}\,. \tag{2.7}$$

An SU$(2)_L$-doublet mediator coupled to the left-handed quark doublet additionally couples to the Higgs doublet through the $\lambda_{\varphi H,2}(H^\dagger\varphi)(\varphi^\dagger H)$ term. The components of the mediator doublet $\varphi = (\varphi_u, \varphi_d)^\intercal$ thus receive different contributions to their squared masses after EWSB, given by

$$\begin{aligned}M_{\varphi_u}^2 &= m_\varphi^2 - \frac{v^2}{2}\lambda_{\varphi H,1}, \\ M_{\varphi_d}^2 &= m_\varphi^2 - \frac{v^2}{2}(\lambda_{\varphi H,1} + \lambda_{\varphi H,2}).\end{aligned} \tag{2.8}$$

Lastly, a doublet mediator coupled to the left-handed lepton doublet can be parameterized as $\varphi = (1/\sqrt{2}(\varphi_R + i\varphi_I), \varphi^-)^\intercal$, where we decomposed the neutral component of the doublet into its real and imaginary parts φ_R and φ_I as done in scotogenic models [39]. In this case all $\lambda_{\varphi H}$ terms are present, and the squared masses of the physical neutral scalar bosons are given by

$$M^2_{\varphi_R} = m^2_\varphi - \frac{v^2}{2}(\lambda_{\varphi H,1} + \lambda_{\varphi H,3})\,,$$
$$M^2_{\varphi_I} = m^2_\varphi - \frac{v^2}{2}(\lambda_{\varphi H,1} - \lambda_{\varphi H,3}). \tag{2.9}$$

The squared mass of the charged scalar boson is given by

$$M^2_{\varphi^-} = m^2_\varphi - \frac{v^2}{2}(\lambda_{\varphi H,1} + \lambda_{\varphi H,2})\,. \tag{2.10}$$

- *Dirac DM*
  For Dirac DM the flavor triplet $X \equiv \chi$ is a Dirac fermion while the scalar mediator $Y \equiv \varphi$ can be described analogously to the Majorana fermion DM models. The Lagrangian closely resembles the one of the Majorana fermion DM models and is given by

$$\begin{aligned}\mathcal{L} \supset\, & \bar{\chi}(i\not{\partial} - M_\chi)\chi \\ & + (D_\mu\varphi)^\dagger(D^\mu\varphi) - m^2_\varphi\varphi^\dagger\varphi + (\lambda_{ij}\bar{f}_i\chi_j\varphi + \text{h.c.}) \\ & + \lambda_{\varphi H,1}(\varphi^\dagger\varphi)(H^\dagger H) \\ & + \lambda_{\varphi H,2}(H^\dagger\varphi)(\varphi^\dagger H) + \frac{1}{2}\lambda_{\varphi H,3}[(H_i\varepsilon^{ij}\varphi_j)^2 + \text{h.c.}] \\ & + \lambda_{\varphi\varphi}(\varphi^\dagger\varphi)^2\end{aligned} \tag{2.11}$$

  Since the coupling of the mediator to the Higgs doublet is completely analogous to the Majorana fermion DM models, the mediator masses are again given by Eqs. (2.7), (2.8), (2.9), and (2.10) depending on the gauge quantum numbers of φ.

Beyond the classification in Table 1, flavored DM models are distinguished by the dark sector's flavor structure. While a priori any number $n > 1$ of generations is possible, the most common assumption in the literature is $n = 3$ in analogy to the SM flavor structure. Furthermore, different possible scenarios for flavor symmetries in the dark sector have been discussed. The most common choices are minimal flavor violation (MFV) or dark minimal flavor violation (DMFV).

MFV [49–52] is based on the assumption that the approximate flavor symmetry

$$G_{\text{MFV}} = U(3)_q \times U(3)_u \times U(3)_d \times U(3)_\ell \times U(3)_e \tag{2.12}$$

is broken only by the SM Yukawa couplings Y_u, Y_d, Y_e even in the presence of new particles and interactions. The DM flavor multiplet X then has to transform under a non-trivial representation of one of the $U(3)$ factors in G_{MFV}. Therefore, only certain values for the number n of dark generations are possible in MFV. The structure of the coupling matrix λ between the dark sector and the SM sector is also restricted by MFV and can be determined using the usual MFV spurion expansion. In the same way, also the DM mass matrix and the Higgs-portal coupling matrix for scalar DM are determined by the MFV expansion.

The DMFV hypothesis [9] extends the MFV framework in a minimal way. The flavor symmetry group G_{MFV} is extended by a factor G_X under which the DM field X transforms non-trivially,

$$G_{\text{DMFV}} = G_{\text{MFV}} \times G_X. \tag{2.13}$$

In analogy to MFV, in DMFV models the only sources of flavor breaking are the new flavor-violating coupling matrix λ and the SM Yukawa couplings $Y_u,\ Y_d,\ Y_e$. The DM mass matrix and Higgs-portal interactions can therefore be written in terms of a DMFV spurion expansion in λ (and in principle $Y_u,\ Y_d,\ Y_e$, but those enter only at higher order). In this way, the DMFV assumption reduces the number of new parameters in the model while still allowing for the phenomenological implications of a new source of flavor violation.

3 Numerical toolchain

For our phenomenological study, we built a numerical toolchain, illustrated in Fig. 2 and described in this section. For all models summarized in Table 1, we derived the Feynman rules and generated CalcHEP [53] and UFO [54] model files using the Mathematica-based package FeynRules [16]. The toolchain as well as all model files are publicly available on GitHub,[2] where the naming conventions used in the model files are described in Appendix A.

3.1 Dark matter observables

For the automated computation of the DM relic density as well as the direct and indirect detection cross sections, we use micrOMEGAs [17–19], based on our CalcHEP model implementation. Further details are provided in the following subsections.

3.1.1 Relic abundance

We use micrOMEGAs to numerically solve the Boltzmann equation to compute the DM relic density, taking into account coannihilation effects between all relevant particles. While the tool can also accommodate non-standard production mechanisms, such as freeze-in or conversion-driven freeze-out, we focus on the standard scenario of canonical thermal freeze-out in this work.

[2] https://github.com/lena-ra/Flavored-Dark-Matter.

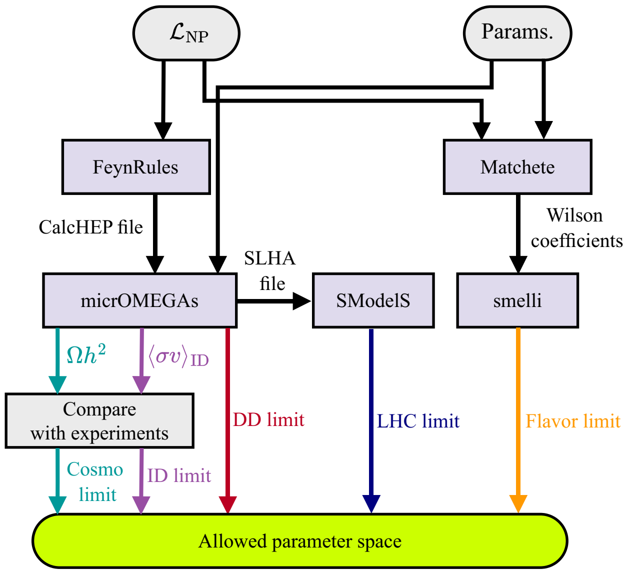

Fig. 2 Illustration of the numerical toolchain used in our analysis of flavored DM models. The gray rounded rectangles show the inputs to the toolchain (i.e. the Lagrangian of the DM model and the values for all parameters) and light purple boxes show the tools used

In this context, we assume that the DM particle is a thermal relic, and that its present-day abundance is set by the freeze-out mechanism and a standard cosmological history. We consider both the case of the computed relic density being consistent with the value measured by the Planck satellite, $\Omega h^2 = 0.120 \pm 0.001$ [55], within an assumed theoretical uncertainty of 10%, as well as the case of underabundant DM. In the latter case the observed relic abundance is assumed to be accounted for by additional DM components. Parameter points that predict overabundant DM are considered experimentally excluded.

3.1.2 Direct detection

Direct detection of DM particles involves observing their rare scattering off a nucleus in a low-background environment. Constraints on the DM scattering cross section have been provided in terms of spin-independent (SI) and spin-dependent (SD) cross sections. Models where DM interacts with quarks are subject to stronger constraints compared to those coupling to leptons. The former give rise to tree-level interactions as well as loop-induced Higgs and gluon interactions relevant in parts of the parameter space. These loop-induced interactions, however, are suppressed for fermionic flavored DM due to the chiral coupling structure, so that one-loop photon and Z-boson penguin and box diagrams become competitive [7,9,10,34]. Leptophilic DM interacts via electroweak loop-diagrams only – typically via photon or Z-boson exchange – which are highly suppressed, in particular, for self-conjugate DM, see e.g. [56].

Table 2 Overview of indirect detection constraints used in this analysis, grouped by cosmic messenger and SM final state. References indicate the sources from which the limits were taken. "–" indicates that no constraint is included for that channel. All bounds assume a Navarro-Frenk-White halo profile, except for [72,74], which use an Einasto profile

Final state	Gamma rays	Antiprotons	Positrons	Neutrinos
e^+e^-	[63,64]	[65]	[66]	–
$\mu^+\mu^-$	[67]	[65]	[66]	[67]
$\tau^+\tau^-$	[68,69]	[65]	[66]	–
$q\bar{q}$ (light)	–	[65,70]	–	–
$c\bar{c}$	[63]	[65]	–	–
$b\bar{b}$	[71]	[65,70]	–	–
$t\bar{t}$	[63,72]	[65]	-	–
W^+W^-	[67,73]	[65,70]	–	–
ZZ	[63,74]	[65]	–	–
hh	–	[65,70]	–	–
$\nu\bar{\nu}$ (any flavor)	–	[65]	–	[75,76]

We calculate both the SI and SD DM-nucleon scattering cross sections using micrOMEGAs.[3] We exclude parameter points that are ruled out at 90% confidence level by the current direct detection experiments that are implemented in micrOMEGAs. This means that for the SI cross sections, we consider constraints from CRESST-III [57], LZ [58], XENON1T [59,60], and DarkSide-50 [61]. For SD cross sections, we include limits from PICO-60 [62].

3.1.3 Indirect detection

Indirect detection experiments constrain the velocity averaged DM annihilation cross section $\langle\sigma v\rangle$ into SM final states by measuring the flux of cosmic messengers such as gamma rays, cosmic-ray antiprotons and positrons, and neutrinos. In our analysis, we use published constraints on annihilation into SM particle-antiparticle pairs derived from experimental data. These results are typically obtained either by the experimental collaborations themselves or by independent phenomenological studies based on publicly available data.

An overview of the indirect detection bounds included in our framework is provided in Table 2, grouped by cosmic messenger and SM final state.

We use micrOMEGAs to compute the total annihilation cross section $\langle\sigma v\rangle$ and the branching fractions into different primary final states, $\mathrm{BR}_{\mathrm{prim}}$. To apply experimental limits, we compute the partial cross section for each final state as

$$\langle\sigma v\rangle_{\mathrm{prim}} = \mathrm{BR}_{\mathrm{prim}} \times \langle\sigma v\rangle, \tag{3.1}$$

[3] The current version of micrOMEGAs does not include DM-nucleon scattering via photon or Z-boson penguin or box diagrams potentially relevant for the leptophilic models. Note that the photon exchange gives rise to operators beyond contact interactions.

and compare it to the corresponding upper limits. Parameter points that yield a cross section above the bound for at least one channel are excluded.

There are two situations in which final states beyond the standard channels listed in Table 2 become relevant. In these cases, we apply approximate mappings that allow us to use the available experimental limits in a controlled way. First, in our models, the DM particle couples to SM flavor triplets, and annihilation through t- or u-channel mediator exchange can result in mixed final states with different SM flavors. Since these mixed channels are not considered in the available constraints, we approximate the cross section limit by using the average from the two corresponding single-flavor pair-annihilation channels:

$$\langle \sigma v \rangle_{AB} = \frac{1}{2}\big(\langle \sigma v \rangle_{AA} + \langle \sigma v \rangle_{BB}\big)\,. \tag{3.2}$$

This is equivalent to the prescription used in MICROMEGAS and can be applied if the DM mass satisfies $M_X > \max(M_A, M_B)$. In reality, mixed final states can occur if $2M_X > M_A + M_B$, but such configurations are not included in this analysis. Simulating both the single-flavor and mixed-flavor annihilation processes with MADDM [77,78], we have verified that the spectrum from the averaged single-flavor channels approximates the mixed-flavor spectrum with sufficient accuracy to justify this approach. (For neutrino final states, we neglect flavor-specific effects and sum over all neutrino flavors, consistent with the assumptions in the experimental bounds.)

Secondly, radiative three-body final states can become relevant. If the two-body final state annihilation is p-wave suppressed, as is the case in the scenarios considered in Sect. 4, it is inefficient in the present Universe and the processes $XX \to \gamma f \bar{f}$ and, for quark-philic models, $XX \to g q \bar{q}$ can provide an important additional contribution, as they lift the p-wave suppression [79,80]. The process $XX \to \gamma f \bar{f}$ is automatically computed by MICROMEGAS. For quark final states, we additionally include $XX \to g q \bar{q}$ using

$$\frac{\sigma_{XX\to q\bar{q}g}}{\sigma_{XX\to q\bar{q}\gamma}} = \frac{C_F}{Q_q^2}\frac{\alpha_s}{\alpha_{em}}\,, \tag{3.3}$$

where $C_F = 4/3$, $Q_q = 2/3$ for up-type quarks and $Q_q = -1/3$ for down-type quarks. Since experimental limits are generally not provided for these three-body final states, we incorporate them by summing the corresponding two- and three-body cross sections and applying the available bound for the associated two-body channel, following Ref. [47]. This amounts to assuming that the continuum part of the spectra from $f\bar{f}\gamma$ and $q\bar{q}g$ is approximated sufficiently well by the corresponding $f\bar{f}$ and $q\bar{q}$ channels for the purpose of applying the published limits. This is also consistent with the analysis underlying Ref. [81], which indicates that radiative three-body spectra in related t-channel mediator models can be approximated reasonably well by standard two-body templates. Possible sharp spectral features from the radiated photon in $f\bar{f}\gamma$ are not included in this treatment and are beyond the scope of the present analysis.

3.2 Collider constraints

Collider searches for new physics can constrain regions of the parameter space where DM and/or its mediator are produced at the LHC. We use the MICROMEGAS interface [20] to SMODELS v3 [21–23] to evaluate these constraints. SMODELS decomposes the full model into simplified model topologies, which are then tested against an extensive database of ATLAS and CMS results. The tool returns r-values, defined as the ratio of the predicted signal cross section to the experimental upper limit, and parameter points with $r \geq 1$ are considered excluded. For searches that provide additional statistical information beyond observed limits, SMODELS can also compute an approximate likelihood for a given parameter point. However, to avoid potential biases from inconsistent likelihood availability across searches, we base our constraints solely on the r-value.

Constraints are typically strongest when the mediator carries QCD charge, as this enhances the production cross section. We also use the SMODELS functionality to identify missing topologies, which are categorized as displaced, prompt, or outside the experimental results grid. This helps reveal gaps in the current experimental coverage that are particularly relevant for the scenario under study.

3.3 Flavor physics

3.3.1 *Effective field theory framework for dark matter models*

Constraints from flavor observables are best explored by mapping the DM models onto their corresponding effective field theory (EFT) description.[4] To this end, we have implemented the different DM models, with their Lagrangians given in Sect. 2, in the MATCHETE package [24], which performs the complete one-loop matching[5] of the DM theories onto the Standard Model Effective Field Theory (SMEFT) [84] in the *Warsaw basis* [85], for reviews see [86–88].

Subsequently, we use the Renormalization Group (RG) equations of the SMEFT [89–91] to evolve the SMEFT Wilson coefficients from the high scale, where the NP param-

[4] A similar approach was also followed in [4] to analyze a t-channel DM model with a flavored mediator. However, in [4] only LEP data was considered in the EFT analysis to constrain the model, whereas our focus here is on flavor observables, while LEP data can be trivially included in our setup.

[5] See [82,83] for other one-loop matching tools with a similar scope.

eters are defined, down to the electroweak scale. In a next step, the SMEFT is matched onto the Low Energy Effective Theory (LEFT) [92,93] and subsequently the coefficients of the LEFT are further run down to the energies of the flavor observables using the LEFT RG equations [94]. The RG evolution and SMEFT-LEFT matching is performed with the help of the WILSON package [27] (see also [95]), and the flavor observables are computed using FLAVIO [26].

The validity of the EFT description depends, of course, on the masses considered for the DM flavor multiplet (X) and the mediator (Y). The EFT constitutes a power series in $E_{\text{obs}}^2/M_{\text{NP}}^2$, where E_{obs} is the typical energy scale of the observables considered and M_{NP} is the mass scale of the NP states (M_X and M_Y). For flavor observables, we typically have $E_{\text{obs}} \le 5\,\text{GeV}$. Therefore, we expect the EFT to provide an accurate description even for DM masses in the range of a few times $10\,\text{GeV}$.[6] Notice, that such low masses are also strongly constrained by collider searches, for which we do not employ an EFT approximation. Thus, first applying the LHC limits before determining the flavor constraints can improve the validity of the EFT description. When also Higgs observables or electroweak precision data are included, E_{obs} is at the electroweak scale and the EFT cannot be expected to yield reliable results for such low DM masses. Thus, these constraints should be applied only for DM masses above a few times $100\,\text{GeV}$, as done, e.g., in [4]. Ultimately, the mass scale up to which the EFT is deemed reliable must be decided individually for each analysis performed with the setup described here. Therefore, this choice is left to the user of the toolchain we provide.

3.3.2 Flavor likelihood

To construct a global flavor likelihood to obtain constraints on the DM models from all relevant flavor observables, we employ a variety of publicly available codes, partially mentioned before already. At the core of the flavor toolchain is the SMELLI package[7] [25], which allows one to compute a global likelihood in the SMEFT parameter space, including not only flavor observables, but also Higgs and electroweak precision measurements. Depending on the concrete scenario one is investigating, it can be convenient to only consider certain subsets of these measurements in the analysis. A complete list of all available observables can be found in Appendix D of [25]. The SMELLI code is based on the FLAVIO software [26] to compute flavor observables and on the WILSON package [27] to perform the RG evolution in the SMEFT and LEFT, and the matching between the two EFTs.

The input to SMELLI is provided in terms of `WCxf` files [96] containing the numerical values of all SMEFT Wilson coefficients, corresponding to a specific point in the NP parameter space, at the high UV scale. This input scale is set to 1 TeV for the analyses presented in this article, but can be modified in the toolchain as desired. These `WCxf` files are generated through a new interface to the MATCHETE package [24], which was developed specifically for this project, but can also be used for any other NP theory. This interface will be included and documented in the MATCHETE code from v0.4.2 onward. For a given point in NP parameter space, the interface numerically evaluates the one-loop matching conditions determined by MATCHETE, thus obtaining a list of numerical values for all Warsaw basis Wilson coefficients. The results are subsequently written into `WCxf` files (one file per parameter point), which is then used as input to SMELLI to compute the global likelihood for the specified point. The details of the parameter scan are, of course, specific to the scenario that is being investigated. Therefore, generating the NP parameter points used as input by the interface is left external to the toolchain.

Detailed instructions and examples on how to use the MATCHETE–`WCxf` interface[8] for the DM models considered here, and for how to subsequently analyze these files with SMELLI, are provided on GitHub.[2]

For every parameter point, SMELLI computes and returns the global log-likelihood ratio, which is defined as

$$\Delta\mathcal{L} = \log\left(\frac{\mathcal{L}_{\text{NP}}}{\mathcal{L}_{\text{SM}}}\right), \tag{3.4}$$

where $\mathcal{L}_{\text{SM}}$ is the likelihood of the SM and $\mathcal{L}_{\text{NP}}$ is the likelihood of the NP model at the specified parameter point. For the analysis presented in this article, we reject all points with $\Delta\mathcal{L} < -2$, that is, the parameter points that fit the data worse than the SM with a pull of approximately $2\,\sigma$ with respect to the SM fit. The threshold for rejecting or accepting points based on the value of the log-likelihood ratio can be easily modified if required. While additional information on all computed observables is available through SMELLI in principle, our toolchain also provides a summary of the most relevant observables for every analysis.

[6] For DM masses below the weak scale ($M_{\text{NP}} < v$), the SMEFT expansion in v^2/M_{NP}^2 suffers an apparent breakdown. However, since we subsequently match onto the LEFT and evolve to energies at or below the B-meson scale, the SMEFT expansion is always supplemented by the LEFT expansion in E_{obs}^2/v^2. Hence, in combination, we find that the relevant observables have an expansion in $(E_{\text{obs}}^2/v^2) \times (v^2/M_{\text{NP}}^2) = E_{\text{obs}}^2/M_{\text{NP}}^2$ such that neglected higher-order SMEFT operators are still sufficiently suppressed as long as $E_{\text{obs}} \ll M_{\text{NP}}$, which validates our SMEFT expansion a posteriori.

[7] For the present analyses we use v2.4.2 of the SMELLI code.

[8] This interface is also documented in detail within the MATCHETE package.

3.3.3 Flavor observables

The SMELLI package allows to include a wide range of observables, which are implemented in FLAVIO, in the global likelihood analysis. The different types of available measurements include quark flavor observables, anomalous magnetic moments of leptons, neutrino trident production, charged- and neutral-current lepton-flavor-universality tests, and lepton-flavor-violation (LFV) tests, but also electroweak precision observables (EWPO) and Higgs decays. A list of all available observables can be found in Appendix D of [25] with an up-to-date version on GitHub.[9]

Which of the observables are the most relevant depends heavily not only on the model considered but also on the specifics of the parameter scan. For example, if the DM couples only to the quark fields (q, u, d) the strongest constraints on the parameter space are presumably derived from meson-anti-meson mixing observables (D^0-$\bar{D}^0$ mixing in the up sector or $B^0_{d,s}$-$\bar{B}^0_{d,s}$ and K^0-$\bar{K}^0$ in the down sector, cf. Sect. 4.3), at least when the parameter scan allows sufficiently large contributions to these $\Delta F = 2$ processes. For leptophilic scenarios, on the other hand, the most stringently constrained charged-lepton flavor-violating observables such as $\mu \to e\gamma$ or $\mu \to eee$ are likely to provide the strongest limits on the parameter space, if the scan allows for LFV, cf. Sec. 4.2. If this is not the case, EWPO can potentially give the leading constraints on the models (see, e.g., [4]).

Ultimately, the relevant observables have to be determined model-by-model and scan-by-scan. Notice that once this is done, it can be useful to restrict SMELLI to compute only the relevant parts of the likelihood, in order to improve performance.

4 Applications and results: majorana dark matter

In this section, we apply our toolchain to two models of Majorana flavored DM which have not yet been studied in the literature. In Sect. 4.2 we examine the coupling to right-handed charged leptons,[10] and in Sect. 4.3 we consider the case of a coupling to the right-handed down-type quarks. In both cases, we assume DMFV, i.e., we assume λ to be the only new source of flavor and CP violation. First, we describe the parametrization framework of λ in Sect. 4.1.

[9] https://github.com/smelli/smelli/tree/master/smelli/data/yaml.

[10] While Majorana flavored DM coupled to right-handed charged leptons has been considered before, the analysis of [46] was restricted to the coupling to only a single SM generation, and [15] dealt exclusively with the possibility of obtaining conversion-driven leptogenesis.

4.1 General parameterization of the coupling matrix and masses

In this study, we make use of the parameterization framework for the matrix λ introduced in [36], which we summarize here for completeness. All expressions relevant for our analysis are presented below, and the reader is referred to [36] for additional context and discussion. Note that this parameterization can be used in all DMFV models with real DM. A useful parameterization for complex DM in DMFV has been derived in [9]. It can be obtained from the one for real DM by removing the orthogonal matrix O and the diagonal matrix d which become unphysical in the complex DM case.

The coupling matrix λ is expressed in terms of two diagonal matrices D and d, an orthogonal matrix O, and a unitary matrix U, respecting the flavor symmetry group $O(3)$:

$$\lambda = U\,\mathrm{diag}(D_1, D_2, D_3)\, O\, \mathrm{diag}(d_1, d_2, d_3)\,. \tag{4.1}$$

The unitary matrix U is constructed as a product of three unitary rotations:

$$\begin{aligned} U &= U_{23}\, U_{13}\, U_{12} \\ &= \begin{pmatrix} 1 & 0 & 0 \\ 0 & c^\theta_{23} & s^\theta_{23} e^{-i\delta_{23}} \\ 0 & -s^\theta_{23} e^{i\delta_{23}} & c^\theta_{23} \end{pmatrix} \begin{pmatrix} c^\theta_{13} & 0 & s^\theta_{13} e^{-i\delta_{13}} \\ 0 & 1 & 0 \\ -s^\theta_{13} e^{i\delta_{13}} & 0 & c^\theta_{13} \end{pmatrix} \\ &\quad \begin{pmatrix} c^\theta_{12} & s^\theta_{12} e^{-i\delta_{12}} & 0 \\ -s^\theta_{12} e^{i\delta_{12}} & c^\theta_{12} & 0 \\ 0 & 0 & 1 \end{pmatrix}, \end{aligned} \tag{4.2}$$

where $c^\theta_{ij} = \cos(\theta_{ij})$ and $s^\theta_{ij} = \sin(\theta_{ij})$. Similarly, the orthogonal matrix O is defined as

$$\begin{aligned} O = O_{23}\, O_{13}\, O_{12} &= \begin{pmatrix} 1 & 0 & 0 \\ 0 & c^\phi_{23} & s^\phi_{23} \\ 0 & -s^\phi_{23} & c^\phi_{23} \end{pmatrix} \begin{pmatrix} c^\phi_{13} & 0 & s^\phi_{13} \\ 0 & 1 & 0 \\ -s^\phi_{13} & 0 & c^\phi_{13} \end{pmatrix} \\ &\quad \begin{pmatrix} c^\phi_{12} & s^\phi_{12} & 0 \\ -s^\phi_{12} & c^\phi_{12} & 0 \\ 0 & 0 & 1 \end{pmatrix}, \end{aligned} \tag{4.3}$$

with $c^\phi_{ij} = \cos(\phi_{ij})$ and $s^\phi_{ij} = \sin(\phi_{ij})$. The diagonal unitary matrix d is given by

$$d = \mathrm{diag}(e^{i\gamma_1}, e^{i\gamma_2}, e^{i\gamma_3})\,. \tag{4.4}$$

In total, the coupling matrix λ is characterized by the following 15 parameters:

$$\theta_{23}, \theta_{13}, \theta_{12}, \phi_{23}, \phi_{13}, \phi_{12}, \delta_{23}, \delta_{13}, \delta_{12}, \gamma_1, \gamma_2, \gamma_3, D_1, D_2, D_3. \tag{4.5}$$

The DM mass matrix is parameterized in terms of λ via the DMFV spurion expansion:

$$\tilde{M}_{\tilde{\chi}} = M_{\tilde{\chi}} \left[\mathbb{1} + \frac{\eta}{2}(\lambda^\dagger \lambda + \lambda^\intercal \lambda^*) + \mathcal{O}(\lambda^4) \right] . \tag{4.6}$$

To diagonalize $\tilde{M}_{\tilde{\chi}}$, we apply the Autonne–Takagi factorization, yielding an orthogonal matrix W such that

$$\tilde{M}_{\tilde{\chi}} = W^\intercal \tilde{M}^D_{\tilde{\chi}} W , \tag{4.7}$$

with $\tilde{M}^D_{\tilde{\chi}} = \text{diag}(M_{\tilde{\chi}1}, M_{\tilde{\chi}2}, M_{\tilde{\chi}3})$ ordered such that $M_{\tilde{\chi}1} < M_{\tilde{\chi}2} < M_{\tilde{\chi}3}$. The coupling matrix is accordingly rotated to the mass eigenbasis via $\tilde{\lambda} = \lambda W^\intercal$. Note that for vanishing phases γ_i ($d = \mathbb{1}$) the orthogonal transformation O simply amounts to a dark flavor symmetry transformation and is hence redundant such that $W = O$; see Appendix B.1 for further details on the dark flavor basis transformation.

Unlike previous analyses of Majorana flavored DM with DMFV in [14,36], we allow for interactions of the mediator with the Higgs doublet, which modify the mediator's physical mass after EWSB. The nature of this correction depends on the mediator's gauge quantum numbers as discussed in Sect. 2.

4.2 Coupling to right-handed charged leptons

4.2.1 Scan setup

We consider a Majorana fermion DM flavor-triplet field and scalar mediator coupling to right-handed charged leptons. We perform a random scan of the model parameters as presented in Table 3 where the prior indicates whether the parameters are sampled linearly (lin) or logarithmically (log) in their scan range.[11] To suppress LFV decays like $\mu \to e\gamma$, the mixing angles θ_{12} and ϕ_{12} are scanned logarithmically over $[10^{-6}, 10^{-2}]$. Because the mass matrix depends on the sign of η, which can be negative, we discard parameter points where the lightest mass eigenstate has a negative mass, guaranteeing $M_{\tilde{\chi}1} > 0$.

4.2.2 Constraints and results

We generate approximately 350,000 points and sequentially apply constraints from relic density, direct and indirect detection, collider searches (via MICROMEGAS and SMODELS), and flavor observables (MATCHETE, SMELLI). The results are presented in Figs. 3, 4 and 5. Points surviving all constraints are shown with lime green circles in Fig. 4. The top left panel displays allowed values in the $(M_{\tilde{\chi}1}, M_\varphi)$ plane, with the gray dashed line denoting the minimal mediator mass. The top right panel shows the allowed mass-splitting parameter η versus $M_{\tilde{\chi}1}$. The bottom panels present viable couplings in terms of the absolute value of the sum over all DM states of $\tilde{\lambda}_{\mu i}\tilde{\lambda}^*_{ei}$ on the left and $\tilde{\lambda}_{\tau i}\tilde{\lambda}^*_{ei}$ on the right for a given M_φ. Points excluded by specific constraints are shown with square-shaped markers in blue (collider) and orange (flavor).

Relic density constraints: In Fig. 3 we show the calculated relic density in two different projections of the parameter space, as described in the figure caption. Parameter points that predict overabundant DM have been discarded and are not shown. We observe that the minimum allowed value of the coupling strength $\sqrt{D_1^2 + D_2^2 + D_3^2}$ increases with increasing mediator mass M_φ, and that larger couplings tend to favor underabundant DM. Furthermore, the calculated relic abundance depends on the mass splitting between DM and mediator, $M_\varphi/M_{\tilde{\chi}1} - 1$. For sizable coupling strengths, $\sqrt{D_1^2 + D_2^2 + D_3^2} \gtrsim 2$, the mass splitting required to reproduce the observed relic density increases.

In the following, unless stated otherwise, we focus on the case in which the model reproduces the full observed DM abundance. We return to the case of underabundant DM at the end of this subsection. Requiring the model to reproduce the observed relic density poses a fairly restrictive constraint in our parameter space scan. We find that approximately 97% of the scanned points fail to yield the measured DM abundance within the assigned theoretical uncertainty. Given the large fraction of excluded points, we only show those that satisfy this constraint in Fig. 4. The dominant contribution to the relic abundance stems from coannihilations between the

Table 3 Ranges and priors for the parameters for the scan with couplings to right-handed leptons. The priors indicate whether the scan range is sampled linearly (lin) or logarithmically (log). The upper part of the table shows the parameters needed for the couplings and the lower part shows the mass parameters

Parameter	Range	Prior
D_i	$[0, 2]$	lin
θ_{12}	$[10^{-6}, 10^{-2}]$	log
θ_{13}	$[10^{-4}, \pi/4]$	log
θ_{23}	$[10^{-4}, \pi/4]$	log
ϕ_{12}	$[10^{-6}, 10^{-2}]$	log
ϕ_{13}	$[10^{-4}, \pi/4]$	log
ϕ_{23}	$[10^{-4}, \pi/4]$	log
δ_{ij}	$[0, 2\pi)$	lin
γ_i	$[0, 2\pi)$	lin
$\lambda_{\varphi H,1}$	$[-1, -0.001] \cup [0.001, 1]$	log
η	$[-1, -0.001] \cup [0.001, 1]$	log
$M_{\tilde{\chi}}$ [GeV]	$[100, 1500]$	lin
M_φ [GeV]	$[M_{\tilde{\chi}1}, M_{\tilde{\chi}1} + 2000]$	lin

[11] We note that to cover the full physical parameter space, one of the angles ϕ_{ij} should cover both positive and negative values between 0 and $\pm\pi/4$. We have checked that restricting our scans to include only positive values does not impact our results.

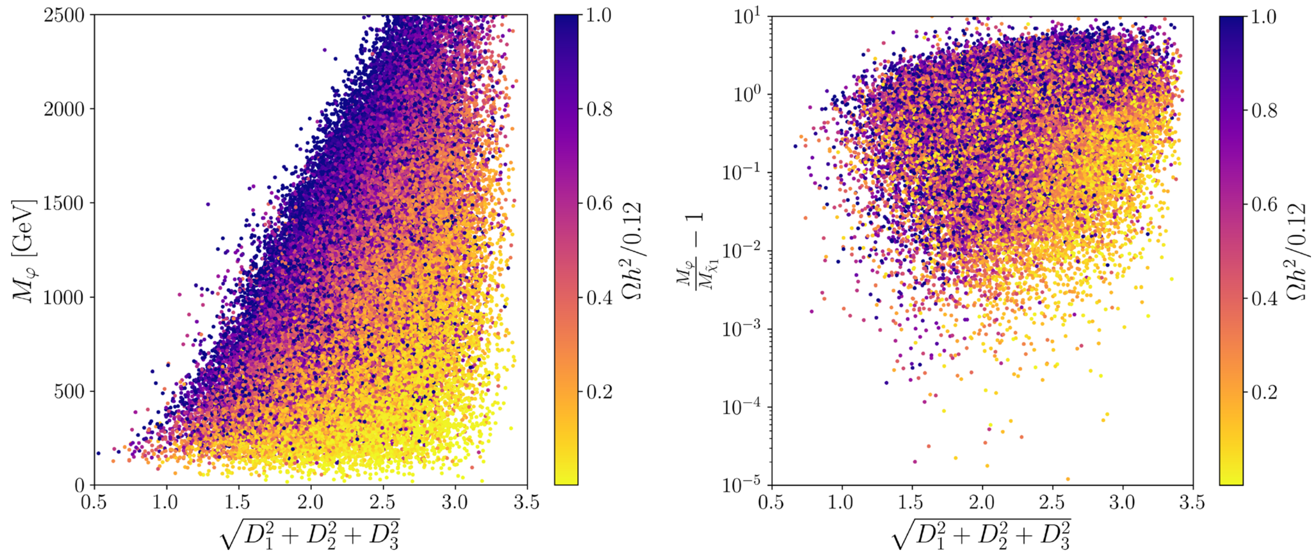

Fig. 3 Calculated relic abundance shown in color as indicated by the color scale. The left plot shows the parameter space in the $\sqrt{D_1^2+D_2^2+D_3^2}$-M_φ plane, while the right plot shows the plane of $\sqrt{D_1^2+D_2^2+D_3^2}$ and $M_\varphi/M_{\tilde\chi_1}-1$

different $\tilde\chi_i$ states into leptons, mediated by t- and u-channel exchange of the scalar mediator. For small couplings, however, the main process for DM depletion is mediator pair annihilation into photons as the DM particles and the mediator are still in thermal equilibrium because they are almost mass degenerate.

A key feature of the viable points is a lower bound on the DM mass $M_{\tilde\chi_1}$ for a given mediator mass. This behavior arises from the scaling of the annihilation cross section, which roughly grows as $M_{\tilde\chi_1}^2/M_\varphi^4$ in the limit of sizable mass splittings and fixed couplings. Since the mediator mass M_φ is bounded from below, this scaling implies that for sufficiently small $M_{\tilde\chi_1}$, the annihilation cross section becomes too small to yield the correct relic abundance, even when the coupling matrix elements D_i saturate their maximal values. This effect is reflected in the absence of points in the lower right area in the upper left panel of Fig. 4.[12]

We also observe a dependence of the allowed points on the mass splitting parameter η. Large positive values of η are allowed across the entire mass range of $M_{\tilde\chi_1}$, whereas large negative values are only compatible with small DM masses. This is because in our scan we choose the upper value for $M_{\tilde\chi}$ to be 1500 GeV meaning that for $\eta<0$ the individual values for the masses $M_{\tilde\chi_i}$ will be smaller than 1500 GeV. For $M_{\tilde\chi_1}$ to be close to 1500 GeV if the absolute value for $\eta<0$ is large, very small couplings are needed to have very small mass splittings. In this case, the relic abundance becomes too large so that these points are excluded. Note that the region with $M_{\tilde\chi_1}<100$ GeV is only populated for negative η since $M_{\tilde\chi}\geq 100$ GeV. Note also that the absence of points in the lower-left corner in the upper left panel of Fig. 4 at $M_\varphi \lesssim 200$ GeV (and relatively small mass splittings) is due to the relic abundance being too low in this region, as efficient coannihilation with the mediator over-depletes the DM density even for small DM couplings; this region could, however, become viable in the regime of conversion-driven freeze-out for very small couplings $\lesssim 10^{-6}$.[13]

Collider constraints: We now turn to constraints from LHC searches, evaluated using SModelS. These searches exclude only 0.3% of the parameter points that have the correct relic abundance, all confined to the low-mass region with $M_{\tilde\chi_1}<200$ GeV and $M_\varphi<500$ GeV (see upper left panel of Fig. 4), while the bulk of the parameter space remains unconstrained. This result is similar to the findings of Ref. [47,48], where complex scalar DM coupling to right-handed leptons was studied.

As seen in the upper right panel of Fig. 4, points with negative η and small $M_{\tilde\chi_1}$ are most affected.[14] For negative η, $\tilde\chi_1$ has the largest coupling, leading to dominant mediator decays into $\tilde\chi_1$ and leptons, resulting in two-lepton plus missing energy signatures well covered by SModelS. For positive η, by contrast, the mediator decays dominantly into heavier $\tilde\chi_i$ states, which subsequently undergo cascade decays producing multi-lepton final states not covered by current searches implemented in SModelS. As a result, the parameter space with negative η is more effectively constrained,

[12] Note that the unpopulated region extends beyond the region that is not covered by our parameter scan.

[13] See Refs. [15,46] for a respective analysis in the case of two DM flavors.

[14] Note that our scan setup does not cover the mass range $M_{\tilde\chi_1}<100$ GeV for positive η.

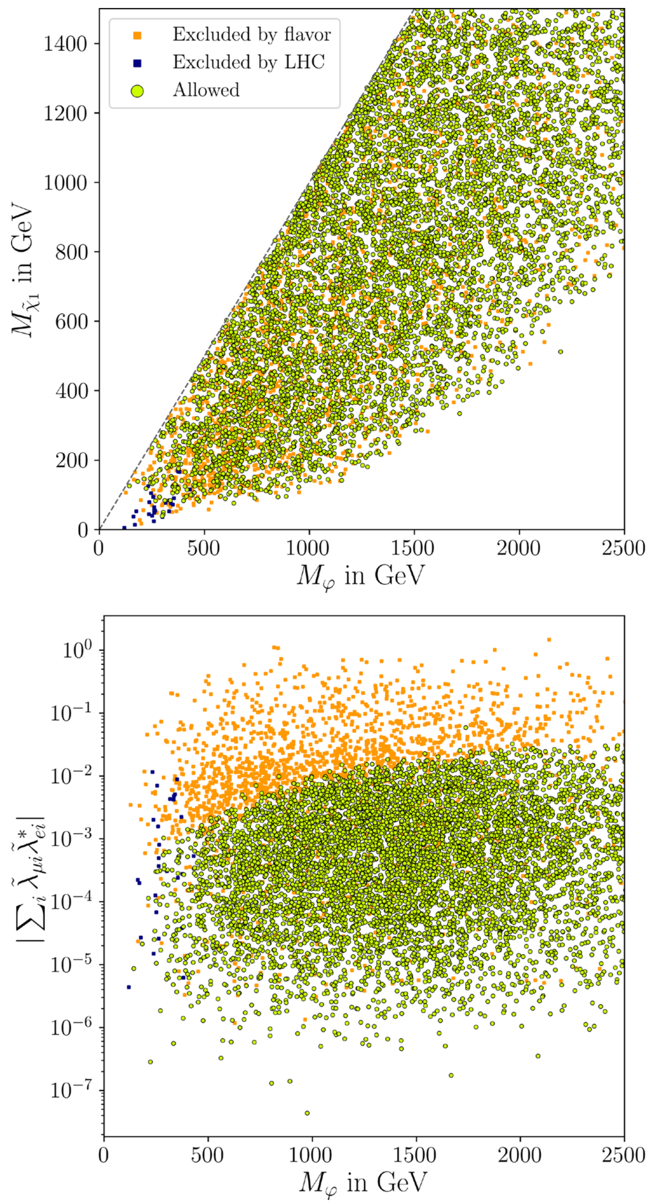

Fig. 4 Constraints on the parameter space for the Majorana DM model coupling to right-handed leptons. Points shown by orange square markers are excluded by flavor observables while still passing the LHC and relic abundance constraints. Blue square markers fulfill only the relic abundance constraints but are excluded by constraints from the LHC. The remaining points that pass all constraints are shown with green circles. The upper left panel shows the parameter space in the $M_{\tilde{\chi}_1}$-M_φ plane, with the gray dashed line indicating $M_{\tilde{\chi}_1} = M_\varphi$. The upper right panel displays the mass splitting parameter η versus $M_{\tilde{\chi}_1}$. The lower panels show the sum over all DM states of $\tilde{\lambda}_{\mu i}\tilde{\lambda}^*_{ei}$ on the left and $\tilde{\lambda}_{\tau i}\tilde{\lambda}^*_{ei}$ on the right versus M_φ

although dedicated multilepton searches could significantly enhance sensitivity.

The dominant LHC signal arises from Drell-Yan production of mediator pairs decaying to leptons and missing energy. Although Majorana DM allows for same-sign dileptons, these are suppressed by initial-state statistics [97], and dedicated searches are lacking. Mixed-flavor channels are also possible [47] but to our knowledge are not covered by experimental searches and are not included in SModelS. These channels are also the most frequently identified prompt missing topologies by SModelS, suggesting that these merit further experimental attention.

The most stringent constraint comes from a CMS search for two same-flavor, opposite-sign light leptons plus missing energy ($\not{E}_T$) [98], which excludes points with large $\tilde{\chi}_1$-μ couplings. Other searches [99, 100] are less sensitive, excluding only one point with large $\tilde{\chi}_1$-e couplings. Searches for

$\tau\bar{\tau} + \not{E}_T$ exclude no points, explaining why large $\tilde{\chi}_1$-τ couplings remain allowed.

Finally, as the model couples to right-handed leptons, lepton colliders like LEP can constrain it via $e^+e^- \to \tilde{\chi}_i\tilde{\chi}_j\gamma$ resulting in mono-photon + $\not{E}_T$ signatures. While not included in SModelS, we expect LEP to set a lower bound of about 100 GeV on the mediator mass [101], which we find to be respected by all points satisfying the relic abundance constraint in our scan.

Direct detection constraints: In lepton-flavored DM models, tree-level interactions with nuclei are absent, making direct detection constraints significantly weaker than in scenarios with quark couplings. The only possible contributions arise from scattering off electrons or from loop-induced couplings to nuclei. The latter proceeds dominantly through photon exchange via the anapole operator. However, following the findings of Ref. [56], we do not expect the current experimental data to impose constraints on the parameter space.[15]

Indirect detection constraints: Indirect detection experiments impose only weak constraints on our model, with no points satisfying the relic abundance requirement being excluded in our scan. In the leptophilic scenario, the leading two-body annihilation channel $\tilde{\chi}_1\tilde{\chi}_1 \to \ell^+\ell^-$ is p-wave suppressed and hence inefficient in the present Universe. We therefore include the radiative three-body process $\tilde{\chi}_1\tilde{\chi}_1 \to \gamma\ell^+\ell^-$ according to the prescription described in Sec. 3.1.3. Even with this contribution included, no parameter point in our scan is excluded by indirect detection.

Flavor constraints: We finally apply flavor constraints to the points that remain after imposing relic density and collider bounds. These observables exclude an additional $\sim 25\%$ of the parameter space, as shown in orange in Fig. 4. The most stringent bound arises from the LFV decay $\mu \to e\gamma$ [103], with $\mu \to eee$ [103] providing a complementary constraint. While the latter can occur via internal photon conversion in $\mu \to e\gamma$, its dominant contribution stems from Z-penguin and in particular box diagrams involving φ and $\tilde{\chi}_i$. This observable has not been included in previous analyses of Dirac [44] or scalar [47] lepton-flavored DM.

As expected, LFV constraints are stronger at low mediator and DM masses, where loop contributions are less suppressed. This is illustrated in Fig. 5, where we show, in each bin of the $M_{\tilde{\chi}_1}$-M_φ plane, the largest value of the coupling combination entering $\mu \to e$ flavor transitions found among the flavor-allowed points in our scan. This provides a scan-based estimate of the maximally allowed coupling strength as a function of the DM and mediator masses. Moreover, the upper right panel of Fig. 4 seems to show a bias toward excluding points with small absolute values of η, though this is a scan artifact due to the logarithmic prior and linear plotting scale. The exclusion fraction is in fact independent of the value of η.

[15] An interpretation of XENON1T, SuperCDMS and CRESST-III data in terms of the anapole moment can be found in [102].

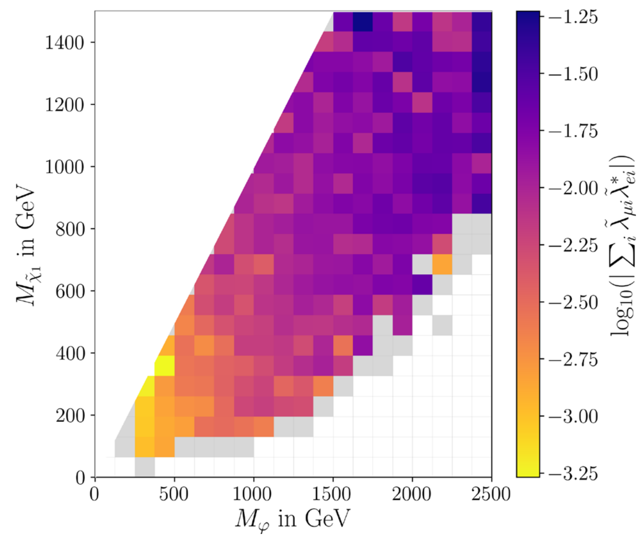

Fig. 5 Largest (absolute) value of the sum over all DM states of $\tilde{\lambda}_{\mu i}\tilde{\lambda}^*_{ei}$ found among the flavor-allowed points in each bin of the $M_{\tilde{\chi}_1}$-M_φ plane. This provides a scan-based estimate of the maximally allowed coupling strength in different mass regions. Empty bins are left blank, while bins containing fewer than ten points are shown in gray.

Flavor bounds primarily constrain the structure of the coupling matrix $\tilde{\lambda}$, which controls the size of LFV effects. Large couplings to both the electron and muon are strongly disfavored, as shown in the lower left panel of Fig. 4, while scenarios with hierarchical couplings – where only one of the first two rows of $\tilde{\lambda}$ dominates – can remain viable. The constraint on the relevant coupling parameters weakens with increasing mediator mass as the latter suppresses LFV amplitudes. Constraints from τ LFV decays [103,104] are generally weaker, as seen in the lower right panel of Fig. 4, and only become relevant for small values of M_φ. Even in that case larger $\tilde{\lambda}_{\tau i}$ values remain allowed unless accompanied by a sizable coupling to e or μ.

Underabundant dark matter: In order to assess the impact of the relic density constraint on our results, we also compared the case of our model reproducing the measured abundance with the cases of only 10% or 1% of the observed DM density stemming from our model. As before, we assumed a 10% theoretical uncertainty in the relic density computation. Compared to about 3% of the generated points reproducing the full relic density, in the two underabundant scenarios only 0.4% and 0.03% of points, respectively, pass the corresponding relic density constraint, leading to significantly less statistics for further analysis. At the same time, the preference of underabundant DM for larger coupling strengths tends to enhance the impact of collider

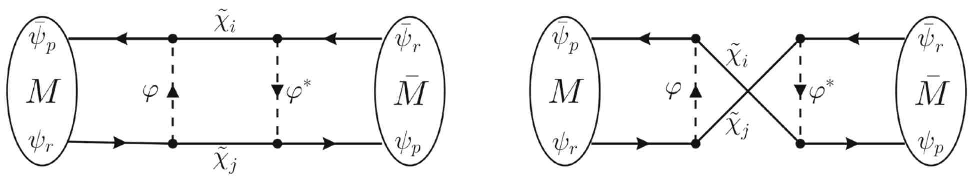

Fig. 6 Feynman diagrams contributing to meson-anti-meson mixing in quarkphilic Majorana DM models. While the diagram on the left-hand side is present also in Dirac models, the diagram on the right-hand side only contributes in the Majorana scenario

and flavor constraints, while direct and indirect detection still exclude no parameter points.

4.3 Coupling to right-handed down-type quarks

As a second example, we investigated again a Majorana-fermion DM field but coupling to right-handed down-type quarks, which has also not been discussed in the literature so far. Because the flavor constraints, particularly meson-anti-meson mixing limits, are even stronger in this case than for the leptophilic model, we perform dedicated scans guided by the insights from Appendix B to efficiently probe the phenomenologically viable regions of parameter space. In the following, we first motivate our scan setup and assumptions, before discussing the results of our analysis.

4.3.1 Scan setups

In order to have a sufficient number of parameter points that meet the strong constraints deriving from $\Delta F = 2$ processes, we have to design an efficient parameter scan setup with care. Since we are dealing with Majorana fermions, the common box diagram shown on the left-hand side of Fig. 6, which contributes to meson-anti-meson mixing, is supplemented by the crossed box diagram shown on the right-hand side of Fig. 6 [36]. The former diagram is proportional to $\tilde{\lambda}_{pi}\tilde{\lambda}^*_{ri}\tilde{\lambda}_{pj}\tilde{\lambda}^*_{rj}$, whereas the latter scales like $\tilde{\lambda}^2_{pi}\,\tilde{\lambda}^{*2}_{rj}$. This indicates that large contributions to $\Delta F = 2$ processes can be present for Majorana models, even if all off-diagonal entries of $\tilde{\lambda}$ vanish. Already the presence of two non-negligible entries of $\tilde{\lambda}$ suffices for a parameter point to be in tension with meson-mixing data.

In practice, this means that we want a strong hierarchy between the eigenvalues of the coupling matrix $\tilde{\lambda}$ in order to sufficiently suppress these flavor-changing processes. We implemented this hierarchy in two different ways that we dub *general hierarchical* and *bottom-philic* scenarios. In the following, we compare both the setups and their results. We start by describing the details of the two scan setups and qualitatively motivating them. A more detailed and quantitative argument for the exact structure of these scans is provided in Appendix B.

General hierarchical scenario: In order to efficiently scan the parameters D_1, D_2, and D_3, which determine the magnitude of the eigenvalues of the coupling matrix λ [cf. Eq. (4.1)], we sample the values such that their product lies within a specified range while allowing for hierarchical structures among them. Specifically, we sample:

- a total scale $d_{\mathrm{mul}} = D_1 D_2 D_3 \in [(10^{-4})^3, 2^3]$ logarithmically, which sets the overall coupling strength of the DM multiplet to the SM, allowing efficient exploration of very small as well as large values;
- two independent ratios $r_{12} = D_1/D_2$ and $r_{23} = D_2/D_3$ logarithmically in the range $[5 \times 10^{-5},\ 2 \times 10^4]$, which ensures that most parameter points obey a hierarchy among the eigenvalues of λ as discussed before.

The individual parameters are obtained as

$$
\begin{aligned}
D_1 &= \left(d_{\mathrm{mul}}\, r_{12}^2\, r_{23}\right)^{1/3}, \\
D_2 &= \left(d_{\mathrm{mul}}\, \frac{r_{23}}{r_{12}}\right)^{1/3}, \\
D_3 &= \left(\frac{d_{\mathrm{mul}}}{r_{12}\, r_{23}^2}\right)^{1/3},
\end{aligned}
\tag{4.8}
$$

and we retain only those points for which all D_i lie within the range $[10^{-4}, 2]$. The upper bound of that range ensures that the UV couplings remain perturbative, whereas the lower bound is chosen conservatively to guarantee that all dark-sector states remain in thermal equilibrium with each other during freeze-out, consistent with the assumptions underlying the standard MICROMEGAS routines used in the scan. The remaining model parameters are scanned according to the ranges and priors listed in Table 4. Note that the mixing angles θ and ϕ are scanned with logarithmic priors, ensuring efficient coverage of small angles.[16]

[16] The structure of the general hierarchical scan is closely related to the first scenario discussed in Appendices B.2 and B.3, where small mixing angles θ_{ij}, ϕ_{ij} are assumed (i.e. suppressed off-diagonal entries in λ). However, for sizable couplings (as required by the relic-density constraint in the bulk of parameter space) small angles alone are not always sufficient to satisfy the bounds from neutral-meson mixing – in particular when $M_\varphi \sim M_{\tilde{\chi}}$, where the box diagram on the right side

Table 4 Ranges and priors for the parameters in the general hierarchical scan scenario with couplings to right-handed down-type quarks. The priors indicate whether the scan range is sampled linearly (lin) or logarithmically (log). The upper part of the table shows the parameters needed for the couplings and the lower part shows the mass parameters

Parameter	Range	Prior
D_i	$[10^{-4}, 2]$	Description in text
θ_{ij}	$[10^{-4}, \pi/4]$	log
ϕ_{ij}	$[10^{-4}, \pi/4]$	log
δ_{ij}	$[0, 2\pi)$	lin
γ_i	$[0, 2\pi)$	lin
$\lambda_{\varphi H,1}$	$[-1, -0.001] \cup [0.001, 1]$	log
η	$[-1, -0.01] \cup [0.01, 1]$	log
$M_{\tilde{\chi}}$ [GeV]	$[100, 1500]$	lin
M_φ [GeV]	$[M_{\tilde{\chi}_1}, M_{\tilde{\chi}_1} + 1600]$	lin

This procedure allows for a wide variety of hierarchies among the D_i, including cases where one parameter is significantly larger than the others, while keeping the geometric mean fixed within a physically relevant range. In addition, we require either $\sqrt{D_1^2 + D_2^2 + D_3^2} > 0.6$ or $M_\varphi/M_{\tilde{\chi}_1} - 1 < 0.1$, as indicated by the dashed lines in the lower left panel of Fig. 7. This condition excludes regions that we found to overshoot the observed relic abundance. Specifically, it ensures that either the overall coupling strength of the DM multiplet to the SM is large enough for efficient $\tilde{\chi}_i \tilde{\chi}_j$ annihilation, or that the mass splitting between the DM state $\tilde{\chi}_1$ and the mediator φ is small enough for efficient coannihilation via the sizable QCD interactions of the mediator. The resulting set of accepted points constitutes our set of *generated* points.

Bottom-philic scenario:

In addition to the rather general scan setup discussed above, covering a wide range of possible hierarchies, it is instructive to consider a more targeted scan focusing on regions that largely evade the bounds from flavor-changing observables.

One such scenario follows a flavor hierarchy, with the DM flavor multiplet coupling dominantly to the bottom quark. This scenario can be interpreted as a toy model representing the large class of NP theories with a dominant coupling to the third generation of SM fermions. A bottom-philic coupling structure can be achieved by assuming the hierarchy $D_3 \gg D_2 \gg D_1$ among the eigenvalues of the coupling matrix λ. In addition, we have to require $\theta_{ij} \ll 1$, i.e., small misalignment between the quark mass basis and the basis

Footnote 16 continued
of Fig. 6 is relevant. In this regime, an additional hierarchy among the diagonal entries of λ is needed, as shown, for instance, in Eq. (B.60) (cf. also the first line in Eq. (B.53), where ϵ corresponds to the size of the small mixing angles θ_{ij}).

Table 5 Scan ranges and priors for all parameters in the bottom-philic scenario with a DM flavor multiplet coupled dominantly to the third generation

Parameter	Range	Prior
D_3	$[10^{-1}, 2]$	lin
ϵ	$[10^{-3}, 0.5]$	log
D_2	$[0.3, 1.3] \times \epsilon\, D_3$	lin
D_1	$[0.3, 1.3] \times \epsilon\, D_2$	lin
θ_{12}	$[0.3, 1.3] \times \epsilon$	lin
θ_{23}	$[0.3, 1.3] \times \epsilon$	lin
θ_{13}	$[0.3, 1.3] \times \epsilon^2$	lin
ϕ_{ij}	$[0, \pi/4]$	lin
δ_{ij}	$[0, 2\pi)$	lin
γ_i	$[0, 2\pi)$	lin
$\lambda_{\varphi H,1}$	$[-1, -0.001] \cup [0.001, 1]$	log
η	$[-1, -0.01] \cup [0.01, 1]$	log
$M_{\tilde{\chi}}$ [GeV]	$[100, 1500]$	lin
M_φ [GeV]	$[M_{\tilde{\chi}_1}, M_{\tilde{\chi}_1} + 1600]$	lin

where λ is diagonal, to ensure the dominant third-generation coupling. In contrast, no special alignment between this matrix and the DM flavor multiplet is required and we typically have $\phi_{ij} = \mathcal{O}(1)$. Following from Eq. (4.1), we find the texture for the coupling matrix

$$\lambda \sim \begin{pmatrix} \epsilon^2 & \epsilon^2 & \epsilon^2 \\ \epsilon & \epsilon & \epsilon \\ 1 & 1 & 1 \end{pmatrix}, \tag{4.9}$$

where $\epsilon \ll 1$ and every entry is, of course, multiplied by an order one number.[17]

This texture can be implemented in a scan in the following way: We start by sampling the largest eigenvalue of λ linearly in $D_3 \in [10^{-1}, 2]$. This choice selects couplings in the ballpark required to obtain the observed relic abundance, thereby improving the efficiency of the scan. Next, we introduce the hierarchy parameter ϵ that we sample logarithmically in $[10^{-3}, 0.5]$. Larger values would yield too large contributions to meson-mixing observables through the box diagrams of Fig. 6, whereas lower values might lead to too small coupling for some of the dark flavors, making the underlying assumption of thermal equilibrium in the dark sector questionable.[18] The other eigenvalues can then be computed using

[17] This scenario is described in Appendix B.2 and B.3 as *Scenario III*. Following this scenario, it could also be interesting to consider setups where the dark sector is dominantly coupled to the first or second generation, i.e., interchanging the rows of Eq. (4.9). We leave these studies for future work.

[18] In our scan, however, we checked that each dark-sector state undergoes at least one efficient inelastic scattering process to maintain chemical equilibrium within the dark sector during freeze-out. For a given

$D_2 = \mathcal{O}(1) \times \epsilon D_3$ and $D_1 = \mathcal{O}(1) \times \epsilon D_2$. As already mentioned, to maintain that the flavor multiplet is predominantly coupled to the bottom quark, we have to additionally ensure small rotation angles ($\theta_{ij} \ll 1$). This is achieved requiring $\theta_{12} = \mathcal{O}(1) \times \epsilon$, $\theta_{23} = \mathcal{O}(1) \times \epsilon$, and $\theta_{13} = \mathcal{O}(1) \times \epsilon^2$.

The remaining scan parameters are left unchanged with respect to the general hierarchical scan scenario, except for the angles ϕ_{ij}, for which the scan range remains the same but they are scanned linearly in the bottom-philic scenario, since we aim at sampling $\phi_{ij} = \mathcal{O}(1)$ mixing angles. The complete list of all scan ranges and priors used in this scenario is summarized in Table 5. More details on the specific values chosen in the scan and a more thorough motivation for this specific setup are provided in Appendix B.

4.3.2 Constraints and results

We generate 250,000 points in both scans and apply the relic density, direct and indirect detection, collider, and flavor constraints discussed in the following. The results for both scans are presented in Figs. 7, 8, 9 and 10, where the general hierarchical scenario is shown on the left and the bottom-philic scenario on the right. The color coding for the constraints is the same as for the leptophilic case, with the addition of direct-detection constraints shown in red.

Relic density constraints: The parametric dependence of the calculated relic density is displayed in Fig. 7, where, as in the leptophilic model, we discarded parameter points predicting overabundant DM. We observe a qualitatively similar picture, with larger coupling strengths as well as smaller masses and mass splittings implying a smaller theoretical value for the relic abundance. However, due to the increased importance of mediator (co)annihilation effects sensitive to the strong coupling constant, the quantitative picture changes.

In the following, unless stated otherwise, we focus on the case in which the model reproduces the full observed DM abundance, and we return to the case of underabundant DM at the end of this subsection. Requiring the model to account for the full relic density remains the most stringent selection criterion in the down-type quark scenario, excluding about 99% of the generated points within our assumed 10% theoretical uncertainty.[19] Only the surviving points are shown in the plots. The interplay between coupling strength and masses in Fig. 7, where $\sqrt{D_1^2 + D_2^2 + D_3^2}$ serves as a proxy for the overall interaction strength of the DM multiplet with the SM, and $M_\varphi/M_{\tilde{\chi}_1} - 1$ quantifies the relative mass splitting that controls the relevance of mediator coannihilations. Small couplings $\sqrt{D_1^2 + D_2^2 + D_3^2} < 1$ can provide the correct relic abundance for mediator masses $M_\varphi \lesssim 1.5$ TeV, as indicated by the upper panels of the figure. The lower panels show that for large splittings, $M_\varphi/M_{\tilde{\chi}_1} - 1 \gtrsim 0.1$, achieving the observed relic abundance requires sizable couplings of order unity, while for smaller splittings efficient coannihilation with the mediator allows for smaller coupling strengths. The region with very small values of $\sqrt{D_1^2 + D_2^2 + D_3^2}$ corresponds to regimes where mediator pair annihilations dominate the depletion of the dark sector while DM is kept in chemical equilibrium with the mediator by efficient conversion processes. This region is only populated to a noticeable extent in the general hierarchical scan, owing to the logarithmic prior on the product of the D_i, whereas in the bottom-philic scan the linear prior on $D_3 > 0.1$ prevents access to very small effective couplings.

Similar to the leptophilic case (see Sect. 4.2), the region of large mass splittings ($M_\varphi - M_{\tilde{\chi}_1}$) corresponds to suppressed annihilation cross sections, causing the relic density to exceed the observed value and, hence, leaving a non-accessible region in the lower-right corner of the upper panels of Fig. 8.[20]

The allowed parameter space further shows a preference for negative values of the mass-splitting parameter η, see lower panels of Fig. 8. Positive η implies that the lightest DM state couples weakest to the SM, such that obtaining the correct relic density would rely on coannihilation among different $\tilde{\chi}_i$ flavors. Because these processes are suppressed in the hierarchical flavor structure, viable points predominantly feature negative η, where the lightest state couples most strongly and can efficiently annihilate without relying on coannihilations. Coannihilation with the mediator φ may still occur for small mass splittings but remains somewhat disfavored by the linear mass priors used in our scans. Despite structural differences, both scan setups yield very similar viable regions under the relic-density constraint, as the freeze-out dynamics depends mainly on the total coupling strength and masses rather than on the detailed flavor pattern. This is expected since in the bulk of the parameter space the typical freeze-out temperature exceeds the bottom-quark mass, so all quark flavors the dark sector couples to behave effectively alike.

Collider constraints: We now turn to collider constraints from LHC searches, evaluated using SModelS, with excluded points shown in blue in all figures. In the case of

Footnote 18 continued
state $\tilde{\chi}_j$, it typically requires one coupling $\tilde{\lambda}_{ij} \gtrsim 10^{-6}$; see [12] for a detailed discussion. In fact, we specifically observe $\tilde{\lambda}_{sj} > 10^{-5}$ for all cosmologically viable parameter points in the scan.

19 Note that the nearly identical number of points rejected by the relic density in the two scenarios – occurring despite the different scan setups described in Sect. 4.3.1 – is largely coincidental.

20 We have checked in an exploratory scan allowing for larger M_φ values that our choice for the mass range of M_φ does not cut into the accessible region.

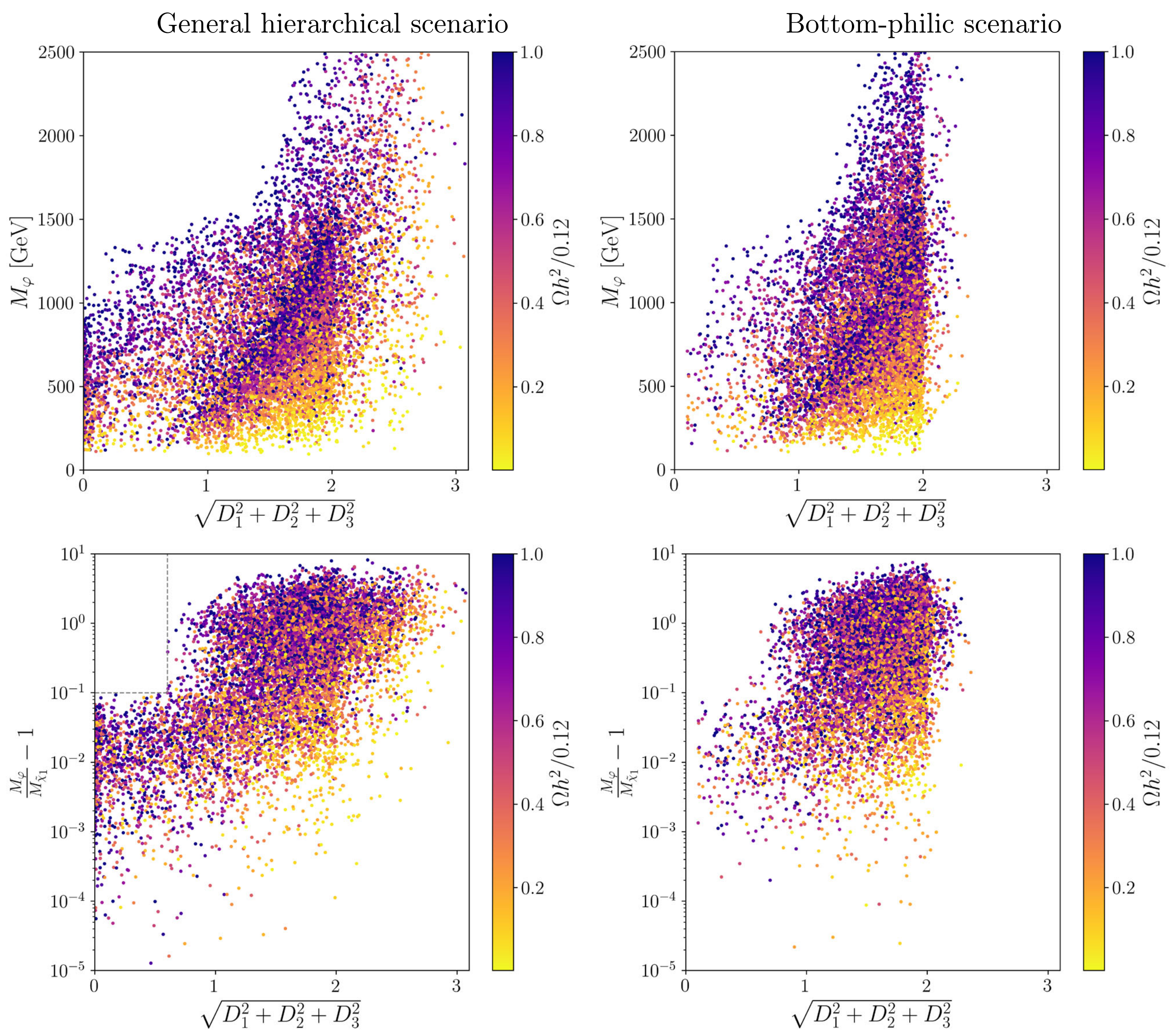

Fig. 7 Calculated relic density in the $\sqrt{D_1^2+D_2^2+D_3^2}$ - M_φ plane (upper panels) and in the $\sqrt{D_1^2+D_2^2+D_3^2}$ - $(M_\varphi/M_{\tilde\chi_1}-1)$ plane (lower panels) for the Majorana DM model coupling to right-handed down-type quarks. The left panel shows the results for the general hierarchical scenario and the right panel shows the ones for the bottom-philic scenario. The dashed gray lines in the left panel depict the region excluded in the general hierarchical scan by requiring either $\sqrt{D_1^2+D_2^2+D_3^2}>0.6$ or $M_\varphi/M_{\tilde\chi_1}-1<0.1$

the model coupling to down-type quarks, these constraints are significantly more restrictive, excluding 30.1% of the parameter points that satisfy the relic abundance requirement in the general hierarchical scan and 23.9% in the bottom-philic scenario. The exclusion reaches up to masses of $M_{\tilde\chi_1}\approx 1100\,\mathrm{GeV}$ (600 GeV) and $M_\varphi\approx 1900\,\mathrm{GeV}$ (1100 GeV) in the most extreme case for the general hierarchical (bottom-philic) scenario. The dominant LHC signal originates from pair production of the scalar mediators, both through QCD interactions and via t-channel exchange of $\tilde\chi_i$, followed by their decay into a DM particle and a down-type quark. The latter production channel is particularly relevant for large $\tilde\lambda_{di}$ couplings as it is enhanced by the down-quark content of the proton.[21] In the general hierarchical scenario all generations of down-type quarks are possible in the final state, depending on the specific hierarchy of a given parameter point. On the contrary, the bottom-philic scenario is dominated by the b-quark final state, which explains the lower energy reach of the collider limits in this case.

[21] For a sizable Majorana mass $M_{\tilde\chi_i}$ the same-sign process $dd\to\varphi\varphi$ becomes dominant in this case [14,36].

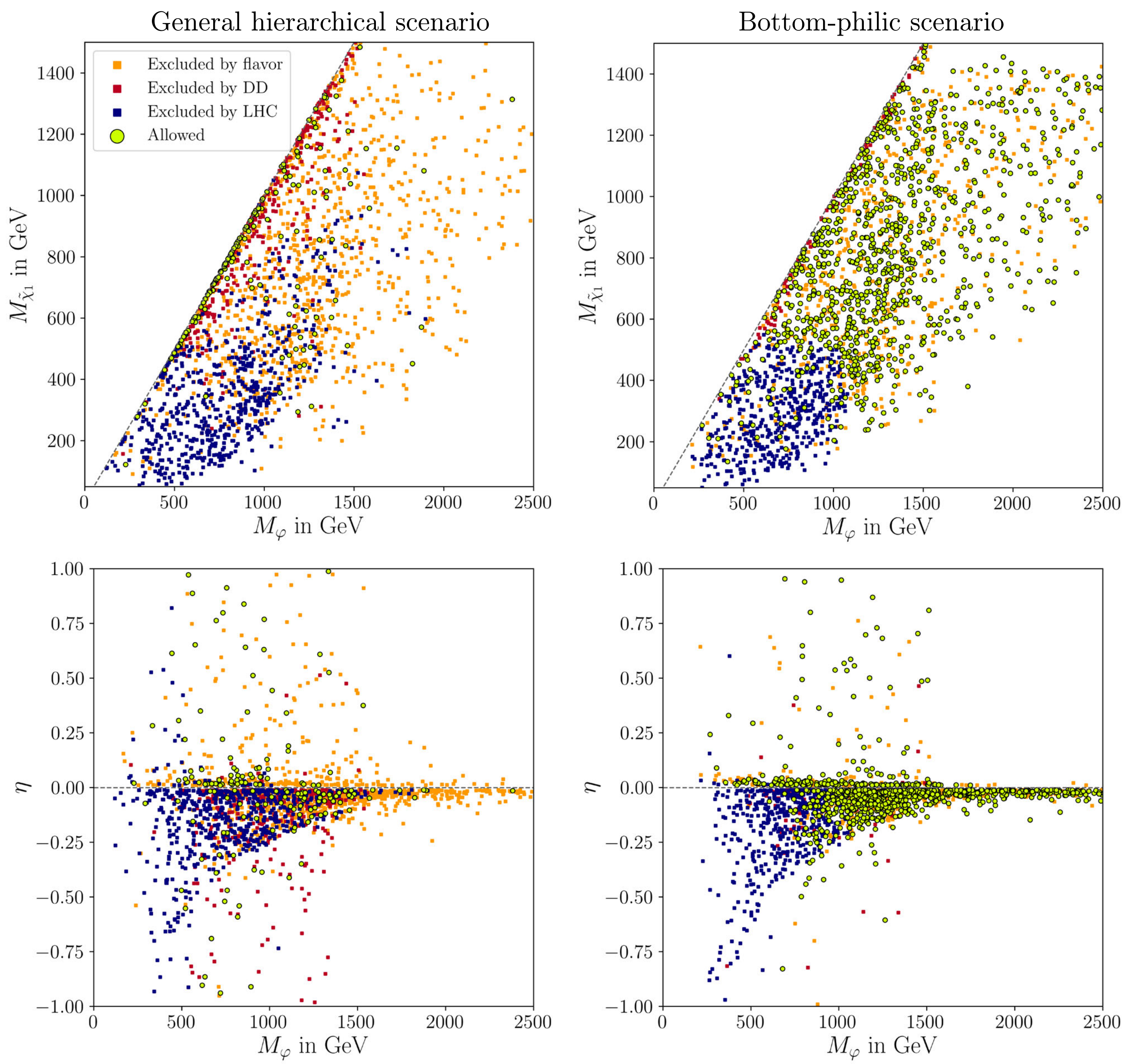

Fig. 8 Comparison of the constraints in the general hierarchical scenario (left) and the bottom-philic scenario (right). The upper panels show the $M_{\tilde{\chi}_1}$-M_φ plane and the lower panels show the η-M_φ plane. The color-code is the same as in Fig. 4 with the addition of direct detection constraints in red

In the general hierarchical scenario, the most constraining searches are ATLAS-SUSY-2018-22 [105] searching only for a di-jet signature plus missing transverse energy ($\not{E}_T$) and CMS-SUS-19-006 [106], CMS-SUS-16-033 [107], and CMS-SUS-16-036 [108] that also target bottom-quark final states and, to a lesser extent, charm-quark final states.[22] Other searches have a weaker impact on the parameter space, excluding comparatively few points in our scan [109–118].

[22] Note that SModelS also determines that the $c\bar{c} + \not{E}_T$ topology becomes relevant for this model due to a peculiarity of the respective CMS searches [108,109]. These do not employ a dedicated charm tagger, but exploit the $\sim$ 10% misidentification rate of charm quarks in the b-jet tagger, which allows one to gain sensitivity on the $c\bar{c} + \not{E}_T$

Footnote 22 continued
channel. This also means that the signal region of $c\bar{c} + \not{E}_T$ is actually identical to the signal region of $b\bar{b} + \not{E}_T$ for this search. Moreover, the CMS analyses investigate stop ($\tilde{t}$) production with the subsequent decay channels $\tilde{t} \to b\tilde{\chi}^\pm$ or $\tilde{t} \to c\tilde{\chi}^0$, where $\tilde{\chi}^\pm$ is a chargino and $\tilde{\chi}^0$ a neutralino, i.e., the DM candidate. Only the latter can lead to the topologies relevant for the DM models we consider here, since the chargino decay would lead to further charged particles in the final state. Thus, the $c\bar{c} + \not{E}_T$ topology still corresponds physically to a $b\bar{b} + \not{E}_T$ final state.

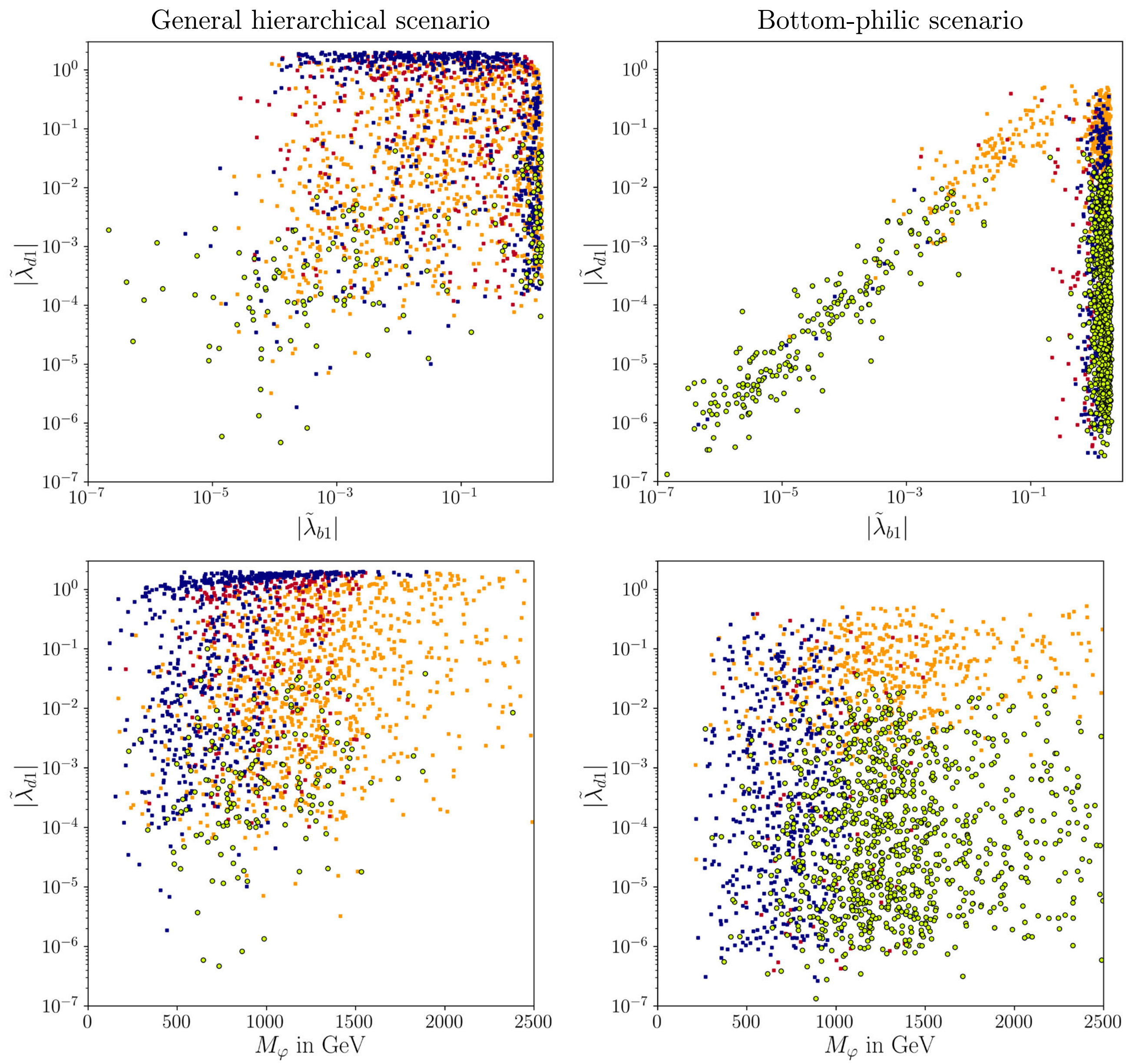

Fig. 9 Comparison of the constraints in the general hierarchical scenario (left) and the bottom-philic scenario (right). The upper panels show the $|\tilde{\lambda}_{b1}|$-$|\tilde{\lambda}_{d1}|$ plane and the lower panels show the M_φ-$|\tilde{\lambda}_{d1}|$ plane. The color coding for the different constraints is the same as in Fig. 8

These searches exclude mostly large couplings of $\tilde{\chi}_1$ to either of the quark generations, as can be seen in the upper left panel of Fig. 9. In the lower left panel, we also see that the strongest collider constraints apply to parameter points with large first-generation quark couplings leading to high-energetic di-jet + $\not{E}_T$ signals.

For the bottom-philic scenario, the most relevant searches are CMS-SUS-19-006 [106] and CMS-SUS-16-036 [108], which target the $b\bar{b} + \not{E}_T$ channel and exclude the largest number of parameter points. Other searches, such as [107, 109–112, 119], exclude only a comparatively small subset of points (where they provide the strongest constraint). The top-right panel of Fig. 9 shows that mainly parameter points with large couplings to b quarks are excluded, as expected. From the lower-right panel, we see that there is no dependence of the collider limits on the first generation coupling.

As in the leptophilic case, the points with negative values of the mass splitting parameter η and small $M_{\tilde{\chi}_1}$ are the most affected. This is because for negative η, $\tilde{\chi}_1$ has the largest coupling, leading to dominant mediator decays directly into $\tilde{\chi}_1$ and quarks. For light (third-generation) quarks, this results in high-efficiency di-jet ($b\bar{b}$) plus missing transverse energy signatures that are well covered by the relevant LHC analyses. For positive η, the mediator decays predominantly into

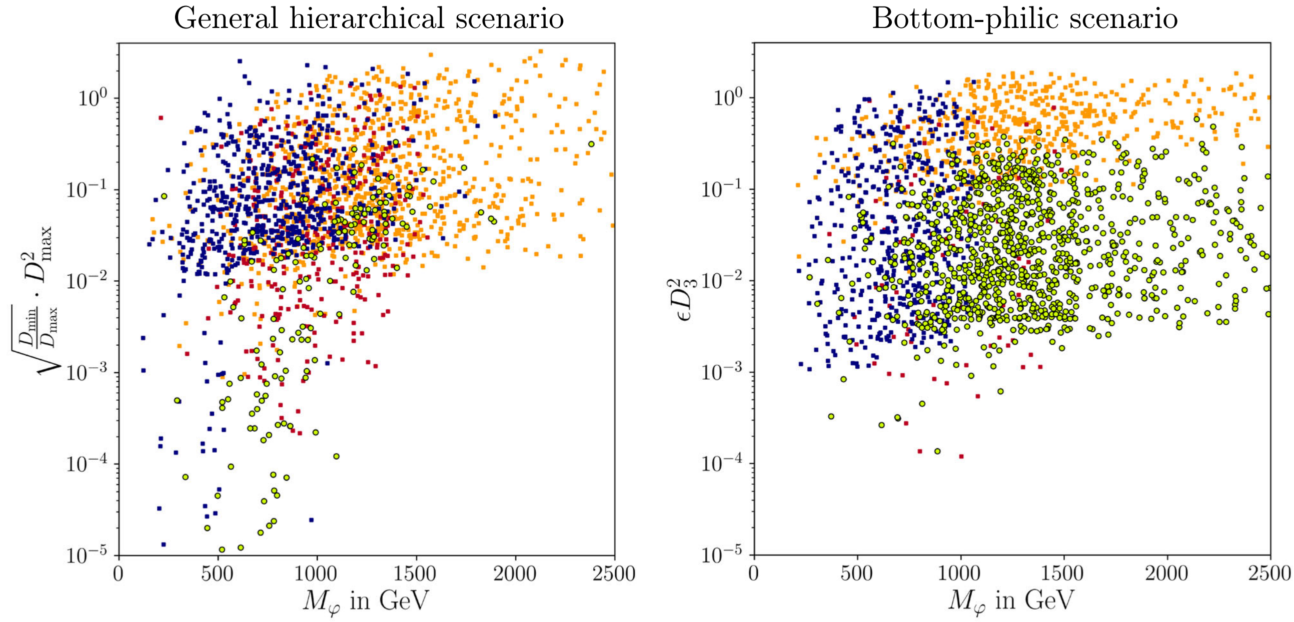

Fig. 10 Comparison of the constraints in the general hierarchical scenario (left) and the bottom-philic scenario (right). Shown are $\sqrt{D_{\min}/D_{\max}}\, D^2_{\max}$ (left) and ϵD_3^2 (right) versus the mediator mass M_φ. The two former quantities are related to each other; see the main text for details. The color coding for the different constraints is the same as in Fig. 8. Note that, to achieve a common y-axis range, the left panel is truncated at the lower end

heavier $\tilde{\chi}_i$ states, which undergo cascade decays producing multi-jet final states which are less constraining. The stronger constraints for negative η can also be observed in the bottom panels of Fig. 8.

The missing topologies identified by SMODELS in both scenarios correspond primarily to final states containing a single b quark or a b quark accompanied by a light-flavor jet. These signatures are not currently covered by the database, leaving open the possibility that dedicated searches for such final states could further extend the reach of collider constraints in this model.

Direct detection constraints: In the case of down-type quark couplings, direct detection constraints become substantially more restrictive than in the leptophilic case, because the DM particle couples directly to quarks, giving rise to tree-level SD scattering as well as to a DM-gluon interaction $\bar{\chi}\chi G^{\mu\nu}G_{\mu\nu}$ at one-loop level [120,121]. The latter constitutes the leading contribution to SI scattering for the considered case of Majorana DM and is implemented in MICROMEGAS, where it is matched onto the gluon content of the nucleon via the trace anomaly in the standard way [122]. For points yielding the measured relic abundance, current direct detection searches exclude 32.5% in the general hierarchical scan and around 5% in the bottom-philic case (excluded points shown in red). In the general hierarchical scenario, the majority of excluded points are ruled out by SD scattering limits from the LZ experiment [58]. These points feature sizable couplings to first-generation quarks, which are the most relevant for tree-level SD scattering due to the significant up- and down-quark content of the nucleons. A much smaller fraction of points is ruled out by loop-induced SI scattering constrained by LZ and XENON1T [59]. This explains the stronger bounds in the general hierarchical scan compared to the bottom-philic case, where the coupling to the down quark is generally suppressed (cf. left and right panels of Fig. 9), so that direct detection is dominated by the loop-induced SI contribution.

In the upper row of Fig. 8, it can be seen that the sensitivity of these searches extends up to the upper edge of the scanned DM mass range, with the constraints being stronger when the mediator mass is close to the DM mass, since in the zero-momentum limit relevant for direct detection the scattering amplitude is suppressed by the mediator mass.

Indirect detection constraints: In our analysis, the constraints from indirect detection experiments do not impose any relevant limits on the model, with no parameter points satisfying the relic abundance requirement being excluded in our scan. In the quark-philic scenario, the leading tree-level annihilation process $\tilde{\chi}_1\tilde{\chi}_1 \to q\bar{q}$ is p-wave suppressed and therefore inefficient in the present Universe, which limits the sensitivity of current indirect searches. As in the leptophilic case (see Sect. 4.2), the relevant present-day contribution then comes from the radiative three-body processes $\tilde{\chi}_1\tilde{\chi}_1 \to \gamma q\bar{q}$ and $\tilde{\chi}_1\tilde{\chi}_1 \to g q\bar{q}$, which are included following the prescription described in Sect. 3.1.3. Even with these contributions included, however, no parameter point in our scan is excluded by indirect detection.

Flavor constraints: Finally, we apply the flavor constraints to the remaining points that pass the relic-density, direct-detection, and collider bounds, with excluded points shown in orange. In the down-type quark coupling scenario considered, these observables are particularly powerful, excluding an additional 85.6% of the surviving parameter points in the general hierarchical scenario. In the bottom-philic scenario, the constraints are, by construction, less restrictive, with only 35.7% of the remaining parameter points being excluded. This leaves us with 165 allowed points in the general hierarchical and 973 points in the bottom-philic scenario.

The most stringent bound in both scenarios arises from the CP-violating parameter ϵ_K [123] in K^0-$\bar{K}^0$ mixing, where the NP contribution originates from the standard and crossed box diagrams involving the scalar mediator and the $\tilde{\chi}_i$ states, shown in Fig. 6. Further relevant observables are $S_{\psi K_S}$ [124], ΔM_d [125], $S_{\psi\phi}$ [124], ΔM_s [125], and ϵ'/ϵ_K [103]. Here, ΔM_d and ΔM_s denote the mass differences in the B_d and B_s systems, while $S_{\psi K_S}$ and $S_{\psi\phi}$ quantify CP-violation in the interference of B_q^0-$\bar{B}_q^0$ mixing with $b \to c\bar{c}q$ decays ($q = d, s$). The fractions of points that have passed all other constraints but show a pull above 2σ relative to the SM in these observables are listed in Table 6. They reveal that the general hierarchical scenario is far more restricted by flavor physics. The largest difference between the two scan setups appears, as expected, in ϵ_K, but the other observables also have a significantly reduced impact in the bottom-philic scan. This behavior is reflected in Figs. 8, 9 and 10. It is also visible from the top panels in Fig. 8 that the flavor constraints can probe high scales and are relevant over the entire energy range covered by our scan.

As shown in Fig. 9, these constraints exclude almost all points with a DM coupling to down quarks, $\tilde{\lambda}_{d1}$, larger than 0.1, while large couplings to b quarks are less severely constrained. The resulting bounds strongly shape the allowed flavor structure of the coupling matrix, favoring hierarchical patterns that avoid simultaneously enhancing multiple flavor-changing amplitudes, as mentioned above. For better performance, this hierarchy is incorporated directly in our two scan setups for the values of $D_{1,2,3}$, as described in Sect. 4.3.1.

The pattern of parameter points visible in the top right panel of Fig. 9 can be interpreted by inspecting the matrix $\tilde{\lambda}$ in the mass basis for the bottom-philic scenario. The couplings to the first and second generation SM quarks are $\tilde{\lambda}_{di} = \mathcal{O}(\epsilon^2)$ and $\tilde{\lambda}_{si} = \mathcal{O}(\epsilon)$, respectively, as given in Eq. (4.9). For the third family, two of the couplings are sizable, $\tilde{\lambda}_{bi} = \mathcal{O}(1)$, however, one turns out to be suppressed, $\tilde{\lambda}_{bj} = \mathcal{O}(\epsilon^2)$.[23]

[23] For details see the derivation of Eq. (B.35) in Appendix B.2.

This small coupling is associated with the first (lightest) DM generation when $\eta > 0$, whereas for $\eta < 0$ one finds $\tilde{\lambda}_{b1} = \mathcal{O}(1)$. As discussed above in connection with Fig. 8, only a few points with $\eta > 0$ satisfy the relic density constraint. Consequently, the region away from $\tilde{\lambda}_{b1} = \mathcal{O}(1)$ in the top-right panel of Fig. 9 is only sparsely populated.

To better understand the constraints from neutral meson mixing in the general hierarchical scenario, it is instructive to compare our results to approximate bounds derived from the leading box-diagram contributions (see the discussion on *Scenario I* in Appendices B.2 and B.3 for details). For example, considering small mixing angles and mass splittings, $M_{\tilde{\chi}} \sim M_\varphi$, the dominant terms that contribute to $\Delta F = 2$ processes scale as $D_i^2 D_j^2$, with i, j depending on the meson system. We obtain the approximate upper bounds

$$\begin{aligned} D_1 D_2 &< \left(0.2\text{ - }4.4\right) \times 10^{-2} \left(\frac{M_\varphi}{\text{TeV}}\right), \\ D_1 D_3 &< 5 \times 10^{-2} \left(\frac{M_\varphi}{\text{TeV}}\right), \\ D_2 D_3 &< 0.2 \left(\frac{M_\varphi}{\text{TeV}}\right), \end{aligned} \tag{4.10}$$

from K, B_d, and B_s mixing, respectively [cf. Eqs. (B.55), (B.58), and (B.59)].[24] The two limits on $D_1 D_2$ correspond to the CP-violating and CP-conserving constraints from the neutral kaon system. The system associated with the two largest D_i is subject to the strongest constraint. We can estimate the size of this contribution by considering the combination $\sqrt{D_\text{min}/D_\text{max}} \times D_\text{max}^2$, where D_min and D_max denote the smallest and largest of the D_i, respectively.[25] This quantity can be strongly constrained particularly when the kaon system receives the largest contribution, as emerges from Eq. (4.10). The corresponding result for this quantity from our parameter scan is shown in Fig. 10, where we see in the left panel that flavor constraints can be satisfied for $\sqrt{D_\text{min}/D_\text{max}} \times D_\text{max}^2 \lesssim 10^{-1}$, in accordance with the estimates in Eq. (4.10). The exact bound on $\sqrt{D_\text{min}/D_\text{max}} \times D_\text{max}^2$ depends on which meson system is affected by the largest couplings. Note that the limits in Eq. (4.10) can also be fulfilled for non-hierarchical couplings provided that their overall scale is suppressed, $D_1, D_2, D_3 \ll 1$.

Similarly, we find that in the bottom-philic scenario, the contribution to the dominant $\Delta F = 2$ process is controlled by $\epsilon\, D_3^2$. From B_s mixing, we obtain the approximate con-

[24] For $M_{\tilde{\chi}}^2 \ll M_\varphi^2$, the relevant contributions become proportional to $(\sin\theta_{ij}\,|D_j^2 - D_i^2|)^2$ leading to the bounds in the first lines of Eqs. (B.46), (B.50), (B.51).

[25] Note that we can identify $D_\text{max} \sim D_3$ and $\sqrt{D_\text{min}/D_\text{max}} \sim \epsilon$ when comparing to the bottom-philic scenario. Moreover, we can write $\sqrt{D_\text{min}/D_\text{max}} \times D_\text{max}^2 = \sqrt{D_\text{min} D_\text{max}} \times D_\text{max}$, where $\sqrt{D_\text{min} D_\text{max}}$ is the geometric mean of the second largest D_i.

Table 6 List of relevant flavor observables and their impact on our scan. The first row lists all flavor observables for which at least one parameter point in our scan has a pull above 2σ with respect to the SM expectation. The second and third rows show the percentage of points in the general hierarchical and bottom-philic scenarios, respectively, that satisfy all other (non-flavor) constraints but have a pull above 2σ with respect to the SM for the corresponding flavor observable

Observable	ϵ_K [123]	$S_{\psi K_S}$ [124]	ΔM_d [125]	$S_{\psi\phi}$ [124]	ΔM_s [125]	$\frac{\epsilon'}{\epsilon_K}$ [103]
General hier.	76%	47%	46%	39%	37%	1%
Bottom-phil.	28%	19%	18%	26%	24%	<1%

straint

$$\epsilon\, D_3^2 \lesssim 0.1 \left(\frac{M_\varphi}{\text{TeV}}\right), \tag{4.11}$$

[cf. the third lines of Eqs. (B.52) and (B.59) with $\lambda_0 \approx D_3$] which can also be observed in the right panel of Fig. 10. This highlights, again, the clearer distinction between viable and forbidden parameter space in the bottom-philic scenario.

Before concluding, we discuss two possible issues of our flavor analysis: the validity of the underlying EFT approach; and the assumptions about the CKM parameters. Since the experimental energy scale of all these observables is around the b-quark mass $m_b \sim 4\,\text{GeV}$ or below, we expect the EFT to provide a good approximation for the entire range of the DM and mediator masses listed in Table 4, cf. the discussion in Sect. 3.3.1. In addition, all parameter points with very low DM masses, where the EFT description is potentially questionable, are already excluded by collider constraints, as can be seen in the top panels of Fig. 8. Notice that the physical DM mass $M_{\tilde\chi_1}$ can also reach below the lower bound of $M_{\tilde\chi} \geq 100\,\text{GeV}$ for the Lagrangian mass parameter $M_{\tilde\chi}$ in our scan. This is due to the physical mass matrix in Eq. (4.6) receiving (possibly negative) corrections from the coupling matrix under the DMFV assumption.

Notice that for this analysis, we chose to fix the CKM elements to their SM values in SMELLI. Determining CKM elements from data in the presence of NP [126] can be problematic due to the potentially too large effects of NP in the observables used to extract the CKM elements, leading to the program crashing. Since CKM elements are extracted from B decays, this problem is particularly severe for NP models coupled to the down-type quarks. However, we have checked that the points that crash during the CKM extraction are also rejected in our analysis by other observables when fixing the CKM elements to their SM values. Furthermore, we have also verified that for the parameter points that are not problematic, the results with a CKM matrix extracted under the assumption of the SM or NP are in good agreement.

Underabundant dark matter: To assess the impact of the relic density constraint on our results, we also considered the cases in which the model accounts for only 10% or 1% of the observed DM density, again assuming a 10% theoretical uncertainty in the relic density computation. In both the general hierarchical and bottom-philic scenarios, the fraction of generated points passing the corresponding relic density constraint is significantly smaller than in the 100%-DM scenario. In the general hierarchical case, this fraction decreases from 0.8% in the 100%-DM scenario to 0.08% and 0.003% in the 10%-DM and 1%-DM scenarios, corresponding to 200 and 7 viable points, respectively. In the bottom-philic case, it decreases from 0.8% to 0.07% and 0.004%, corresponding to 183 and 10 viable points. At the same time, the preference of underabundant DM for larger coupling strengths enhances the impact of collider and flavor constraints. Most notably, direct detection becomes significantly more restrictive: in the general hierarchical scenario, the fraction of points excluded by direct detection increases from 31.7% in the 100%-DM scenario to 78.5% in the 10%-DM scenario and 100% in the 1%-DM scenario, while in the bottom-philic scenario it rises from 5.0% to 71.0% and 100%, respectively. This behavior can be understood from the fact that the relic density is often controlled by coannihilation with the mediator, whereas the direct-detection cross section scales more strongly with the DM coupling. As a result, the rescaling of the local DM density in the underabundant scenarios does not compensate the enhancement of the direct-detection rate from the larger couplings. By contrast, indirect detection still excludes no parameter points in either scenario.

5 Conclusions

In this work, we have developed and applied a comprehensive toolchain for the study of flavored DM models, combining relic density computations, direct and indirect detection bounds, collider constraints, and a global likelihood analysis of flavor observables based on one-loop matching to the SMEFT and RG evolution to the low-energy scale.

As a proof of principle, we investigated two benchmark scenarios with a Majorana DM flavor triplet coupling either to right-handed charged leptons or to right-handed down-type quarks. In both cases, we performed extensive parameter scans, taking into account the relevant theoretical and experimental constraints.

For the leptophilic scenario, we find that the relic density requirement is the most restrictive constraint, excluding roughly 97% of the parameter space points before applying other bounds. The surviving points are further shaped by strong limits from charged-lepton flavor-violating decays such as $\mu \to e\gamma$, which remove large regions of parameter space with sizable off-diagonal couplings. Collider searches for missing energy signatures still allow for a substantial viable region, as current limits only exclude a subset of points with $M_{\tilde{\chi}_1} < 200\,\text{GeV}$ and $M_\varphi < 500\,\text{GeV}$, while higher masses remain unconstrained by the LHC.

In the quark-coupling scenario, the combination of relic density, direct detection, and flavor constraints leaves only a small fraction of viable points. As flavor data places stringent limits on the parameter space, we study two particular coupling structures - a general hierarchical scenario and a bottom-philic scenario. While both scenarios behave similarly concerning the relic density constraint, limits from direct detection, collider and flavor observables differ significantly. Direct detection limits from LZ and XENON1T exclude about one third of the points in the general hierarchical scenario – predominantly points with sizable couplings to first-generation quarks, for which tree-level SD scattering is most relevant – while in the bottom-philic scenario those limits rule out only 5% of the cosmologically allowed parameter points, with the loop-induced SI contribution dominating. Collider searches using jets + $\not{E}_T$ and b-tagged final states potentially reaching mediator masses up to roughly 1.9 TeV and DM masses up to about 1.1 TeV exclude a subset of points in this region. Due to the suppressed bottom content of colliding protons, in the bottom-philic case, mediator-pair production is dominated by its strong interactions and therefore the maximal LHC reach is reduced in this case, constraining points with mediator masses up to around 1.1 TeV only. In addition, we find that higher multiplicity final states, obtained when the mediator decays to a heavier dark flavor leading to cascade decays, are suppressed. For underabundant DM, we find qualitatively similar behavior, with collider and flavor constraints becoming stronger and direct detection gaining additional relevance in the quark-coupling scenario.

The most stringent flavor constraint in both scenarios arises from ε_K, followed by $\Delta M_{d,s}$ and the CP asymmetries $S_{\psi K_S}$ and $S_{\psi\phi}$. In the general hierarchical scenario, together these remove close to 86% of the remaining points, while in the bottom-philic scenario roughly 36% of the remaining points do not pass the flavor constraints. A general feature of both scenarios is a preference for hierarchical flavor structures in the coupling matrix λ, which allow the models to evade simultaneous enhancement of several $\Delta F = 2$ processes. We have designed the general hierarchical scenario to probe a wide range of different hierarchies, while the bottom-philic scenario singles out the case where the dark sector is dominantly coupled to the bottom quark. As we have shown, the latter case leaves significantly more room for NP, due to the specific choices implemented directly into the scan setup. This finding quantitatively confirms the expectation that flavored DM models are strongly constrained by the flavor sector and motivates future model-building efforts toward naturally hierarchical couplings.

The framework we have presented is generic and flexible: UFO models for all 20 combinations of DM and mediator flavor representations are provided together with the full analysis toolchain on GitHub,[2] enabling straightforward extension of our results to other scenarios. Many of the combinations listed in the summary Table 1 remain unexplored. In particular, scenarios with left-handed mediators and with scalar DM offer a wide range of phenomenological implications – including richer decay topologies, enhanced electroweak production mechanisms, and potential links to Higgs-sector phenomenology – which we leave for future work.

Acknowledgements This research was supported by the Deutsche Forschungsgemeinschaft (DFG, German Research Foundation) under grant 396021762 - TRR 257. MB, MK, and FW are grateful to the Mainz Institute for Theoretical Physics (MITP) of the Cluster of Excellence PRISMA+ (Project ID 390831469) for its hospitality and partial support during the final stages of this work.

Data Availability Statement This manuscript has no associated data. [Authors' comment: Data sharing not applicable to this article as no datasets were generated or analysed during the current study].

Code Availability Statement This manuscript has associated code/software in a data repository. [Authors' comment: The code underlying this article is publicly available at https://github.com/lena-ra/Flavored-Dark-Matter].

Funded by SCOAP^3.

Appendix A: Naming conventions

In this appendix, we describe the naming conventions that we use for the parameters in the model files for the different flavored DM models which are published on GitHub.[2] The models are listed in the different columns and specified by the DM particle type (real or complex scalar, Dirac, or Majorana fermion) and the SM fermion to which the particles couple [i.e. right-handed up-type quarks (u), right-handed down-type quarks (d), left-handed quark doublet (q), right-handed leptons (e), and left-handed lepton doublet (l)]. The rows list

Table 7 Parameters in real scalar DM models

	Real_q	Real_u	Real_d	Real_l	Real_e
$\tilde{S}$	XS1, XS2, XS3				
$M_{\tilde{S}}$	MXS1, MXS2, MXS3				
ψ	YFq	YFu	YFd	YFl	YFe
M_ψ	MYFqu	MYFu	MYFd	MYFle	MYFe
	MYFqd			MYFlv	
f	QL	uR	dR	LL	lR
λ_{ij}	lamSqRe,	lamSuRe,	lamSdRe,	lamSlRe,	lamSeRe,
	lamSqIm	lamSuIm	lamSdIm	lamSlIm	lamSeIm
$\lambda_{\tilde{S}H}$	lamSHRe, lamSHIm				
$\lambda_{\tilde{S}\tilde{S}}$	lam2S				

Table 8 Parameters in complex scalar DM models

	Complex_q	Complex_u	Complex_d	Complex_l	Complex_e
S	XC1, XC2, XC3				
M_S	MXC1, MXC2, MXC3				
ψ	YFq	YFu	YFd	YFl	YFe
M_ψ	MYFqu	MYFu	MYFd	MYFle	MYFe
	MYFqd			MYFlv	
f	QL	uR	dR	LL	lR
λ_{ij}	lamCqRe,	lamCuRe,	lamCdRe,	lamClRe,	lamCeRe,
	lamCqIm	lamCuIm	lamCdIm	lamClIm	lamCeIm
λ_{SH}	lamCHRe, lamCHIm				
λ_{SS}	lam2C				

Table 9 Parameters in Majorana DM models

	Majorana_q	Majorana_u	Majorana_d	Majorana_l	Majorana_e
$\tilde{\chi}$	XM1, XM2, XM3				
$M_{\tilde{\chi}}$	MXM1, MXM2, MXM3				
φ	YSq	YSu	YSd	YSl	YSe
M_φ	MYSqu	MYSu	MYSd	MYSle	MYSe
	MYSqd			MYSlvR	
				MYSlvI	
f	QL	uR	dR	LL	lR
λ_{ij}	lamMqRe,	lamMuRe,	lamMdRe,	lamMlRe,	lamMeRe,
	lamMqIm	lamMuIm	lamMdIm	lamMlIm	lamMeIm
$\lambda_{\varphi H,1}$	lamYHq1	lamYHu	lamYHd	lamYHl1	lamYHe
$\lambda_{\varphi H,2}$	lamYHq2	–	–	lamYHl2	–
$\lambda_{\varphi H,3}$	–	–	–	lamYHl3	–
$\lambda_{\varphi\varphi}$	lam2Yq	lam2Yu	lam2Yd	lam2Yl	lam2Ye

Table 10 Parameters in Dirac DM models

	Dirac_q	Dirac_u	Dirac_d	Dirac_l	Dirac_e
χ	`XD1`, `XD2`, `XD3`				
M_χ	`MXD1`, `MXD2`, `MXD3`				
φ	`YSq`	`YSu`	`YSd`	`YSl`	`YSe`
M_φ	`MYSqu`	`MYSu`	`MYSd`	`MYSle`	`MYSe`
	`MYSqd`			`MYSlvR`	
				`MYSlvI`	
f	`QL`	`uR`	`dR`	`LL`	`lR`
λ_{ij}	`lamDqRe`,	`lamDuRe`,	`lamDdRe`,	`lamDlRe`,	`lamDeRe`,
	`lamDqIm`	`lamDuIm`	`lamDdIm`	`lamDlIm`	`lamDeIm`
$\lambda_{\varphi H,1}$	`lamYHq1`	`lamYHu`	`lamYHd`	`lamYHl1`	`lamYHe`
$\lambda_{\varphi H,2}$	`lamYHq2`	–	–	`lamYHl2`	–
$\lambda_{\varphi H,3}$	–	–	–	`lamYHl3`	–
$\lambda_{\varphi\varphi}$	`lam2Yq`	`lam2Yu`	`lam2Yd`	`lam2Yl`	`lam2Ye`

the parameters of the different models as introduced in Sect. 2 (Tables 7, 8, 9, 10).

Appendix B: Coupling matrix and flavor constraints

In this section we analyze the constraints and relations between the parameters of the matrix λ. We start by summarizing the dark flavor transformations in Appendix B.1. In Appendix B.2 we describe the relations between the parameters in different bases for various coupling scenarios. In Appendix B.3 we analyze the relevant experimental constraints on λ from flavor changing phenomena.

B.1 Dark flavor basis transformations

The dark-flavor-breaking terms of the Lagrangian are

$$-\frac{1}{2}\overline{\tilde{\chi}_L}\mathcal{C}\, M_{\tilde{\chi}}\,\overline{\tilde{\chi}_L}^{\intercal} - \overline{d_{Ri}}\,\lambda\,\tilde{\chi}\phi + \text{h.c.} \tag{B.1}$$

In the model presented in this work, the field $\tilde{\chi}$ transforms as a triplet under a global $O(3)$ symmetry. Under a flavor transformation we have

$$\begin{aligned} &\tilde{\chi} \to \tilde{\chi}' = R_f\,\tilde{\chi}\,, \\ M_{\tilde{\chi}} &\to M'_{\tilde{\chi}} = R_f\, M_{\tilde{\chi}}\, R_f^{\intercal}\,, \qquad \lambda \to \lambda' = \lambda\, R_f^{\intercal}\,, \end{aligned} \tag{B.2}$$

where R_f is an orthogonal matrix. Under the DMFV assumption the mass matrix emerges as

$$\tilde{M}_{\tilde{\chi}} = M_{\tilde{\chi}}\left[\mathbb{1} + \frac{\eta}{2}(\lambda^{\dagger}\lambda + \lambda^{\intercal}\lambda^{*}) + \mathcal{O}(\lambda^4)\right] \tag{B.3}$$

working to leading order in the spurion (λ) expansion. Since $\tilde{M}_{\tilde{\chi}}$ is real we can go to the mass basis using an orthogonal transformation

$$\tilde{\chi} \to \tilde{\tilde{\chi}}=W\,\tilde{\chi}\,,\; \tilde{M}_{\tilde{\chi}} \to \tilde{M}^{D}_{\tilde{\chi}}=W\,\tilde{M}_{\tilde{\chi}}\,W^{\intercal}\,,\; \lambda \to \tilde{\lambda}=\lambda\,W^{\intercal}\,, \tag{B.4}$$

where the orthogonal matrix W diagonalizes the symmetric mass matrix $\tilde{M}_{\tilde{\chi}}$, and $\tilde{M}^{D}_{\tilde{\chi}}$ is the diagonal matrix.

The λ matrix can be diagonalized by a biunitary transformation:

$$U^{\dagger}\,\lambda\,V = D\,, \tag{B.5}$$

where D is diagonal. We can choose to absorb three phases of U into V. Following [36], V can be written in terms of two orthogonal matrices (O, R) and one diagonal matrix of phases (d) [127]

$$\lambda = U D V^{\dagger} = U\,D\,O d R\,. \tag{B.6}$$

A basis with minimal number of parameters can be obtained by applying the transformation (B.2) in order to absorb the rotation R. In particular, by rotating the $\tilde{\chi}$ species with $R^{\intercal}$ one has in the new basis $\tilde{\chi}'$:

$$\lambda' = \lambda\,R^{\intercal} = U\,D O d\,, \quad \tilde{M}'_{\tilde{\chi}} = R\,\tilde{M}_{\tilde{\chi}}\,R^{\intercal}\,, \tag{B.7}$$

The transformation which brings us to the mass basis from the minimal parameterization reads

$$\begin{aligned} \tilde{\chi}' &\to \tilde{\tilde{\chi}} = W'\,\tilde{\chi}' \\ \tilde{M}'_{\tilde{\chi}} &\longrightarrow \tilde{M}^{D}_{\tilde{\chi}} = W'\,\tilde{M}'_{\tilde{\chi}}\,W'^{\intercal} = W'\,R\,\tilde{M}_{\tilde{\chi}}\,R^{\intercal}\,W'^{\intercal}\,, \\ \lambda' &\longrightarrow \tilde{\lambda} = \lambda'\,W'^{\intercal} = U\,D\,O d\,W'^{\intercal} \end{aligned} \tag{B.8}$$

with

$$W'^{\mathsf{T}} = R\, W^{\mathsf{T}}\,. \tag{B.9}$$

In particular, in a scenario where the mass matrix emerges as Eq. (B.3) we have

$$\begin{aligned} &W\left(\lambda^\dagger\lambda + \lambda^{\mathsf{T}}\lambda^*\right) W^{\mathsf{T}} = \text{diagonal}\,,\\ &W\, R^{\mathsf{T}}\left(d^* O^{\mathsf{T}} D^2 O d + d\, O^{\mathsf{T}} D^2 O d^*\right) R\, W^{\mathsf{T}} = \text{diagonal} \end{aligned} \tag{B.10}$$

or, in the basis of minimal parameterization $\tilde{\chi}'$

$$W'\left(d^* O^{\mathsf{T}} D^2 O d + d\, O^{\mathsf{T}} D^2 O d^*\right) W'^{\mathsf{T}} = \text{diagonal}\,. \tag{B.11}$$

Scenario I

For instance, we can assume that the diagonal elements are larger than the off-diagonal ones, i.e. the coupling matrix in an initial flavor basis can be written as

$$\lambda = \lambda_0 \begin{pmatrix} \hat{\lambda}_{d1} & \epsilon\hat{\lambda}_{d2} & \epsilon\hat{\lambda}_{d3} \\ \epsilon\hat{\lambda}_{s1} & \hat{\lambda}_{s2} & \epsilon\hat{\lambda}_{s3} \\ \epsilon\hat{\lambda}_{b1} & \epsilon\hat{\lambda}_{b2} & \hat{\lambda}_{b3} \end{pmatrix}, \tag{B.12}$$

where λ_0 is a real parameter of the order of the largest coupling, ϵ is a small real parameter, while $\hat{\lambda}_{\alpha i}$ are parameters which can be of order $\mathcal{O}(1)$. In this scenario we can compute the rotation matrices and the respective eigenvalues in terms of the Lagrangian parameters as an expansion in the small parameter ϵ. Assuming that the masses of the $\tilde{\chi}$ species are given by Eq. (B.3), the orthogonal matrix W [see Eq. (B.4)] at first order in ϵ is given by

$$W = \begin{pmatrix} 1 & -[W]_{21} & -[W]_{31} \\ \frac{|\hat{\lambda}_{s1}\hat{\lambda}^*_{s2}|\cos(\delta_{s1}-\delta_{s2})+|\hat{\lambda}_{d1}\hat{\lambda}^*_{d2}|\cos(\delta_{d1}-\delta_{d2})}{|\hat{\lambda}_{s2}|^2-|\hat{\lambda}_{d1}|^2}\,\epsilon & 1 & -[W]_{32} \\ \frac{|\hat{\lambda}_{b1}\hat{\lambda}^*_{b3}|\cos(\delta_{b1}-\delta_{b3})+|\hat{\lambda}_{d1}\hat{\lambda}^*_{d3}|\cos(\delta_{d1}-\delta_{d3})}{|\hat{\lambda}_{b3}|^2-|\hat{\lambda}_{u1}|^2}\,\epsilon & \frac{|\hat{\lambda}_{s2}\hat{\lambda}^*_{s3}|\cos(\delta_{s2}-\delta_{s3})+|\hat{\lambda}_{b2}\hat{\lambda}^*_{b3}|\cos(\delta_{b2}-\delta_{b3})}{|\hat{\lambda}_{b3}|^2-|\hat{\lambda}_{s2}|^2}\,\epsilon & 1 \end{pmatrix} + \mathcal{O}(\epsilon^2) \tag{B.13}$$

Notice that W' here corresponds to W in Eq. (4.7).[26]

B.2 Indicative scenarios

The parameters contained in the coupling matrix λ determine the relic density as well as the contribution of the new fields to physical processes, such as flavor changing phenomena, which provide potentially stringent constraints. Therefore, it is essential to analyze how large the couplings can be. In particular, it is important to understand the role of the different parameters and the respective experimental limits in any useful flavor basis. Hence, it is useful to clarify the relations between the parameters in different bases. In this section, we analyze these relations (and in B.3 the corresponding constraints) starting from some illustrative scenarios characterized by specific textures of the λ matrix.

The coupling matrix λ can be written in terms of U, V and D in Eq. (B.5) with the unitary matrices given by

$$U = \begin{pmatrix} 1 & \frac{\hat{\lambda}^*_{s1}\hat{\lambda}_{d1}+\hat{\lambda}^*_{s2}\hat{\lambda}_{d2}}{|\hat{\lambda}_{s2}|^2-|\hat{\lambda}_{d1}|^2}\,\epsilon & \frac{\hat{\lambda}^*_{b1}\hat{\lambda}_{d1}+\hat{\lambda}^*_{b3}\hat{\lambda}_{d3}}{|\hat{\lambda}_{b3}|^2-|\hat{\lambda}_{d1}|^2}\,\epsilon \\ -\frac{\hat{\lambda}_{s1}\hat{\lambda}^*_{d1}+\hat{\lambda}_{s2}\hat{\lambda}^*_{d2}}{|\hat{\lambda}_{s2}|^2-|\hat{\lambda}_{d1}|^2}\,\epsilon & 1 & -\frac{\hat{\lambda}_{s2}\hat{\lambda}^*_{b2}+\hat{\lambda}_{s3}\hat{\lambda}^*_{b3}}{|\hat{\lambda}_{s2}|^2-|\hat{\lambda}_{b3}|^2}\,\epsilon \\ -\frac{\hat{\lambda}_{b1}\hat{\lambda}^*_{d1}+\hat{\lambda}_{b3}\hat{\lambda}^*_{d3}}{|\hat{\lambda}_{b3}|^2-|\hat{\lambda}_{d1}|^2}\,\epsilon & \frac{\hat{\lambda}^*_{s2}\hat{\lambda}_{b2}+\hat{\lambda}^*_{s3}\hat{\lambda}_{b3}}{|\hat{\lambda}_{s2}|^2-|\hat{\lambda}_{b3}|^2}\,\epsilon & 1 \end{pmatrix} + \mathcal{O}(\epsilon^2) \tag{B.14}$$

[26] In a scenario with $d \propto \mathbf{1}$, we would have that $V^\dagger = O_R$, $\lambda = U D d\, O_R$, with O_R an orthogonal transformation. This implies that $\lambda^\dagger\lambda$ is symmetric and real and diagonalized by an orthogonal matrix. Then, the mass matrix is diagonalized by the orthogonal matrix $W = O_R$, with eigenvalues given by D. The minimal parameterization is obtained by the transformation $R = O_R = W$: $\lambda' = \lambda\, O_R^{\mathsf{T}} = U D$, $M'_{\tilde{\chi}} = O_R M_{\tilde{\chi}} O_R^{\mathsf{T}} = M_{\tilde{\chi}}^{\text{diag}}$, $W' = \mathbf{1}$.

and, with $\arg(\hat{\lambda}_{\alpha i}) = \delta_{\alpha i}$

$$V = \begin{pmatrix} e^{-i\delta_{d1}} & \frac{\hat{\lambda}^*_{s1}\hat{\lambda}_{s2}+\hat{\lambda}^*_{d1}\hat{\lambda}_{d2}}{|\hat{\lambda}_{s2}|^2-|\hat{\lambda}_{d1}|^2} e^{-i\delta_{s2}}\,\epsilon & \frac{\hat{\lambda}^*_{b1}\hat{\lambda}_{b3}+\hat{\lambda}^*_{d1}\hat{\lambda}_{d3}}{|\hat{\lambda}_{b3}|^2-|\hat{\lambda}_{d1}|^2}\, e^{-i\delta_{b3}}\epsilon \\ -\frac{\hat{\lambda}_{s1}\hat{\lambda}^*_{s2}+\hat{\lambda}_{d1}\hat{\lambda}^*_{d2}}{|\hat{\lambda}_{s2}|^2-|\hat{\lambda}_{d1}|^2} e^{-i\delta_{d1}}\,\epsilon & e^{-i\delta_{s2}} & -\frac{\hat{\lambda}^*_{s2}\hat{\lambda}_{s3}+\hat{\lambda}^*_{b2}\hat{\lambda}_{b3}}{|\hat{\lambda}_{s2}|^2-|\hat{\lambda}_{b3}|^2} e^{-i\delta_{b3}}\,\epsilon \\ -\,\frac{\hat{\lambda}_{b1}\hat{\lambda}^*_{b3}+\hat{\lambda}_{d1}\hat{\lambda}^*_{d3}}{|\hat{\lambda}_{b3}|^2-|\hat{\lambda}_{d1}|^2} e^{-i\delta_{d1}}\,\epsilon & \frac{\hat{\lambda}_{s2}\hat{\lambda}^*_{s3}+\hat{\lambda}_{b2}\hat{\lambda}^*_{b3}}{|\hat{\lambda}_{s2}|^2-|\hat{\lambda}_{b3}|^2} e^{-i\delta_{s2}}\,\epsilon & e^{-i\delta_{b3}} \end{pmatrix} + \mathcal{O}(\epsilon^2)\,, \tag{B.15}$$

where we also transferred three of the phases in U into V. Notice that these expressions are only valid in the small angles approximation, that is, the denominators cannot be small, implying for the diagonal couplings that $||\hat{\lambda}_{ii}|^2 - |\hat{\lambda}_{jj}|^2| \gg \epsilon$. As for the eigenvalues D, at first order they are given by the diagonal elements of the matrix λ in Eq. (B.12):

$$D=\lambda_0 \cdot \mathrm{diag}\Big(|\hat{\lambda}_{d1}|+\mathcal{O}(\epsilon^2)\,,\, |\hat{\lambda}_{s2}|+\mathcal{O}(\epsilon^2)\,,\, |\hat{\lambda}_{b3}|+\mathcal{O}(\epsilon^2)\Big)\,. \tag{B.16}$$

In order to obtain a minimal parameterization, the unitary matrix V can be written as in Eq. (B.6) $V^\dagger = OFR$, where O is the orthogonal matrix diagonalizing the symmetric unitary matrix $V^\dagger V^*$. At first order in ϵ we have

$$O=\begin{pmatrix} 1 & -[O]_{21} & -[O]_{31} \\ -\frac{|\hat{\lambda}_{s1}\hat{\lambda}_{s2}|\,\sin(\delta_{s1}-\delta_{s2})+|\hat{\lambda}_{d1}\hat{\lambda}_{d2}|\,\sin(\delta_{d1}-\delta_{d2})}{(|\hat{\lambda}_{s2}|^2-|\hat{\lambda}_{d1}|^2)\,\sin(\delta_{s2}-\delta_{d1})}\,\epsilon & 1 & -[O]_{32} \\ -\frac{|\hat{\lambda}_{b1}\hat{\lambda}_{b3}|\,\sin(\delta_{b1}-\delta_{b3})+|\hat{\lambda}_{d1}\hat{\lambda}_{d3}|\,\sin(\delta_{d1}-\delta_{d3})}{(|\hat{\lambda}_{b3}|^2-|\hat{\lambda}_{d1}|^2)\,\sin(\delta_{b3}-\delta_{d1})}\,\epsilon & -\frac{|\hat{\lambda}_{s2}\hat{\lambda}_{s3}|\,\sin(\delta_{s2}-\delta_{s3})+|\hat{\lambda}_{b2}\hat{\lambda}_{b3}|\,\sin(\delta_{b2}-\delta_{b3})}{(|\hat{\lambda}_{s2}|^2-|\hat{\lambda}_{b3}|^2)\,\sin(\delta_{s2}-\delta_{b3})}\,\epsilon & 1 \end{pmatrix} + \mathcal{O}(\epsilon^2)\,. \tag{B.17}$$

As regards the matrix of phases d, we have

$$d = \begin{pmatrix} e^{i\delta_{d1}}\left(1+i\,\theta_{d1}[\hat{\lambda}_{\alpha i}]\epsilon^2\right) & 0 & 0 \\ 0 & e^{i\delta_{s2}}\left(1+i\,\theta_{s2}[\hat{\lambda}_{\alpha i}]\epsilon^2\right) & 0 \\ 0 & 0 & e^{i\delta_{b3}}\left(1+i\,\theta_{b3}[\hat{\lambda}_{\alpha i}]\epsilon^2\right) \end{pmatrix}. \tag{B.18}$$

Let us remark that the expression (B.17) is only valid for small angles. This means that not only the moduli of the diagonal couplings should differ between each other $||\hat{\lambda}_{ii}|^2-|\hat{\lambda}_{jj}|^2| \gg \epsilon$, but also the differences between respective phases should be sufficiently large $|\sin(\delta_{ii}-\delta_{jj})| \gg \epsilon$. In fact, small angles in V do not imply small angles for the orthogonal matrices O and R, which instead can contain large rotations, depending on the values of the phases contained in the matrix λ. Namely, in a situation with small angles in V and large angles in O, also R, and thus $W'^{\mathsf{T}} = R\,W^{\mathsf{T}}$, would exhibit large rotations, while small phases would appear in the diagonal phase matrix

The texture (B.12) can be in conflict with experimental limits, since the magnitude of the diagonal couplings can be in general subject to constraints from flavor changing phenomena (see 1). A viable texture would then contain some hierarchy between the eigenvalues, as

$$D \approx \mathrm{diag}\left(\epsilon_1\hat{\lambda}_{d1}\,,\, \epsilon_2\hat{\lambda}_{s2}\,,\, \hat{\lambda}_{b3}\right) \tag{B.19}$$

together with small mixing angles.

Scenario II

Let us assume a different kind of scenario, in which one species of $\tilde{\chi}$ is more strongly coupled than the others, for instance with couplings of the type:

$$\lambda = \lambda_0 \begin{pmatrix} \hat{\lambda}_{d1}\epsilon^2 & \hat{\lambda}_{d2}\epsilon & \hat{\lambda}_{d3} \\ \hat{\lambda}_{s1}\epsilon^2 & \hat{\lambda}_{s2}\epsilon & \hat{\lambda}_{s3} \\ \hat{\lambda}_{b1}\epsilon^2 & \hat{\lambda}_{b2}\epsilon & \hat{\lambda}_{b3} \end{pmatrix}\,. \tag{B.20}$$

In this scenario the mixing angles from the left are generically large while the mixing angles from the right can be small:

$$U_{\alpha i} \approx \mathcal{O}(1)\,, \quad V \approx \begin{pmatrix} e^{-i\delta_{d1}} & \mathcal{O}(\epsilon) & \mathcal{O}(\epsilon^2) \\ \mathcal{O}(\epsilon) & e^{-i\delta_{s2}} & \mathcal{O}(\epsilon) \\ \mathcal{O}(\epsilon^2) & \mathcal{O}(\epsilon) & e^{-i\delta_{b3}} \end{pmatrix}\,. \tag{B.21}$$

The orthogonal matrix W also shows small mixing angles of order ϵ and ϵ^2:

$$W \approx \begin{pmatrix} 1+\mathcal{O}(\epsilon^2) & -\frac{|\hat\lambda_{s1}\hat\lambda_{s2}|\cos(\delta_{s1}-\delta_{s2})+|\hat\lambda_{b1}\hat\lambda_{b2}|\cos(\delta_{b1}-\delta_{b2})+|\hat\lambda_{d1}\hat\lambda_{d2}|\cos(\delta_{d1}-\delta_{d2})}{|\hat\lambda_{b2}|^2+|\hat\lambda_{s2}|^2+|\hat\lambda_{d2}|^2}\epsilon & \mathcal{O}(\epsilon^2) \\ -[W]_{12} & 1+\mathcal{O}(\epsilon^2) & -\frac{|\hat\lambda_{s2}\hat\lambda_{s3}|\cos(\delta_{s2}-\delta_{s3})+|\hat\lambda_{b2}\hat\lambda_{b3}|\cos(\delta_{b2}-\delta_{b3})+|\hat\lambda_{d2}\hat\lambda_{d3}|\cos(\delta_{d2}-\delta_{d3})}{|\hat\lambda_{b3}|^2+|\hat\lambda_{s3}|^2+|\hat\lambda_{d3}|^2}\epsilon \\ \mathcal{O}(\epsilon^2) & -[W]_{23} & 1+\mathcal{O}(\epsilon^2) \end{pmatrix}. \tag{B.22}$$

As for the eigenvalues we have

$$D = \lambda_0 \begin{pmatrix} \mathcal{O}(\epsilon^2) & 0 & 0 \\ 0 & \mathcal{O}(\epsilon) & 0 \\ 0 & 0 & \sqrt{|\hat\lambda_{b3}|^2+|\hat\lambda_{s3}|^2+|\hat\lambda_{d3}|^2}+\mathcal{O}(\epsilon^2) \end{pmatrix}. \tag{B.23}$$

Let us note that in a model with the mass matrix given by Eq. (B.3) (dark minimal flavor violation) the choice of the third species as the more coupled is only for illustration, in fact any column of the λ matrix could be the largest since the order of the eigenvalues can be reshuffled and large left rotations are equivalent to a renaming of the DM fields.

Neutral mesons systems can impose stringent constraints on the magnitude of the products of the strongest couplings (e.g. $\lambda_{d3}\lambda_{s3}$, $\lambda_{d3}\lambda_{b3}$, $\lambda_{s3}\lambda_{b3}$ in the example, respectively from neutral kaons and B mesons). Then a more realistic texture for the couplings would show additional hierarchy between the three larger couplings.

Scenario III

We can envisage a scenario where the DM couplings to the SM fermions manifest some hierarchy depending on the SM family. Namely, the DM species can be more strongly coupled to one SM family than the others, for example, with the third family:

$$\lambda = \lambda_0 \begin{pmatrix} \hat\lambda_{d1}\epsilon^2 & \hat\lambda_{d2}\epsilon^2 & \hat\lambda_{d3}\epsilon^2 \\ \hat\lambda_{s1}\epsilon & \hat\lambda_{s2}\epsilon & \hat\lambda_{s3}\epsilon \\ \hat\lambda_{b1} & \hat\lambda_{b2} & \hat\lambda_{b3} \end{pmatrix}. \tag{B.24}$$

This corresponds to the *bottom-philic* scenario considered in Sec. 4.3. In this case, since the matrix $\lambda^\dagger\lambda$ contains elements of the same order of magnitude, the mixing angles from the right are generically large [as well as the angles of the orthogonal matrix which diagonalizes the $\tilde\chi$ mass matrix (B.3)]

$$V_{ij} \approx \mathcal{O}(1)\,, \quad W_{ij} \approx \mathcal{O}(1) \tag{B.25}$$

while the mixing angles from the left show hierarchy. Specifically, we can find the mixing from the left by diagonalizing the matrix $\lambda\lambda^\dagger$:

$$U = \begin{pmatrix} 1 & \frac{\hat\lambda^*_{s1}\hat\lambda_{d1}+\hat\lambda^*_{s2}\hat\lambda_{d2}+\hat\lambda^*_{s3}\hat\lambda_{d3}}{|\hat\lambda_{s1}|^2+|\hat\lambda_{s2}|^2+|\hat\lambda_{s3}|^2}\epsilon & \mathcal{O}(\epsilon^2) \\ -\frac{\hat\lambda_{s1}\hat\lambda^*_{d1}+\hat\lambda_{s2}\hat\lambda^*_{d2}+\hat\lambda_{s3}\hat\lambda^*_{d3}}{|\hat\lambda_{s1}|^2+|\hat\lambda_{s2}|^2+|\hat\lambda_{s3}|^2}\epsilon & 1 & \frac{\hat\lambda_{s3}\hat\lambda^*_{b3}+\hat\lambda_{s2}\hat\lambda^*_{b2}+\hat\lambda_{s1}\hat\lambda^*_{b1}}{|\hat\lambda_{b1}|^2+|\hat\lambda_{b2}|^2+|\hat\lambda_{b3}|^2}\epsilon \\ \mathcal{O}(\epsilon^2) & -\frac{\hat\lambda^*_{s3}\hat\lambda_{b3}+\hat\lambda^*_{s2}\hat\lambda_{b2}+\hat\lambda^*_{s1}\hat\lambda_{b1}}{|\hat\lambda_{b1}|^2+|\hat\lambda_{b2}|^2+|\hat\lambda_{b3}|^2}\epsilon & 1 \end{pmatrix} + \mathcal{O}(\epsilon^2)\,. \tag{B.26}$$

For the eigenvalues we get

$$D^2 = \lambda_0^2 \begin{pmatrix} \mathcal{O}(\epsilon^4) & 0 & 0 \\ 0 & \left(|\hat{\lambda}_{s1}|^2 + |\hat{\lambda}_{s2}|^2 + |\hat{\lambda}_{s3}|^2 - \frac{\left|\hat{\lambda}_{s1}^*\hat{\lambda}_{b1}+\hat{\lambda}_{s2}^*\hat{\lambda}_{b2}+\hat{\lambda}_{s3}^*\hat{\lambda}_{b3}\right|^2}{|\hat{\lambda}_{b1}|^2+|\hat{\lambda}_{b2}|^2+|\hat{\lambda}_{b3}|^2}\right)\epsilon^2 + \mathcal{O}(\epsilon^4) & 0 \\ 0 & 0 & |\hat{\lambda}_{b1}|^2 + |\hat{\lambda}_{b2}|^2 + |\hat{\lambda}_{b3}|^2 + \mathcal{O}(\epsilon^2) \end{pmatrix}. \tag{B.27}$$

Let us notice that one element of the matrix λ can always be made zero by an orthogonal rotation of the $\tilde{\chi}$ fields. In particular, in the limit $\epsilon \to 0$, the matrix λ has the form

$$\lambda_{\epsilon=0} = \begin{pmatrix} 0 & 0 & 0 \\ 0 & 0 & 0 \\ \lambda_{b1} & \lambda_{b2} & \lambda_{b3} \end{pmatrix}$$
$$\to \quad \tilde{\lambda}_{\epsilon=0} = \lambda_{\epsilon=0} W_0^{\mathsf{T}} = \begin{pmatrix} 0 & 0 & 0 \\ 0 & 0 & 0 \\ 0 & \tilde{\lambda}_{0b2} & \tilde{\lambda}_{0b3} \end{pmatrix}, \tag{B.28}$$

i.e.,. we can perform an orthogonal rotation $\lambda \to \lambda W^{\mathsf{T}}$ to set e.g. $[\lambda W^{\mathsf{T}}]_{11} = 0$, which implies the conditions:

$$\sum_i \lambda_{bi} W_{0\,1i} = 0\,. \tag{B.29}$$

This has to be the same transformation which diagonalizes $\lambda^\dagger\lambda$ and its real part $(\lambda^\dagger\lambda + \lambda^{\mathsf{T}}\lambda^*)/2$. In fact, in the limit $\epsilon \to 0$ the matrix $\lambda^\dagger\lambda$ has two zero eigenvalues, while its real part has one zero eigenvalue, e.g., the first one. Namely, the diagonalization of $(\lambda^\dagger\lambda + \lambda^{\mathsf{T}}\lambda^*)/2$ gives

$$\left[W\,\mathrm{Re}(\lambda^\dagger\lambda)\,W^{\mathsf{T}}\right]_{\ell n} = \mathrm{Re}\Big(\sum_{i,j} \lambda_i^* W_{\ell i} \lambda_j W_{nj}\Big) = 0\,, \qquad \ell \neq n \tag{B.30}$$

and for the eigenvalues we have

$$\Big|\sum_i \lambda_i W_{0\,1i}\Big|^2 = 0\,, \quad \Big|\sum_i \lambda_i W_{0\,3i}\Big|^2 \sim \Big|\sum_i \lambda_i W_{0\,2i}\Big|^2 \sim \mathcal{O}(\lambda_0^2)\,. \tag{B.31}$$

For $\epsilon \neq 0$, we have

$$\left[\lambda^\dagger\lambda\right]_{ij} = \lambda_{bi}^*\lambda_{bj} + \mathcal{O}(\epsilon^2)\,. \tag{B.32}$$

The trace and the determinant of $(\lambda^\dagger\lambda + \lambda^{\mathsf{T}}\lambda^*)$ are respectively of order λ_0^2 and $\epsilon^2\lambda_0^6$, with e.g. the first eigenvalue which is zero in the limit $\epsilon \to 0$. Then, the diagonalization of the mass matrix reads

$$W\,\mathrm{Re}(\lambda^\dagger\lambda)\,W^{\mathsf{T}} = \mathrm{Re}\left[W_1 W_0\,(\lambda^\dagger\lambda)\,W_0^{\mathsf{T}} W_1^{\mathsf{T}}\right]$$
$$= W_1 \begin{pmatrix} \mathcal{O}(\epsilon^2) & \mathcal{O}(\epsilon^2) & \mathcal{O}(\epsilon^2) \\ \mathcal{O}(\epsilon^2) & \mathcal{O}(\lambda_0^2) & \mathcal{O}(\epsilon^2) \\ \mathcal{O}(\epsilon^2) & \mathcal{O}(\epsilon^2) & \mathcal{O}(\lambda_0^2) \end{pmatrix} W_1^{\mathsf{T}}\,. \tag{B.33}$$

Hence, the transformation leading to the mass basis is

$$W^{\mathsf{T}} = W_0^{\mathsf{T}} W_1^{\mathsf{T}} \approx W_0^{\mathsf{T}}$$
$$\begin{pmatrix} 1 & \mathcal{O}(\epsilon^2) & \mathcal{O}(\epsilon^2) \\ \mathcal{O}(\epsilon^2) & 1 & \mathcal{O}(\epsilon^2) \\ \mathcal{O}(\epsilon^2) & \mathcal{O}(\epsilon^2) & 1 \end{pmatrix}. \tag{B.34}$$

Thus, using (B.29) and (B.34), in the mass basis we have

$$\tilde{\lambda} = \lambda W^{\mathsf{T}}$$
$$= \begin{pmatrix} \mathcal{O}(\epsilon^2) & \mathcal{O}(\epsilon^2) & \mathcal{O}(\epsilon^2) \\ \mathcal{O}(\epsilon) & \mathcal{O}(\epsilon) & \mathcal{O}(\epsilon) \\ \mathcal{O}(\epsilon^2) & \tilde{\lambda}_{b2} & \tilde{\lambda}_{b3} \end{pmatrix}. \tag{B.35}$$

B.3 Neutral mesons

In the SM, the short-distance contribution to the transition $K^0(d\bar{s}) \leftrightarrow \bar{K}^0(\bar{d}s)$ arises from weak box diagrams. The weak short-distance contribution to the mass splitting $\Delta m_K = m_{K_L} - m_{K_S}$ and the CP-violating effects are described by the off-diagonal term M_{12} of the mass matrix of neutral kaons $M_{12} = -\langle K^0|\mathcal{L}_{\Delta S=2}|\bar{K}^0\rangle/(2m_K)$, which in the SM is

$$M_{12}^{\mathrm{SM}} = -\frac{G_F^2 m_W^2 f_K^2 m_K B_K}{12\pi^2}$$
$$\times \left(\lambda_c^{*2}\,S(x_c) + \lambda_t^{*2}\,S(x_t) + 2\,\lambda_c^*\lambda_t^*\,S(x_c, x_t)\right), \tag{B.36}$$

where $\lambda_a = V_{as}^* V_{ad}$, $x_a = m_a^2/m_W^2$, f_K is the kaon decay constant, which can be determined in lattice QCD to be $f_K = 155.7(0.7)$ MeV [128], $m_K = 497.611 \pm 0.013$ MeV is the neutral kaon mass, the factor B_K is the correction to the vacuum insertion approximation which is calculated in lattice QCD, $B_K = 0.7533(91)$ [129], and $S(x_i)$ are the Inami–Lim functions [130] (corrected by short-distance QCD effects [131]).

The modulus and the imaginary part of the mixing mass M_{12}^K describe short-distance contributions in the mass splitting and CP-violation in $\bar{K}^0 \leftrightarrow K^0$ transitions [131]

$$\Delta m_K \approx 2|M_{12}^K| + \Delta m_{K,\mathrm{LD}} ,$$
$$|\epsilon_K| \approx \frac{|\mathrm{Im} M_{12}^K|}{\sqrt{2}\Delta m_K} , \tag{B.37}$$

(in the standard parameterization of V_{CKM}, i.e. λ_u real). $\Delta m_{K,\mathrm{LD}}$ represents the long-distance contributions which are difficult to evaluate [132,133]. However the short distance contribution gives the dominant contribution to the experimental determination $\Delta m_{K,\mathrm{exp}} = (3.484 \pm 0.006) \times 10^{-15}$ GeV [134]. From experimental data one also obtains $|\epsilon_K|_{\mathrm{exp}} = (2.228 \pm 0.011) \times 10^{-3}$ [134].

The dominant short-distance contribution to the B_d^0-$\bar{B}_d^0$ mixing in the SM is given by

$$\Delta M_{B_d,\mathrm{SM}} = 2|M_{12,\mathrm{SM}}^B|$$
$$= m_{B_d} f_{B_d}^2 B_{B_d} \frac{G_F^2 m_W^2}{6\pi^2} |(V_{tb} V_{td}^*)^2| S(x_t) , \tag{B.38}$$

where $M_{12,\mathrm{SM}}^{B_d} = -\langle B_d^0 | \mathcal{L}_{\Delta B_d=2} | \bar{B}_d^0 \rangle / (2 m_{B_d^0})$ and B_{B_d} is the correction factor to the vacuum-insertion approximation. In neutral B-mesons system long distance contributions are estimated to be small. The analogous expression can be obtained for B_s^0-$\bar{B}_s^0$ system by substituting $d \to s$. Lattice QCD calculations yield $f_{B_d}\sqrt{B_{B_d}} = 210.6(5.5)$ MeV and $f_{B_s}\sqrt{B_{B_s}} = 256.1(5.7)$ MeV [128]. The experimental results are $\Delta M_{B_d,\mathrm{exp}} = (3.334 \pm 0.013) \times 10^{-13}$ GeV, $\Delta M_{B_s,\mathrm{exp}} = (1.1693 \pm 0.0004) \times 10^{-11}$ GeV [134].

In the illustrated model with Majorana DM species and the extra scalar field coupled to the SM down quarks, new contributions to neutral meson mixing are generated through box diagrams (see Fig. 6). For instance, the additional contribution to the neutral kaon system reads (see Ref. [36]):

$$M_{12,\mathrm{NP}}^K \approx \frac{1}{3} m_K f_K^2 \frac{1}{128\pi^2 M_\varphi^2}$$
$$\times \left(\sum_{ij} \tilde{\lambda}_{di}^* \tilde{\lambda}_{si} \tilde{\lambda}_{dj}^* \tilde{\lambda}_{sj} F(x_i, x_j) - \sum_{ij} (\tilde{\lambda}_{si} \tilde{\lambda}_{dj}^*)^2 \, 2\, G(x_i, x_j) \right) , \tag{B.39}$$

where $x_i = M_{\tilde{\chi}_i}^2 / M_\varphi^2$,

$$\tilde{\lambda} = \lambda' W'^T = \lambda W^\intercal = U D O d W'^\intercal \tag{B.40}$$

and $F(x_i, x_j)$ and $G(x_i, x_j)$ are functions with values $1 \geq F(x_i, x_j) \geq 0$ and $0 \leq 2G(x_i, x_j) \leq \frac{1}{3}$. For $x_{i,j} \leq 1$, $F(x_i, x_j)$ is a decreasing function of x_i, x_j assuming values between 1 and 1/3 while $2G(x_i, x_j)$ is an increasing function of x_i, x_j assuming values between 0 and 1/3. In particular, for $x_{i,j} \to 0$, $F(x_i, x_j) \to 1$ and $G(x_i, x_j) \to 0$, for $x_j \to 0$ and $x_i \to 1$, $F(x_i, x_j) \to 1/2$ and $G(x_i, x_j) \to 0$, while for $x_j, x_i \to 1$, $F(x_i, x_j)$, $2G(x_i, x_j) \to 1/3$. For $x_{i(j)} \to \infty$, $F(x_i, x_j) \to 0$ and $G(x_i, x_j) \to 0$.

Approximate bounds on the new physics contribution can be estimated by comparison with the SM contribution, as $|M_{12,\mathrm{NP}}^K| < |M_{12,\mathrm{SM}}^K| \, \Delta_K$, $|\mathrm{Im} M_{12,NP}^K| < |\mathrm{Im} M_{12,\mathrm{SM}}^K| \, \Delta_{\epsilon_K}$, e.g. by setting $\Delta_K = 1$ and, approximately using the results in Ref. [135] at 95% CL, $\Delta_{\epsilon_K} = 0.3$. By comparing the effective Lagrangians we obtain

$$\left| \sum_{ij} \tilde{\lambda}_{di}^* \tilde{\lambda}_{si} \tilde{\lambda}_{dj}^* \tilde{\lambda}_{sj} F(x_i, x_j) - \sum_{ij} (\tilde{\lambda}_{si} \tilde{\lambda}_{dj}^*)^2 \, 2\, G(x_i, x_j) \right|$$
$$< 0.6 \times 10^{-5} \left(\frac{M_\varphi}{10^2 \text{ GeV}} \right)^2 ,$$
$$\left| \mathrm{Im} \left[\sum_{ij} \tilde{\lambda}_{di}^* \tilde{\lambda}_{si} \tilde{\lambda}_{dj}^* \tilde{\lambda}_{sj} F(x_i, x_j) - \sum_{ij} (\tilde{\lambda}_{si} \tilde{\lambda}_{dj}^*)^2 \, 2\, G(x_i, x_j) \right] \right|$$
$$< 1.4 \times 10^{-8} \left(\frac{M_\varphi}{10^2 \text{ GeV}} \right)^2 . \tag{B.41}$$

Analogous expressions can be written for the new contributions to neutral B-mesons systems:

$$M_{12,\mathrm{NP}}^{B_d} \approx \frac{1}{3} m_{B_d} f_{B_d}^2 \frac{1}{128\pi^2 M_\varphi^2}$$
$$\times \left(\sum_{ij} \tilde{\lambda}_{di}^* \tilde{\lambda}_{bi} \tilde{\lambda}_{dj}^* \tilde{\lambda}_{bj} F(x_i, x_j) - 2 \sum_{ij} (\tilde{\lambda}_{bi} \tilde{\lambda}_{dj}^*)^2 G(x_i, x_j) \right) \tag{B.42}$$

and similarly for B_s with the substitution $d \to s$. The results obtained in Ref. [135] at 95% CL approximately give a constraint $\Delta M_{B_{d(s)}}^{\mathrm{new}} < \Delta M_{B_{d(s)}}^{\mathrm{SM}} \Delta_{B_{d(s)}}$ with $\Delta_{B_d} = 0.3$, $\Delta_{B_s} = 0.2$. Then, the combination of couplings and Inami–Lim functions in the different scenarios are limited respectively as

$$\left| \sum_{ij} \tilde{\lambda}_{di}^* \tilde{\lambda}_{bi} \tilde{\lambda}_{dj}^* \tilde{\lambda}_{bj} F(x_i, x_j) - 2 \sum_{ij} (\tilde{\lambda}_{bi} \tilde{\lambda}_{dj}^*)^2 G(x_i, x_j) \right|$$
$$< 0.8 \times 10^{-5} \left(\frac{M_\varphi}{10^2 \text{ GeV}} \right)^2 , \tag{B.43}$$
$$\left| \sum_{ij} \tilde{\lambda}_{si}^* \tilde{\lambda}_{bi} \tilde{\lambda}_{sj}^* \tilde{\lambda}_{bj} F(x_i, x_j) - 2 \sum_{ij} (\tilde{\lambda}_{bi} \tilde{\lambda}_{sj}^*)^2 G(x_i, x_j) \right|$$
$$< 1.2 \times 10^{-4} \left(\frac{M_\varphi}{10^2 \text{ GeV}} \right)^2 . \tag{B.44}$$

In the following, we study these constraints in different scenarios. Namely, we analyze the constraints in different regimes of mass differences $M_\varphi^2 - M_{\tilde{\chi}_i}^2$, considering the scenarios generated by the three textures in Eqs. (B.12), (B.20), and (B.24).

1. For instance, with $x_i \to 0$ for all species we would have the extra contribution to kaon mixing

$$M^K_{12,\mathrm{NP}} \approx \frac{1}{3} m_K f_K^2 \frac{1}{128\pi^2 M_\varphi^2}\left[(\tilde{\lambda}\tilde{\lambda}^\dagger)_{sd}\right]^2 = \frac{1}{3} m_K f_K^2 \frac{1}{128\pi^2 M_\varphi^2}\left[(\lambda\lambda^\dagger)_{sd}\right]^2 = \frac{1}{3} m_K f_K^2 \frac{1}{128\pi^2 M_\varphi^2}\Big(\sum_i U_{si} D_i^2 U^*_{di}\Big)^2 . \quad \text{(B.45)}$$

The relevance of the bounds (B.41) also depend on the texture of the coupling matrix. For instance, for the three textures I, II, III in Eqs. (B.12), (B.20), and (B.24) we would have respectively

$$\left|(\lambda\lambda^\dagger)_{sd}\right| = \left|(U D^2 U^\dagger)_{sd}\right| \approx \begin{cases} \text{I:} \;\; \epsilon\,|\hat\lambda^*_{d1}\hat\lambda_{s1} + \hat\lambda^*_{d2}\hat\lambda_{s2}|\lambda_0^2 \approx |s^\theta_{12}|\,|D_2^2 - D_1^2| & \\ \text{II:} \;\; |\lambda_{sj(=3)}\lambda^*_{dj(=3)}| \approx |U^*_{d3}U_{s3}|D_3^2 & < 2.5\times 10^{-3}\left(\frac{M_\varphi}{10^2\,\mathrm{GeV}}\right) \\ \text{III:} \;\; \epsilon^{n(=3)}\,|\sum_i \hat\lambda^*_{di}\hat\lambda_{si}|\lambda_0^2 \approx |s^\theta_{13}s^\theta_{23}\,e^{i(\delta_{13}-\delta_{23})}\,D_3^2 + s^\theta_{12}\,e^{i\delta_{12}}\,D_2^2| & \end{cases} \quad \text{(B.46)}$$

[where $s^\theta_{12} = \sin(\theta_{ij})$ as defined in (4.2)]. The index j indicates the $\tilde{\chi}$ species with larger couplings [$j = 3$ in Eq. (B.20)] and n depends on which SM species is mostly coupled to DM [$n = 3$ in Eq. (B.20)]. Note that $s^\theta_{12} \sim \epsilon$ in the first case, $|U^*_{Ld3}U_{Ls3}| \sim 1$ generically in the second case, while for the third λ texture we have $s^\theta_{12}, s^\theta_{23} \sim \epsilon$, $s^\theta_{13} \sim \epsilon^2$ with $D_2 \sim \epsilon\,\lambda_0$. From the bound on CP-violation the respective imaginary parts should be $< 2\times 10^{-4}\, m_\phi/10^2$ GeV, e.g. for the first scenario

$$\left|\mathrm{Im}\left[(\lambda\lambda^\dagger)^2_{sd}\right]\right|^{1/2} \approx |s^\theta_{12}\,(D_1^2 - D_2^2)| \, \left|\sin(2\delta_{12})\right|^{1/2} < 1.2\times 10^{-4}\left(\frac{M_\varphi}{10^2\,\mathrm{GeV}}\right). \quad \text{(B.47)}$$

We can infer a limit on ϵ from the first and third scenario, which taking into account the CP-violating effect (assuming generic phases) reads

$$\text{I:} \;\; \epsilon\,\lambda_0^2 \lesssim (0.12\text{ - }2.5)\times 10^{-3}\left(\frac{M_\varphi}{10^2\,\mathrm{GeV}}\right), \qquad \text{III:} \;\; \epsilon\,\lambda_0^{2/3} \lesssim (0.5\text{ - }1.4)\times 10^{-1}\left(\frac{M_\varphi}{10^2\,\mathrm{GeV}}\right)^{1/3}, \quad \text{(B.48)}$$

where λ_0 is of the order of the largest coupling. In the second scenario instead the contribution is unsuppressed and we get a limit on the coupling

$$\text{II:} \;\; \lambda_0 \lesssim (1.1\text{ - }5)\times 10^{-2}\left(\frac{M_\varphi}{10^2\,\mathrm{GeV}}\right)^{1/2}. \quad \text{(B.49)}$$

Analogously from B and B_s-mesons systems we get

$$\Big|\sum_i \lambda^*_{di}\lambda_{bi}\Big| = \Big|\sum_i U_{bi} D_i^2 U^*_{di}\Big| \approx \begin{cases} \text{I:} \;\; \epsilon\,|\hat\lambda^*_{d1}\hat\lambda_{b1} + \hat\lambda^*_{d3}\hat\lambda_{b3}|\lambda_0^2 \approx |s^\theta_{13}|\,|D_3^2 - D_1^2| & \\ \text{II:} \;\; |\lambda_{bj(=3)}\lambda^*_{dj(=3)}| & < 2.8\times 10^{-3}\,\frac{M_\varphi}{10^2\,\mathrm{GeV}} \\ \text{III:} \;\; \epsilon^{n(=2)}\,|\sum_i \hat\lambda^*_{di}\hat\lambda_{bi}|\lambda_0^2 \approx |s^\theta_{13}|\,D_3^2 & \end{cases} \quad \text{(B.50)}$$

and

$$\Big|\sum_i \lambda^*_{si}\lambda_{bi}\Big| = \Big|\sum_i U_{bi} D_i^2 U^*_{si}\Big| \approx \begin{cases} \text{I:} \;\; \epsilon\,|\hat\lambda^*_{s2}\hat\lambda_{b2} + \hat\lambda^*_{s3}\hat\lambda_{b3}|\lambda_0^2 \approx |s^\theta_{23}|\,|D_3^2 - D_2^2| & \\ \text{II:} \;\; |\lambda_{bj(=3)}\lambda^*_{sj(=3)}| & < 1.1\times 10^{-2}\,\frac{M_\varphi}{10^2\,\mathrm{GeV}} \\ \text{III:} \;\; \epsilon^{n(=1)}\,|\sum_i \hat\lambda^*_{si}\hat\lambda_{bi}|\lambda_0^2 \approx |s^\theta_{23}|\,D_3^2 & \end{cases} \quad \text{(B.51)}$$

providing respectively the approximate bounds in the three scenarios

$$\begin{aligned} \text{I:} \;\; (B) \;\; & \epsilon\,\lambda_0^2 \lesssim 3\times 10^{-3}\left(\frac{M_\varphi}{10^2\,\mathrm{GeV}}\right), \\ (B_s) \;\; & \epsilon\,\lambda_0^2 \lesssim 10^{-2}\left(\frac{M_\varphi}{10^2\,\mathrm{GeV}}\right), \\ \text{II:} \;\; (B) \;\; & \lambda_0 \lesssim 5.3\times 10^{-2}\left(\frac{M_\varphi}{10^2\,\mathrm{GeV}}\right)^{1/2}, \\ (B_s) \;\; & \lambda_0 \lesssim 0.1\left(\frac{M_\varphi}{10^2\,\mathrm{GeV}}\right)^{1/2}, \\ \text{III:} \;\; (B) \;\; & \epsilon\,\lambda_0 \lesssim 5.3\times 10^{-2}\left(\frac{M_\varphi}{10^2\,\mathrm{GeV}}\right)^{1/2}, \\ (B_s) \;\; & \epsilon\,\lambda_0^2 \lesssim 10^{-2}\left(\frac{M_\varphi}{10^2\,\mathrm{GeV}}\right). \end{aligned} \quad \text{(B.52)}$$

Let us notice that from Eqs. (B.47) and (B.49) we have that for $\lambda_0 \sim D_3 \lesssim 0.01$ the hierarchy becomes irrelevant in suppressing the flavor constraints. We can also obtain a combined estimate from the three systems considering the limits together

$$\begin{aligned} &\text{I:} \;\; \epsilon^{1/2}\left(|D_2^2 - D_1^2||D_3^2 - D_1^2||D_3^2 - D_2^2|\right)^{1/6} \sim \epsilon^{1/2}\,\lambda_0 \\ &\text{II:} \;\; D_3 \approx \lambda_0 \\ &\text{III:} \;\; \epsilon\,D_3 \approx \epsilon\,\lambda_0 \\ &\quad \lesssim (0.04\text{ - }0.07)\left(\frac{M_\varphi}{10^2\,\mathrm{GeV}}\right)^{1/2}. \end{aligned} \quad \text{(B.53)}$$

In this setting with $x_i \to 0$, the second scenario with one dark species mainly coupled to standard particles would contribute without suppression to the neutral mesons mixing.

Some larger coupling can be allowed in presence of additional hierarchy between the three largest couplings.[27]

2. In the limit in which $x_i \to 1$ for all species, $(M_\varphi^2 - M_{\tilde\chi}^2)/M_\varphi^2 \ll 1$, (and the mass difference between the $\tilde\chi$ species can be neglected) we have the extra contribution to neutral kaon mixing

$$\begin{aligned} M_{12,\mathrm{NP}}^K &\approx \frac{1}{3} m_K f_K^2 \frac{1}{128\pi^2 M_\varphi^2} \frac{1}{3}\left(\left[(\tilde\lambda\tilde\lambda^\dagger)_{sd}\right]^2 - (\tilde\lambda\tilde\lambda^\intercal)_{ss}(\tilde\lambda^*\tilde\lambda^\dagger)_{dd}\right) \\ &= \frac{1}{3} m_K f_K^2 \frac{1}{128\pi^2 M_\varphi^2} \frac{1}{3}\left(\left[(\lambda\lambda^\dagger)_{sd}\right]^2 - (\lambda\lambda^\intercal)_{ss}(\lambda^*\lambda^\dagger)_{dd}\right) \\ &= \frac{1}{3} m_K f_K^2 \frac{1}{128\pi^2 M_\varphi^2} \frac{1}{3}\left((UD^2U^\dagger)_{sd}^2 - (UDV^\dagger V^* DU_L^\intercal)_{ss}(U^*DV^\intercal VDU^\dagger)_{dd}\right) \\ &= \frac{1}{3} m_K f_K^2 \frac{1}{128\pi^2 M_\varphi^2} \frac{1}{3}\left((UD^2U^\dagger)_{sd}^2 - (UDOd^2O^\intercal DU^\intercal)_{ss}(U^*DOd^{*2}O^\intercal DU^\dagger)_{dd}\right) . \end{aligned} \tag{B.54}$$

The combinations of couplings which are relevant depend on the texture of the λ matrix. For example, for the three textures in Eqs. (B.12), (B.20), and (B.24) we have respectively

$$\left|\left[(\lambda\lambda^\dagger)_{sd}\right]^2 - (\lambda\lambda^\intercal)_{ss}(\lambda^*\lambda^\dagger)_{dd}\right| \approx \begin{cases} \text{I:} \quad |(\hat\lambda_{s2}\hat\lambda_{d1}^*)^2|\lambda_0^4 \approx D_2^2 D_1^2 \\ \text{II:} \quad \epsilon^2 |(\hat\lambda_{s3}\hat\lambda_{d2}^* - \hat\lambda_{s2}\hat\lambda_{d3}^*)^2|\lambda_0^4 < 2\times 10^{-5}\left(\frac{M_\varphi}{10^2\,\mathrm{GeV}}\right)^2 . \\ \text{III:} \quad \sim \epsilon^6 \lambda_0^4 \end{cases} \tag{B.55}$$

The limit from the CP-violating parameter ϵ_K which apply to the imaginary part of the contributions reads

$$\left|\mathrm{Im}\left[\left[(\lambda\lambda^\dagger)_{sd}\right]^2 - (\lambda\lambda^\intercal)_{ss}(\lambda^*\lambda^\dagger)_{dd}\right]\right| < 4\times 10^{-8}\left(\frac{M_\varphi}{10^2\,\mathrm{GeV}}\right)^2 , \tag{B.56}$$

e.g., in the first case we get

$$\begin{aligned} &|\hat\lambda_{s2}\hat\lambda_{d1}|^2\lambda_0^4 |\sin[2(\delta_{s2}-\delta_{d1})]| \approx D_1^2 D_2^2 |\sin[2(\gamma_2-\gamma_1)]| \\ &\quad < 4\times 10^{-8}\left(\frac{M_\varphi}{10^2\,\mathrm{GeV}}\right)^2 . \end{aligned} \tag{B.57}$$

As regards the B-mesons systems we have in the three scenarios

$$\left|\left[(\lambda\lambda^\dagger)_{bd}\right]^2 - (\lambda\lambda^\intercal)_{bb}(\lambda^*\lambda^\dagger)_{dd}\right| \approx \begin{cases} \text{I:} \quad D_3^2 D_1^2 \\ \text{II:} \quad \epsilon^2 |(\hat\lambda_{b3}\hat\lambda_{d2}^* - \hat\lambda_{b2}\hat\lambda_{d3}^*)^2|\lambda_0^4 < 2.4\times 10^{-5}\left(\frac{M_\varphi}{10^2\,\mathrm{GeV}}\right)^2 \\ \text{III:} \quad \epsilon^4 \lambda_0^4 \end{cases} \tag{B.58}$$

and

$$\left|\left[(\lambda\lambda^\dagger)_{bs}\right]^2 - (\lambda\lambda^\intercal)_{bb}(\lambda^*\lambda^\dagger)_{ss}\right| \approx \begin{cases} \text{I:} \quad D_3^2 D_2^2 \\ \text{II:} \quad \epsilon^2 |(\hat\lambda_{b2}\hat\lambda_{s3}^* - \hat\lambda_{b3}\hat\lambda_{s2}^*)^2|\lambda_0^4 < 3.7\times 10^{-4}\left(\frac{M_\varphi}{10^2\,\mathrm{GeV}}\right)^2 . \\ \text{III:} \quad \epsilon^2 \lambda_0^4 \end{cases} \tag{B.59}$$

From these limits we can extract estimates on the hierarchy parameter ϵ when $\lambda_0 \sim \mathcal{O}(1)$. For $\lambda_0 \lesssim 0.02$ the hierarchy becomes unnecessary.

In this setting with $M_{\tilde\chi}^2 \approx M_\varphi^2$, the first scenario, which is the one with larger diagonal couplings, gives an unsuppressed contribution to the neutral mesons mixing. Assembling together the constraints from the three neutral mesons systems one obtains

$$|D_1 D_2 D_3| < (0.4\text{ - }2)\times 10^{-2}\left(\frac{M_\varphi}{\mathrm{TeV}}\right)^{3/2} \tag{B.60}$$

which for values of D_i of the same order would imply

$$D_{1,2,3} \lesssim (0.16\text{ - }0.3)\left(\frac{M_\varphi}{\mathrm{TeV}}\right)^{1/2} . \tag{B.61}$$

In order to achieve a coupling of order $\mathcal{O}(1)$, the λ matrix should exhibit some hierarchy between the diagonal couplings.

3. We can envisage scenarios in which the mass splitting between DM particles is not negligible. In these scenarios some suppression in the flavor changing phenomena can emerge also in situations in which the DM interacts with similar couplings to all SM families. For instance, we can consider one species with mass similar to the mediator mass

[27] Note that in the first scenario in case of hierarchical values for the D_i we would have the approximate bound $\epsilon^{3/2} D_2 D_3^2 < (0.2\text{ - }0.9)\times 10^{-2}(M_\varphi/1\,\mathrm{TeV})^{3/2}$.

and two lighter species for which $x \to 0$. We can take for example $x_3 \to 1$ and $x_{1,2} \to 0$:

$$M^K_{12,\mathrm{NP}} \approx \frac{1}{3} m_K f_K^2 \frac{1}{128\pi^2 M_\varphi^2} \times \left[\left[\left(\lambda\lambda^\dagger\right)_{sd}\right]^2 + \frac{1}{2}\left(\tilde{\lambda}^*_{d3}\tilde{\lambda}_{s3}\right)^2 - \frac{3}{2}\left(\tilde{\lambda}^*_{d3}\tilde{\lambda}_{s3}\right)\left(\lambda\lambda^\dagger\right)_{sd}\right]$$
$$= \frac{1}{3} m_K f_K^2 \frac{1}{128\pi^2 M_\varphi^2} \times \left[\left[\left(\lambda\lambda^\dagger\right)_{sd}\right]^2 + \frac{1}{2}\left(\lambda_{sj} W_{3j} \lambda^*_{di} W_{3i}\right)^2 - \frac{3}{2}\left(\lambda_{sj} W_{3j} \lambda^*_{di} W_{3i}\right)\left(\lambda\lambda^\dagger\right)_{sd}\right]. \quad \text{(B.62)}$$

Here the two contributions $2G(x_3 = 1, x_3 = 1)$ and $F(x_3 = 1, x_3 = 1)$ cancel each other. Notice that in these types of scenarios the mass basis rotations (and the mixing from the right) appear. In this situation there is a suppression also for the first two scenarios (I and II) with textures in Eqs. (B.12), (B.20), with $M_{12,\mathrm{NP}} \propto \epsilon^2\lambda_0^4$ for all the three neutral mesons systems (while the third scenario show a suppression similar to the other mass ranges).

We could also have considered one lighter species, e.g. $x_1 \to 0$, and two species for which $x_{2,3} \to 1$. In this case the scenario I would give an unsuppressed contribution only in one of the three systems (B_s).

The new effects are reduced also in scenarios with DM species heavier than the scalar field. For instance in a scenario with two heavy species, e.g. $x_{2,3} \to \infty$ and one light species $x_1 \to 0$ the new contribution would read

$$M^K_{12,\mathrm{NP}} \approx \frac{1}{3} m_K f_K^2 \frac{1}{128\pi^2 M_\varphi^2} (\tilde{\lambda}^*_{d1}\tilde{\lambda}_{s1})^2$$
$$= \frac{1}{3} m_K f_K^2 \hat{B}_K \frac{1}{128\pi^2 M_\varphi^2} (\lambda^*_{di} W_{1i} \lambda_{sj} W_{1j})^2 . \quad \text{(B.63)}$$

(In a scenario with two heavy species, e.g., $x_{2,3} \to \infty$ and one lighter species $x_1 \to 1$, the contribution from the two box diagrams would even cancel each other.) Similarly, in scenarios with one heavier DM particle some contributions can be reduced depending on the couplings and masses of the lighter species. For instance, taking $x_3 \to \infty$ only the couplings $\lambda_{d1,2}$, $\tilde{\lambda}_{s12}$ are involved and some ϵ suppression emerge unless $x_{1,2} \to 1$ for which the first scenario does not show suppression.

Summarizing, the flavor constraints are more safely avoided when the DM species couple more strongly to one generation of the standard fermions (as one would expect). While the power of the suppression in the different processes depends on which generation is the most strongly coupled, the hierarchy of the couplings always leads to a suppression which is independent of the mass splittings in this kind of scenario. In cases where the DM fields couple with all the SM families there can be some unsuppressed contributions in flavor changing processes. Some different attenuation of these effects in the various scenarios can be gained depending on the mass splittings between the DM particles and the scalar field and among the DM particles themselves.

References

1. C. Arina et al., t-channel dark matter models—a whitepaper. Eur. Phys. J. C **85**(9), 975 (2025). https://doi.org/10.1140/epjc/s10052-025-14635-7. arXiv:2504.10597
2. Y. Bai, J. Berger, Fermion portal dark matter. JHEP **11**, 171 (2013). https://doi.org/10.1007/JHEP11(2013)171. arXiv:1308.0612
3. A. DiFranzo, K.I. Nagao, A. Rajaraman, T.M.P. Tait, Simplified models for dark matter interacting with quarks. JHEP **11**, 014 (2013). https://doi.org/10.1007/JHEP11(2013)014. arXiv:1308.2679. [Erratum: JHEP **01**, 162 (2014)]
4. S. Biondini, L. Tiberi,, O. Panella, Connecting t-channel dark matter models to the Standard Model Effective Field Theory. JHEP **10**, 060 (2025). https://doi.org/10.1007/JHEP10(2025)060. arXiv:2507.00925
5. J. Kile, A. Soni, Flavored dark matter in direct detection experiments and at LHC. Phys. Rev. D **84**, 035016 (2011). https://doi.org/10.1103/PhysRevD.84.035016. arXiv:1104.5239
6. B. Batell, J. Pradler, M. Spannowsky, Dark matter from minimal flavor violation. JHEP **08**, 038 (2011). https://doi.org/10.1007/JHEP08(2011)038. arXiv:1105.1781
7. P. Agrawal, S. Blanchet, Z. Chacko, C. Kilic, Flavored dark matter, and its implications for direct detection and colliders. Phys. Rev. D **86**, 055002 (2012). https://doi.org/10.1103/PhysRevD.86.055002. arXiv:1109.3516
8. P. Agrawal, Z. Chacko, E.C.F.S. Fortes, C. Kilic, Skew-flavored dark matter. Phys. Rev. D **93**(10), 103510 (2016). https://doi.org/10.1103/PhysRevD.93.103510. arXiv:1511.06293
9. P. Agrawal, M. Blanke, K. Gemmler, Flavored dark matter beyond minimal flavor violation. JHEP **10**, 072 (2014). https://doi.org/10.1007/JHEP10(2014)072. arXiv:1405.6709
10. M. Blanke, S. Kast, Top-flavoured dark matter in dark minimal flavour violation. JHEP **05**, 162 (2017). https://doi.org/10.1007/JHEP05(2017)162. arXiv:1702.08457
11. M. Blanke, P. Pani, G. Polesello, G. Rovelli, Single-top final states as a probe of top-flavoured dark matter models at the LHC. JHEP **01**, 194 (2021). https://doi.org/10.1007/JHEP01(2021)194. arXiv:2010.10530
12. M. Garny, J. Heisig, B. Lülf, S. Vogl, Coannihilation without chemical equilibrium. Phys. Rev. D **96**(10), 103521 (2017). https://doi.org/10.1103/PhysRevD.96.103521. arXiv:1705.09292
13. R.T. D'Agnolo, D. Pappadopulo, J.T. Ruderman, Fourth exception in the calculation of relic abundances. Phys. Rev. Lett. **119**(6), 061102 (2017). https://doi.org/10.1103/PhysRevLett.119.061102. arXiv:1705.08450
14. H. Acaroğlu, M. Blanke, J. Heisig, M. Krämer, L. Rathmann, Flavoured majorana dark matter then and now: from freeze-out scenarios to LHC signatures. JHEP **06**, 179 (2024). https://doi.org/10.1007/JHEP06(2024)179. arXiv:2312.09274
15. J. Heisig, Conversion-driven leptogenesis: a testable theory of dark matter and baryogenesis at the electroweak scale. Phys. Rev. Lett. **133**(19), 191803 (2024). https://doi.org/10.1103/PhysRevLett.133.191803. arXiv:2404.12428

16. A. Alloul, N.D. Christensen, C. Degrande, C. Duhr, B. Fuks, FeynRules 2.0—a complete toolbox for tree-level phenomenology. Comput. Phys. Commun. **185**, 2250–2300 (2014). https://doi.org/10.1016/j.cpc.2014.04.012. arXiv:1310.1921
17. G. Belanger, F. Boudjema, P. Brun, A. Pukhov, Indirect search for dark matter with micrOMEGAs2.4. Comput. Phys. Commun. **182**, 842–856 (2011). https://doi.org/10.1016/j.cpc.2010.11.033. arXiv:1004.1092
18. G. Belanger, A. Mjallal, A. Pukhov, Recasting direct detection limits within micrOMEGAs and implication for non-standard Dark Matter scenarios. Eur. Phys. J. C **81**(3), 239 (2021). https://doi.org/10.1140/epjc/s10052-021-09012-z. arXiv:2003.08621
19. G. Alguero, G. Belanger, F. Boudjema, S. Chakraborti et al., micrOMEGAs 6.0: N-component dark matter. Comput. Phys. Commun. **299**, 109133 (2024). https://doi.org/10.1016/j.cpc.2024.109133. arXiv:2312.14894
20. D. Barducci, G. Belanger, J. Bernon, F. Boudjema, J. Da Silva et al., Collider limits on new physics within micrOMEGAs_4.3. Comput. Phys. Commun. **222**, 327–338 (2018). https://doi.org/10.1016/j.cpc.2017.08.028. arXiv:1606.03834
21. G. Alguero, J. Heisig, C.K. Khosa, S. Kraml, S. Kulkarni et al., Constraining new physics with SModelS version 2. JHEP **08**, 068 (2022). https://doi.org/10.1007/JHEP08(2022)068. arXiv:2112.00769
22. M.M. Altakach, S. Kraml, A. Lessa, S. Narasimha, SModelS v2.3: enabling global likelihood analyses. Sci Post Phys. **15**(5), 185 (2023). https://doi.org/10.21468/SciPostPhys.15.5.185. arXiv:2306.17676
23. M.M. Altakach, S. Kraml, A. Lessa, S. Narasimha, T. Pascal et al., SModelS v3: going beyond $\mathcal{Z}_2$ topologies. JHEP **11**, 074 (2024). https://doi.org/10.1007/JHEP11(2024)074. arXiv:2409.12942
24. J. Fuentes-Martín, M. König, J. Pagès, A.E. Thomsen, F. Wilsch, A proof of concept for matchete: an automated tool for matching effective theories. Eur. Phys. J. C **83**(7), 662 (2023). https://doi.org/10.1140/epjc/s10052-023-11726-1. arXiv:2212.04510
25. J. Aebischer, J. Kumar, P. Stangl, D.M. Straub, A global likelihood for precision constraints and flavour anomalies. Eur. Phys. J. C **79**(6), 509 (2019). https://doi.org/10.1140/epjc/s10052-019-6977-z. arXiv:1810.07698
26. D.M. Straub, Flavio: a Python package for flavour and precision phenomenology in the Standard Model and beyond. arXiv:1810.08132
27. J. Aebischer, J. Kumar, D.M. Straub, Wilson: a Python package for the running and matching of Wilson coefficients above and below the electroweak scale. Eur. Phys. J. C **78**(12), 1026 (2018). https://doi.org/10.1140/epjc/s10052-018-6492-7. arXiv:1804.05033
28. H. Acaroğlu, P. Agrawal, M. Blanke et al., Flavoured $(g-2)_\mu$ with dark lepton seasoning. Sci Post Phys. **15**(4), 176 (2023). https://doi.org/10.21468/SciPostPhys.15.4.176. arXiv:2212.08142
29. B. Batell, T. Lin, L.-T. Wang, Flavored dark matter and R-parity violation. JHEP **01**, 075 (2014). https://doi.org/10.1007/JHEP01(2014)075. arXiv:1309.4462
30. M. Blanke, S. Das, S. Kast, Flavoured dark matter moving left. JHEP **02**, 105 (2018). https://doi.org/10.1007/JHEP02(2018)105. arXiv:1711.10493
31. L. Lopez-Honorez, L. Merlo, Dark matter within the minimal flavour violation ansatz. Phys. Lett. B **722**, 135–143 (2013). https://doi.org/10.1016/j.physletb.2013.04.015. arXiv:1303.1087
32. F. Mescia, S. Okawa, K. Wu, Multi-component dark matter from minimal flavor violation. JHEP **11**, 114 (2024). https://doi.org/10.1007/JHEP11(2024)114. arXiv:2408.16812
33. C. Kilic, M.D. Klimek, J.-H. Yu, Signatures of top flavored dark matter. Phys. Rev. D **91**(5), 054036 (2015). https://doi.org/10.1103/PhysRevD.91.054036. arXiv:1501.02202
34. A. Kumar, S. Tulin, Top-flavored dark matter and the forward-backward asymmetry. Phys. Rev. D **87**(9), 095006 (2013). https://doi.org/10.1103/PhysRevD.87.095006. arXiv:1303.0332
35. T. Jubb, M. Kirk, A. Lenz, Charming dark matter. JHEP **12**, 010 (2017). https://doi.org/10.1007/JHEP12(2017)010. arXiv:1709.01930
36. H. Acaroğlu, M. Blanke, Tasting flavoured Majorana dark matter. JHEP **05**, 086 (2022). https://doi.org/10.1007/JHEP05(2022)086. arXiv:2109.10357
37. P. Agrawal, B. Batell, D. Hooper, T. Lin, Flavored dark matter and the galactic center gamma-ray excess. Phys. Rev. D **90**(6), 063512 (2014). https://doi.org/10.1103/PhysRevD.90.063512. arXiv:1404.1373
38. W. Bensalem, D. Stolarski, Flavor and CP violation from a QCD-like hidden sector. JHEP **02**, 011 (2022). https://doi.org/10.1007/JHEP02(2022)011. arXiv:2111.05515
39. E. Ma, Verifiable radiative seesaw mechanism of neutrino mass and dark matter. Phys. Rev. D **73**, 077301 (2006). https://doi.org/10.1103/PhysRevD.73.077301. arXiv:hep-ph/0601225
40. K.M. Zurek, Multi-component dark matter. Phys. Rev. D **79**, 115002 (2009). https://doi.org/10.1103/PhysRevD.79.115002. arXiv:0811.4429
41. C.-J. Lee, J. Tandean, Lepton-flavored scalar dark matter with minimal flavor violation. JHEP **04**, 174 (2015). https://doi.org/10.1007/JHEP04(2015)174. arXiv:1410.6803
42. P. Agrawal, Z. Chacko, C. Kilic, C.B. Verhaaren, A couplet from flavored dark matter. JHEP **08**, 072 (2015). https://doi.org/10.1007/JHEP08(2015)072. arXiv:1503.03057
43. A. Hamze, C. Kilic, J. Koeller, C. Trendafilova, J.-H. Yu, Lepton-flavored asymmetric dark matter and interference in direct detection. Phys. Rev. D **91**(3), 035009 (2015). https://doi.org/10.1103/PhysRevD.91.035009. arXiv:1410.3030
44. M.-C. Chen, J. Huang, V. Takhistov, Beyond minimal lepton flavored dark matter. JHEP **02**, 060 (2016). https://doi.org/10.1007/JHEP02(2016)060. arXiv:1510.04694
45. N. Desai, C. Kilic, Y.-P. Yang, T. Youn, Suppressed flavor violation in lepton flavored dark matter from an extra dimension. Phys. Rev. D **101**, 075043 (2020). https://doi.org/10.1103/PhysRevD.101.075043. arXiv:2001.00720
46. J. Herms, A. Ibarra, Production and signatures of multi-flavour dark matter scenarios with t-channel mediators. JCAP **10**, 026 (2021). https://doi.org/10.1088/1475-7516/2021/10/026. arXiv:2103.10392
47. H. Acaroğlu, P. Agrawal, M. Blanke, Lepton-flavoured scalar dark matter in dark minimal flavour violation. JHEP **05**, 106 (2023). https://doi.org/10.1007/JHEP05(2023)106. arXiv:2211.03809
48. H. Acaroğlu, M. Blanke, M. Tabet, Opening the Higgs portal to lepton-flavoured dark matter. JHEP **11**, 079 (2023). https://doi.org/10.1007/JHEP11(2023)079. arXiv:2309.10700
49. A.J. Buras, P. Gambino, M. Gorbahn, S. Jager, L. Silvestrini, Universal unitarity triangle and physics beyond the standard model. Phys. Lett. B **500**, 161–167 (2001). https://doi.org/10.1016/S0370-2693(01)00061-2. arXiv:hep-ph/0007085
50. G. D'Ambrosio, G.F. Giudice, G. Isidori, A. Strumia, Minimal flavor violation: an effective field theory approach. Nucl. Phys. B **645**, 155–187 (2002). https://doi.org/10.1016/S0550-3213(02)00836-2. arXiv:hep-ph/0207036
51. R.S. Chivukula, H. Georgi, Composite technicolor standard model. Phys. Lett. B **188**, 99–104 (1987). https://doi.org/10.1016/0370-2693(87)90713-1
52. L.J. Hall, L. Randall, Weak scale effective supersymmetry. Phys. Rev. Lett. **65**, 2939–2942 (1990). https://doi.org/10.1103/PhysRevLett.65.2939
53. A. Belyaev, N.D. Christensen, A. Pukhov, Calchep 3.4 for collider physics within and beyond the standard model. Comput. Phys.

Commun. **184**, 1729–1769 (2013). https://doi.org/10.1016/j.cpc.2013.01.014
54. L. Darmé, C. Degrande, C. Duhr, B. Fuks, M. Goodsell, Ufo 2.0: the 'universal Feynman output' format. Eur. Phys. J. C **83** (2023). https://doi.org/10.1140/epjc/s10052-023-11780-9
55. Planck Collaboration, N. Aghanim et al., Planck 2018 results. VI. Cosmological parameters. Astron. Astrophys. **641**, A6 (2020). https://doi.org/10.1051/0004-6361/201833910. arXiv:1807.06209. [Erratum: Astron. Astrophys. **652**, C4 (2021)]
56. J. Kawamura, S. Okawa, Y. Omura, Current status and muon $g-2$ explanation of lepton portal dark matter. JHEP **08**, 042 (2020). https://doi.org/10.1007/JHEP08(2020)042. arXiv:2002.12534
57. A. Abdelhameed, G. Angloher, P. Bauer, A. Bento, E. Bertoldo, First results from the cresst-iii low-mass dark matter program. Phys. Rev. D (2019). https://doi.org/10.1103/PhysRevD.100.102002
58. J. Aalbers, D. Akerib, C. Akerlof, A. Al Musalhi, F. Alder, et al., First dark matter search results from the lux-zeplin (lz) experiment. Phys. Rev. Lett. (2023). https://doi.org/10.1103/PhysRevLett.131.041002
59. E. Aprile, J. Aalbers, F. Agostini, M. Alfonsi, L. Althueser, Dark matter search results from a one ton-year exposure of xenon1t. Phys. Rev. Lett. (2018). https://doi.org/10.1103/PhysRevLett.121.111302
60. E. Aprile, J. Aalbers, F. Agostini, M. Alfonsi, L. Althueser, Constraining the spin-dependent wimp-nucleon cross sections with xenon1t. Phys. Rev. Lett. (2019). https://doi.org/10.1103/PhysRevLett.122.141301
61. P. Agnes, I. Albuquerque, T. Alexander, A. Alton, G. Araujo, Low-mass dark matter search with the darkside-50 experiment. Phys. Rev. Lett. (2018). https://doi.org/10.1103/PhysRevLett.121.081307
62. C. Amole, M. Ardid, I. Arnquist, D. Asner, D. Baxter et al., Dark matter search results from the complete exposure of the pico-60 c_3f_8 bubble chamber. Phys. Rev. D (2019). https://doi.org/10.1103/PhysRevD.100.022001
63. S. Archambault, A. Archer, W. Benbow, R. Bird, E. Bourbeau, Dark matter constraints from a joint analysis of dwarf spheroidal galaxy observations with veritas. Phys. Rev. D (2017). https://doi.org/10.1103/PhysRevD.95.082001
64. A. Acharyya, C.B. Adams, P. Bangale, J.T. Bartkoske, P. Batista, An indirect search for dark matter with a combined analysis of dwarf spheroidal galaxies from veritas (2024). arxiv:2407.16518
65. A. Cuoco, J. Heisig, M. Korsmeier, M. Krämer, Constraining heavy dark matter with cosmic-ray antiprotons. JCAP **04**, 004 (2018). https://doi.org/10.1088/1475-7516/2018/04/004. arXiv:1711.05274
66. I. John, T. Linden, Cosmic-ray positrons strongly constrain leptophilic dark matter. J. Cosmol. Astropart. Phys. **2021**, 007 (2021). https://doi.org/10.1088/1475-7516/2021/12/007
67. M. Cirelli, A. Strumia, J. Zupan, D. Matter, arXiv:2406.01705
68. A. Albert, B. Anderson, K. Bechtol, A. Drlica-Wagner, M. Meyer et al., Searching for dark matter annihilation in recently discovered milky way satellites with fermi-lat. Astrophys. J. **834**, 110 (2017). https://doi.org/10.3847/1538-4357/834/2/110
69. M. collaboration, Limits to dark matter annihilation cross-section from a combined analysis of magic and fermi-lat observations of dwarf satellite galaxies. J. Cosmol. Astropart. Phys. **2016**, 039 (2016). https://doi.org/10.1088/1475-7516/2016/02/039
70. F. Calore, M. Cirelli, L. Derome, Y. Genolini, AMS-02 antiprotons and dark matter: trimmed hints and robust bounds. Sci Post Phys. **12**(5), 163 (2022). https://doi.org/10.21468/SciPostPhys.12.5.163. arXiv:2202.03076
71. C. Armand, E. Charles, M. di Mauro, C. Giuri, J. P. Harding, et al., Combined dark matter searches towards dwarf spheroidal galaxies with fermi-lat, hawc, h.e.s.s., magic, and veritas (2021). arxiv:2108.13646
72. H. Abdallah, A. Abramowski, F. Aharonian, F. Ait Benkhali, A. Akhperjanian et al., Search for dark matter annihilations towards the inner galactic halo from 10 years of observations with h.e.s.s. Phys. Rev. Lett. (2016). https://doi.org/10.1103/PhysRevLett.117.111301
73. M. Ackermann, A. Albert, B. Anderson, W. Atwood, L. Baldini, Searching for dark matter annihilation from milky way dwarf spheroidal galaxies with six years of fermi large area telescope data. Phys. Rev. Lett. (2015). https://doi.org/10.1103/PhysRevLett.115.231301
74. J. Aleksić, S. Ansoldi, L. Antonelli, P. Antoranz, A. Babic et al., Optimized dark matter searches in deep observations of segue 1 with magic. J. Cosmol. Astropart. Phys. **2014**, 008–008 (2014). https://doi.org/10.1088/1475-7516/2014/02/008
75. T.I. Collaboration, R. Abbasi, M. Ackermann, J. Adams, S.K. Agarwalla, Search for neutrino lines from dark matter annihilation and decay with icecube (2023). arXiv:2303.13663
76. A. Albert, M. André, M. Anghinolfi, G. Anton, M. Ardid et al., Search for dark matter towards the galactic centre with 11 years of antares data. Phys. Lett. B **805**, 135439 (2020). https://doi.org/10.1016/j.physletb.2020.135439
77. F. Ambrogi, C. Arina, M. Backovic, J. Heisig et al., MadDM v.3.0: a comprehensive tool for dark matter studies. Phys. Dark Univ. **24**, 100249 (2019). https://doi.org/10.1016/j.dark.2018.11.009. arXiv:1804.00044
78. C. Arina, J. Heisig, F. Maltoni, D. Massaro, O. Mattelaer, Indirect dark-matter detection with MadDM v3.2—lines and loops. Eur. Phys. J. C **83**(3), 241 (2023). https://doi.org/10.1140/epjc/s10052-023-11377-2. arXiv:2107.04598
79. T. Bringmann, L. Bergstrom, J. Edsjo, New gamma-ray contributions to supersymmetric dark matter annihilation. JHEP **01**, 049 (2008). https://doi.org/10.1088/1126-6708/2008/01/049. arXiv:0710.3169
80. M. Garny, A. Ibarra, S. Vogl, Dark matter annihilations into two light fermions and one gauge boson: general analysis and antiproton constraints. JCAP **04**, 033 (2012). https://doi.org/10.1088/1475-7516/2012/04/033. arXiv:1112.5155
81. C. Arina, B. Fuks, J. Heisig, M. Krämer, L. Mantani, Comprehensive exploration of t-channel simplified models of dark matter. Phys. Rev. D **108**(11), 115007 (2023). https://doi.org/10.1103/PhysRevD.108.115007. arXiv:2307.10367
82. A. Carmona, A. Lazopoulos, P. Olgoso, J. Santiago, Matchmakereft: automated tree-level and one-loop matching, Sci Post. Phys. 12(6), 198 (2022). https://doi.org/10.21468/SciPostPhys.12.6.198. arXiv:2112.10787
83. S.D. Bakshi, J. Chakrabortty, S.K. Patra, CoDEx: Wilson coefficient calculator connecting SMEFT to UV theory. Eur. Phys. J. C **79**(1), 21 (2019). https://doi.org/10.1140/epjc/s10052-018-6444-2. arXiv:1808.04403
84. W. Buchmuller, D. Wyler, Effective Lagrangian analysis of new interactions and flavor conservation. Nucl. Phys. B **268**, 621–653 (1986). https://doi.org/10.1016/0550-3213(86)90262-2
85. B. Grzadkowski, M. Iskrzynski, M. Misiak, J. Rosiek, Dimension-six terms in the standard model Lagrangian. JHEP **10**, 085 (2010). https://doi.org/10.1007/JHEP10(2010)085. arXiv:1008.4884
86. I. Brivio, M. Trott, The standard model as an effective field theory. Phys. Rep. **793**, 1–98 (2019). https://doi.org/10.1016/j.physrep.2018.11.002. arXiv:1706.08945
87. G. Isidori, F. Wilsch, D. Wyler, The standard model effective field theory at work. Rev. Mod. Phys. **96**(1), 015006 (2024). https://doi.org/10.1103/RevModPhys.96.015006. arXiv:2303.16922
88. J. Aebischer, A.J. Buras, J. Kumar, SMEFT ATLAS: The Landscape Beyond the Standard Model. arXiv:2507.05926

89. E.E. Jenkins, A.V. Manohar, M. Trott, Renormalization group evolution of the standard model dimension six operators I: formalism and lambda dependence. JHEP **10**, 087 (2013). https://doi.org/10.1007/JHEP10(2013)087. arXiv:1308.2627
90. E.E. Jenkins, A.V. Manohar, M. Trott, Renormalization group evolution of the standard model dimension six operators II: Yukawa dependence. JHEP **01**, 035 (2014). https://doi.org/10.1007/JHEP01(2014)035. arXiv:1310.4838
91. R. Alonso, E.E. Jenkins, A.V. Manohar, M. Trott, Renormalization group evolution of the standard model dimension six operators III: gauge coupling dependence and phenomenology. JHEP **04**, 159 (2014). https://doi.org/10.1007/JHEP04(2014)159. arXiv:1312.2014
92. E.E. Jenkins, A.V. Manohar, P. Stoffer, Low-energy effective field theory below the electroweak scale: operators and matching. JHEP **03**, 016 (2018). https://doi.org/10.1007/JHEP03(2018)016. arXiv:1709.04486. [Erratum: JHEP **12**, 043 (2023)]
93. W. Dekens, P. Stoffer, Low-energy effective field theory below the electroweak scale: matching at one loop. JHEP **10**, 197 (2019). https://doi.org/10.1007/JHEP10(2019)197. arXiv:1908.05295. [Erratum: JHEP **11**, 148 (2022)]
94. E.E. Jenkins, A.V. Manohar, P. Stoffer, Low-energy effective field theory below the electroweak scale: anomalous dimensions. JHEP **01**, 084 (2018). https://doi.org/10.1007/JHEP01(2018)084. arXiv:1711.05270. [Erratum: JHEP **12**, 042 (2023)]
95. A. Celis, J. Fuentes-Martin, A. Vicente, J. Virto, DsixTools: the standard model effective field theory toolkit. Eur. Phys. J. C **77**(6), 405 (2017). https://doi.org/10.1140/epjc/s10052-017-4967-6. arXiv:1704.04504
96. J. Aebischer, WCxf: an exchange format for Wilson coefficients beyond the Standard Model. Comput. Phys. Commun. **232**, 71–83 (2018). https://doi.org/10.1016/j.cpc.2018.05.022. arXiv:1712.05298
97. L. Buonocore, P. Nason, F. Tramontano, G. Zanderighi, Leptons in the proton. J. High Energy Phys. (2020). https://doi.org/10.1007/JHEP08(2020)019
98. A.M. Sirunyan, A. Tumasyan, W. Adam, T. Bergauer, M. Dragicevic et al., Search for supersymmetry in final states with two oppositely charged same-flavor leptons and missing transverse momentum in proton-proton collisions at $\sqrt{s}$ = 13 tev. J. High Energy Phys. (2021). https://doi.org/10.1007/JHEP04(2021)123
99. ATLAS Collaboration, G. Aad et al., Search for direct production of charginos, neutralinos and sleptons in final states with two leptons and missing transverse momentum in pp collisions at $\sqrt{s} = 8$ TeV with the ATLAS detector. JHEP**05**, 071 (2014). https://doi.org/10.1007/JHEP05(2014)071. arXiv:1403.5294
100. CMS Collaboration, A. M. Sirunyan et al., Search for supersymmetric partners of electrons and muons in proton-proton collisions at $\sqrt{s} = 13$ TeV, *Phys. Lett. B***790** (2019) 140-166, arXiv:1806.05264. https://doi.org/10.1016/j.physletb.2019.01.005
101. J. Abdallah et al., Searches for supersymmetric particles in e + e- collisions up to 208 gev and interpretation of the results within the mssm. Eur. Phys. J. C **31**, 421–479 (2003). https://doi.org/10.1140/epjc/s2003-01355-5
102. A. Ibarra, M. Reichard, R. Nagai, Anapole moment of Majorana fermions and implications for direct detection of neutralino dark matter. JHEP **01**, 086 (2023). https://doi.org/10.1007/JHEP01(2023)086. arXiv:2207.01014
103. C. Patrignani, Review of particle physics. Chin. Phys. C **40**(10), 100001 (2016). https://doi.org/10.1088/1674-1137/40/10/100001
104. K. Hayasaka et al., Search for lepton flavor violating tau decays into three leptons with 719 million produced Tau+Tau- pairs. Phys. Lett. B **687**, 139–143 (2010). https://doi.org/10.1016/j.physletb.2010.03.037. arXiv:1001.3221
105. ATLAS Collaboration, G. Aad et al., Search for squarks and gluinos in final states with jets and missing transverse momentum using 139 fb^{-1} of $\sqrt{s}$ =13 TeV pp collision data with the ATLAS detector. JHEP **02**, 143 (2021). https://doi.org/10.1007/JHEP02(2021)143. arXiv:2010.14293
106. C.M.S. Collaboration, T.C. Collaboration et al., Search for supersymmetry in proton-proton collisions at 13 TeV in final states with jets and missing transverse momentum. JHEP **10**, 244 (2019). https://doi.org/10.1007/JHEP10(2019)244. arXiv:1908.04722
107. CMS Collaboration, A.M. Sirunyan et al., Search for supersymmetry in multijet events with missing transverse momentum in proton-proton collisions at 13 TeV. Phys. Rev. D **96**(3), 032003 (2017). https://doi.org/10.1103/PhysRevD.96.032003. arXiv:1704.07781
108. CMS Collaboration, A.M. Sirunyan et al., Search for new phenomena with the M_{T2} variable in the all-hadronic final state produced in proton-proton collisions at $\sqrt{s} = 13$ TeV. Eur. Phys. J. C **77**(10), 710 (2017). https://doi.org/10.1140/epjc/s10052-017-5267-x. arXiv:1705.04650
109. CMS Collaboration, A.M. Sirunyan et al., Search for top squark production in fully-hadronic final states in proton-proton collisions at $\sqrt{s} = 13$ TeV. Phys. Rev. D **104**(5), 052001 (2021). https://doi.org/10.1103/PhysRevD.104.052001. arXiv:2103.01290
110. CMS Collaboration, A.M. Sirunyan et al., Search for the pair production of third-generation squarks with two-body decays to a bottom or charm quark and a neutralino in proton-proton collisions at $\sqrt{s} = 13$ TeV. Phys. Lett. B **778**, 263–291 (2018). https://doi.org/10.1016/j.physletb.2018.01.012. arXiv:1707.07274
111. ATLAS Collaboration, G. Aad et al., Search for direct third-generation squark pair production in final states with missing transverse momentum and two b-jets in $\sqrt{s} = 8$ TeV pp collisions with the ATLAS detector. JHEP **10**, 189 (2013). https://doi.org/10.1007/JHEP10(2013)189. arXiv:1308.2631
112. ATLAS Collaboration, M. Aaboud et al., Search for supersymmetry in events with b-tagged jets and missing transverse momentum in pp collisions at $\sqrt{s} = 13$ TeV with the ATLAS detector. JHEP **11**, 195 (2017). https://doi.org/10.1007/JHEP11(2017)195. arXiv:1708.09266
113. ATLAS Collaboration, M. Aaboud et al., Search for squarks and gluinos in final states with jets and missing transverse momentum using 36 fb^{-1} of $\sqrt{s} = 13$ TeV pp collision data with the ATLAS detector. Phys. Rev. D **97**(11), 112001 (2018). https://doi.org/10.1103/PhysRevD.97.112001. arXiv:1712.02332
114. ATLAS Collaboration, G. Aad et al., Search for squarks and gluinos with the ATLAS detector in final states with jets and missing transverse momentum using $\sqrt{s} = 8$ TeV proton-proton collision data. JHEP **09**, 176 (2014). https://doi.org/10.1007/JHEP09(2014)176. arXiv:1405.7875
115. V. Khachatryan, A.M. Sirunyan, A. Tumasyan, W. Adam, T. Bergauer, Searches for supersymmetry using the m t2 variable in hadronic events produced in pp collisions at 8 tev. J. High Energy Phys. (2015). https://doi.org/10.1007/JHEP05(2015)078
116. ATLAS Collaboration, G. Aad et al., Search for pair-produced third-generation squarks decaying via charm quarks or in compressed supersymmetric scenarios in pp collisions at $\sqrt{s} = 8$ TeV with the ATLAS detector. Phys. Rev. D **90**(5), 052008 (2014). https://doi.org/10.1103/PhysRevD.90.052008. arXiv:1407.0608
117. CMS Collaboration, Search for heavy stable charged particles with 12.9 fb^{-1} of 2016 data
118. ATLAS Collaboration, M. Aaboud et al., Search for heavy charged long-lived particles in the ATLAS detector in 36.1 fb^{-1} of proton-proton collision data at $\sqrt{s} = 13$ TeV. Phys. Rev. D **99**(9), 092007 (2019). https://doi.org/10.1103/PhysRevD.99.092007. arXiv:1902.01636

119. CMS Collaboration, Search for direct production of bottom squark pairs. https://cds.cern.ch/record/1693164
120. M. Drees, M. Nojiri, Neutralino—nucleon scattering revisited. Phys. Rev. D **48**, 3483–3501 (1993). https://doi.org/10.1103/PhysRevD.48.3483. arXiv:hep-ph/9307208
121. P. Gondolo, S. Scopel, On the sbottom resonance in dark matter scattering. JCAP **10**, 032 (2013). https://doi.org/10.1088/1475-7516/2013/10/032. arXiv:1307.4481
122. G. Jungman, M. Kamionkowski, K. Griest, Supersymmetric dark matter. Phys. Rep. **267**, 195–373 (1996). https://doi.org/10.1016/0370-1573(95)00058-5. arXiv:hep-ph/9506380
123. Particle Data Group Collaboration, M. Tanabashi et al., Review of particle physics. Phys. Rev. D **98**(3), 030001 (2018). https://doi.org/10.1103/PhysRevD.98.030001
124. HFLAV Collaboration, Y.S. Amhis et al., Averages of b-hadron, c-hadron, and τ-lepton properties as of 2021 Phys. Rev. D **107**(5), 052008 (2023). https://doi.org/10.1103/PhysRevD.107.052008. arXiv:2206.07501
125. HFLAV Collaboration, Y. Amhis et al., Averages of b-hadron, c-hadron, and τ-lepton properties as of summer 2014. arXiv:1412.7515
126. S. Descotes-Genon, A. Falkowski, M. Fedele, M. González-Alonso, J. Virto, The CKM parameters in the SMEFT. JHEP **05**, 172 (2019). https://doi.org/10.1007/JHEP05(2019)172. arXiv:1812.08163
127. H. Führ, Z. Rzeszotnik, A note on factoring unitary matrices. Linear Algebra Appl. **547**, 32–44 (2018). https://doi.org/10.1016/j.laa.2018.02.017
128. Flavour Lattice Averaging Group (FLAG) Collaboration, Y. Aoki et al., FLAG Review 2021. Eur. Phys. J. C **82**(10), 869 (2022). https://doi.org/10.1140/epjc/s10052-022-10536-1. arXiv:2111.09849
129. Y. Aoki, FLAG Review (2024). arXiv:2411.04268
130. T. Inami, C.S. Lim, Effects of superheavy quarks and leptons in low-energy weak processes k(L) −> mu anti-mu, K+ −> pi+ neutrino anti-neutrino and K0 < − > anti-K0. Prog. Theor. Phys. **65**, 297 (1981). https://doi.org/10.1143/PTP.65.297. [Erratum: Prog. Theor. Phys. **65**, 1772 (1981)]
131. G. Buchalla, A.J. Buras, M.E. Lautenbacher, Weak decays beyond leading logarithms. Rev. Mod. Phys. **68**, 1125–1144 (1996). https://doi.org/10.1103/RevModPhys.68.1125. arXiv:hep-ph/9512380
132. Z. Bai, N.H. Christ, T. Izubuchi, C.T. Sachrajda, A. Soni et al., $K_L - K_S$ mass difference from lattice QCD. Phys. Rev. Lett. **113**, 112003 (2014). https://doi.org/10.1103/PhysRevLett.113.112003. arXiv:1406.0916
133. Z. Bai, N.H. Christ, C.T. Sachrajda, The K_L - K_S mass difference. EPJ Web Conf. **175**, 13017 (2018). https://doi.org/10.1051/epjconf/201817513017
134. Particle Data Group Collaboration, S. Navas et al., Review of particle physics. Phys. Rev. D **110**(3), 030001 (2024). https://doi.org/10.1103/PhysRevD.110.030001
135. M. Bona et al., Unitarity Triangle global fits beyond the Standard Model: UTfit 2021 NP update. PoS **EPS-HEP2021**, 500 (2022). https://doi.org/10.22323/1.398.0500